DESIGN AND MODELING OF WIRELESS LINKS FOR BIOMEDICAL IMPLANTABLE APPLICATIONS

DUAN ZHU

(B.S. Huazhong Uni. of Sci. & Tech., 2009)

A THESIS SUBMITTED

FOR THE DEGREE OF DOCTOR OF PHILOSOPHY

DEPARTMENT OF ELECTRICAL AND COMPUTER ENGINEERING

NATIONAL UNIVERSITY OF SINGAPORE

2013

Declaration

I hereby declare that this thesis is my original work and it has been written by me in its entirety.

I have duly acknowledged all the sources of information which have been used in the thesis.

This thesis has also not been submitted for any degree in any university previously.

Duan Zhu

Duan Zhu

25 July 2013

Abstract

Implantable microsystems have attracted attention from researchers all around the world, due to the fact that the miniaturization of electronics systems and reduction of power consumption of chips make the actual implantation of extremely complex microsystems possible.

For these microsystems, the wireless communication link is essential to ensure robust communications between an implanted device and an external monitoring apparatus. For most cases, the communication link is composed of power link and data link. The power link consists of two closely spaced coils intended for wireless power transfer based on inductive coupling. The data link is realized by either coupling coils for near-field communications or a pair of antennas for far-field purposes. This work presents the optimization method of rectangular coils for maximum power transfer efficiency; proposes the first differentially fed dual-band implantable antenna for data transfer in neural recording system and evaluates the performance of a novel differential antenna in MICS and ISM bands for dual-mode operation. Also, the interference issues between the power link and data link are examined as well.

Acknowledgements

Both the thesis and the author have benefitted a great deal from many people over the past four years. Without their consistent help and encouragement, this work cannot be achievable.

Foremost, I would like to give my special thanks to my kind supervisor, Prof. Yong-Xin Guo, for introducing me into such a wonderful and meaningful area of Microwave and Radio Frequency intended for biomedical implantable applications. His prospective insight at the scientific frontier really helped me a lot in carrying out the research work. Thank you for your help all along the way.

Secondly, I would like to give my hearty thanks to my co-supervisor Prof. Dim-Lee Kwong and my group leader Dr. Minkyu Je from Institute of Microelectronics (IME), A*STAR. Ever since I joined the group in IME, they have helped me a lot in understanding the bio-implants from system point of view. I am really grateful for their kind help offered.

Thirdly, I would like to thank all the fellow researchers for their sincere help: Dr. Hui Chu, Dr. Meysam Sabahi Al-shoara, Dr. Yujian Chen, Dr. Zhengguo Liu, Dr. Xinyi Tang, Changrong Liu, Dr. Lei Wang, Rangarajan Jegadeesan, Dr. Xiaoyue Bao, Lijie Xu, Hucheng Sun, and Yunshen Long. The useful technical discussions with them have been extremely beneficial in completing my research work.

Lastly, I would like to thank my beloved parents. Apart from my own research interests, their deep understanding and endless support for me has also been an important source of motivation for me in the pursuit of the scientific path. Thanks a lot for your caring and love.

List of Publications

[1] **Z. Duan**, Y.X. Guo, M. Je, and D.L. Kwong, "Design and in vitro test of differentially fed dual-band implantable antenna operating at MICS and ISM bands", *IEEE Trans. Antennas Propag.*, major revision.

[2] **Z. Duan**, Y.X. Guo, R.F. Xue, M. Je, and D.L. Kwong, "Differentially-fed dual-band implantable antenna for biomedical applications", *IEEE Trans. Antennas Propag.*, vol. 60, no.12, pp. 5587-5595, Dec 2012.

[3] **Z. Duan**, Y.X. Guo, and D.L. Kwong, "Rectangular coils optimization for wireless power transmission", *Radio Sci.*, vol. 47, RS3012, Jun. 2012.

[4] K. Cheng, X. Zou, J. H. Cheong, R.-F. Xue, Z. Chen, L. Yao, H.-K. Cha, S. J. Cheng, P. Li, L. Liu, L. Andia, C. K. Ho, M.-Y. Cheng, **Z. Duan**, R. Rajkumar, Y. Zheng, W. L. Goh, Y. Guo, G. Dawe, W.-T. Park, and M. Je, "100-channel wireless neural recording system with 54-Mb/s data link and 40%-efficiency power link," in *Proc. IEEE Asian Solid State Circuits Conference (A-SSCC) Dig. Tech. Papers*, Nov. 2012, pp.185–188.

[5] **Z. Duan**, Y.X. Guo, R.F. Xue, M. Je, and D.L. Kwong, "Investigation of the mutual effect between power link and data link for biomedical applications", *IEEE International Symposium on Radio-Frequency Integration Technology (RFIT)*, Singapore, Singapore, Nov. 21-23, 2012, pp. 219-221.

[6] **Z. Duan**, Y.X. Guo, "Rectangular coils modeling for inductive links in implantable biomedical devices", *IEEE International Symposium on Antennas and Propagation (APSURSI)*, Spokane, Washington, USA, Jul. 3-8, 2011, pp. 388-391.

[7] Y.X. Guo, **Z. Duan**, R. Jegadeesan, "Inductive wireless power transmission for implantable devices", *2011 International Workshop on Antenna Technology (iWAT)*, Mar. 7-9, Hong Kong, 2011, pp. 445-448.

Table of Contents

List of Tables

List of Figures

List of Symbols

ω	angular frequency
f_{BT}	back telemetry frequency
C	capacitance
σ	conductivity
k	coupling coefficient
I	current
ρ	density
d	diameter
D	distance
η	efficiency
W	energy
f_{FD}	forward data telemetry frequency
f	frequency
Z	impedance
L	inductance
l	length
$tan\delta$	loss tangent
m	mass
M	mutual inductance
n	number of turns
μ	permeability
ε_0	permittivity of free space
P	power
f_P	power frequency
Q	quality factor
r	ratio
Γ	reflection coefficient

ε_r	relative permittivity
R	resistance
δ	skin depth
s	space
h	substrate thickness
t	thickness
V	voltage
λ	wavelength
w	width

List of Acronyms

ADS	Advanced Design System
BER	Bit Error Rate
CMOS	Complementary Metal–Oxide–Semiconductor
CST	Computer Simulation Technology
EIRP	Effective Isotropically Radiated Power
ESR	Effective Series Resistance
FEM	Finite Element Method
HF	High Frequency
HFSS	High Frequency Structural Simulator
IC	Integrated Circuit
IL	Implementation Loss
ISM	Industrial, Scientific, and Medical
MICS	Medical Implant Communication Services
PCB	Printed Circuit Board
PEC	Perfect Electrical Conductor
PIFA	Planar Inverted-F Antenna
PL	Path Loss
RF	Radio Frequency
RFID	Radio-frequency Identification
RNF	Receiver Noise Floor
SAR	Specific Absorption Rate
SMA	Subminiature version A
SNR	Signal to Noise Ratio
UHF	Ultra High Frequency
VHF	Very High Frequency
WBAN	Wireless Body Area Network
WLAN	Wireless Local Area Network
WMAN	Wireless Metropolitan Area Network
WMTS	Wireless Medical Telemetry Services
WPAN	Wireless Personal Area Network
UWB	Ultra-Wideband

Chapter 1

Introduction

1.1 Background for Biomedical Telemetry Systems

Ever since the gradual implementation of cardiac pacemakers in the mid-20th century, biomedical telemetry systems have drawn attention from researchers all over the world, because they play a vital role for the communications between implanted devices and external base stations. Recent research advancement of wireless telemetry systems in biomedical areas has been numerous [1], [2]. Typical applications include cochlea implants [3], [4], retinal prosthesis [5], [6], neural recording system [7], [8], glucose and other physiological parameters monitoring [9], [10] and peripheral nerve prostheses [11].

By way of various biotelemetry links, the electromagnetic energy for powering the implanted devices and the control signals can be transferred wirelessly from outside into the human body. Also, the physiological information regarding the human health status collected by small biosensors implanted inside the human tissue can be transmitted wirelessly to an external central unit for processing, then further to experienced doctors for analysis and diagnosis. In this way, a reliable communication link has been established between the patients and doctors. For patients in hospital or even at home, their health status can be monitored in real-time. Therefore in case of emergency breakout, a timely health care preventive maintenance or medical surgery can be ensured.

For some healthcare applications, a wireless network should be developed. The Radio Frequency (RF)-based wireless networking technology that interconnects these separate body sensor units around the human body can be

referred as Wireless Body Area Network (WBAN) [12], [13]. WBAN can be further complemented by Wireless Personal Area Network (WPAN), which can enhance the communication coverage from 2 m to 10 m. These networks can finally be connected to Wireless Local Area Network (WLAN) and Wireless Metropolitan Area Network (WMAN) by way of various wired and wireless communication technologies. The schematic for the complete interconnection is shown in Figure 1-1 [12].

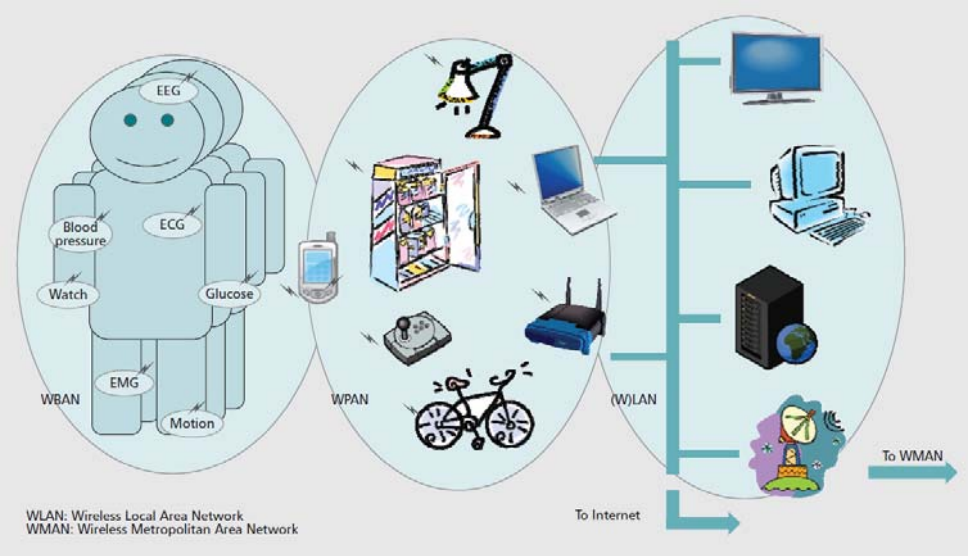

Figure 1-1 Interconnection of WBAN, WPAN, WLAN and WMAN [12].

For implantable applications, usually energy is needed to power the implanted devices. Battery may be a reasonable option as long as it can last for a long time, avoiding the necessity of frequent medical surgery for battery replacement. For the case of an implanted device with relatively high power consumption where an internal battery cannot handle, a wireless transcutaneous link should be employed. In the 1990s, a single inductive wireless link composed of two coils is used for both power and data transfer [14], [15], as shown in Figure 1-2 (a) [14].

However, for applications such as retinal prosthesis and neural recording during recent years, the data rate increases dramatically from kbps range to mbps range. This presents a great challenge for utilizing just one inductive link for both power and data transfer. On one hand, large Quality factor (Q factor) coils are necessary for better power transfer efficiency, which will be explained in Chapter 2. On the other hand, larger bandwidth is necessary for

larger data handling capacity, which means smaller Q for the coils. Due to this reason, separate links with respective power and data transmission purpose are developed, as shown in Figure 1-2 (b) [16].

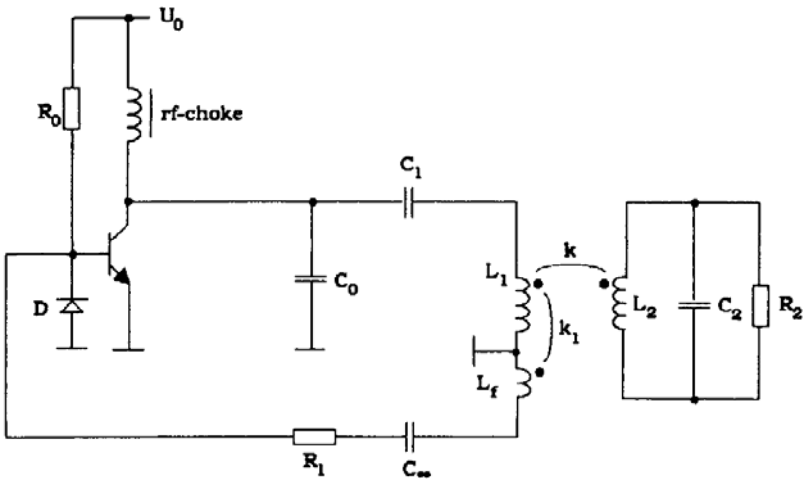

(a)

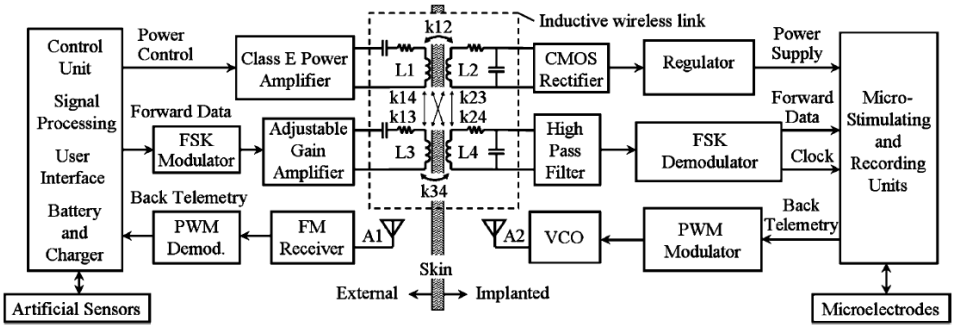

(b)

Figure 1-2 (a) Single inductive link used in the power and data transfer system [14] (b) The block diagram of a neuroprosthetic system with multiple links [16].

Normally, the power link is composed of two inductive coils, either in circular or rectangular forms [17]-[21], such as the pair of L1 and L2 shown in Figure 1-2 (b). The power carried by electromagnetic wave is transferred from outside the body into the implanted device in the human tissue. This type of power transfer is similar as that of the traditional transformers in electric power delivery systems, which is based on inductive coupling in the near field, and the magnetic flux leads to the mutual inductance between two inductors and therefore ensures the successful transfer of energy. For increasing the self and mutual inductance and therefore the Q factors, often multi-turn loop coils with small resistance values are adopted.

For most applications, there are two data links, the downlink and the uplink [22]. The downlink usually transmits control and command signals, and the data is transferred from outside to inside. Downlink can also be termed as the forward data telemetry, which is the coil pair of L3 and L4 shown in Figure 1-2 (b). The uplink transfers the physiological data collected by implanted bio-sensors and related Integrated Circuit (IC) chips to outside the human body for processing and analysis, which is the back telemetry A1 and A2 shown in Figure 1-2 (b). When the data rate requirement is not demanding, the data link can also be incorporated into the power link as shown in Figure 1-3.

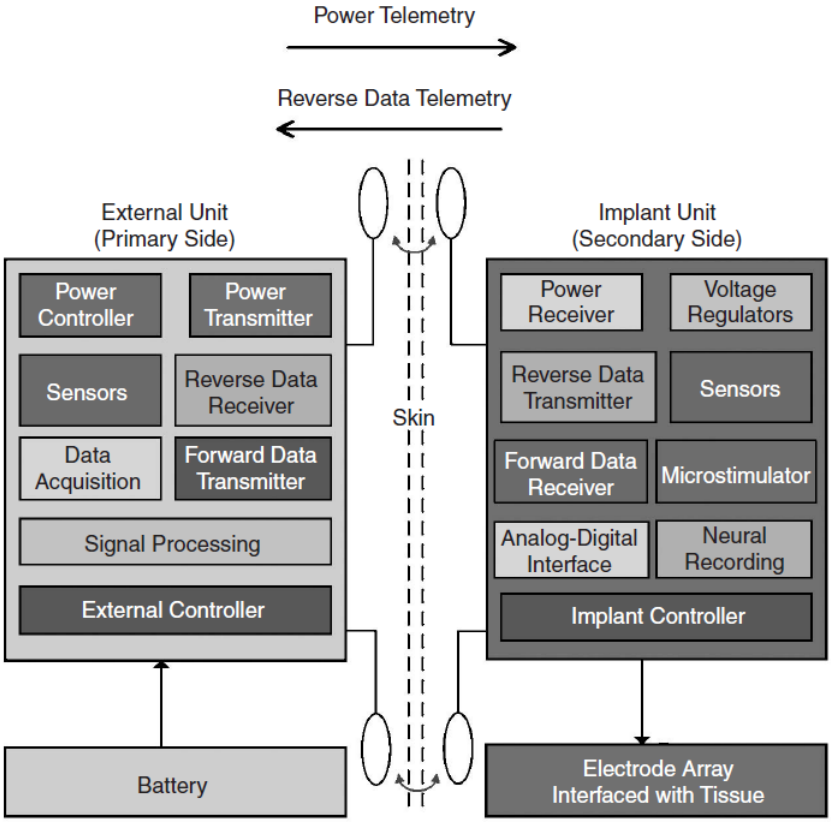

Figure 1-3 The block diagram of an implantable prosthetic system [23].

For the realization of the data link, usually either near-field inductive coils [22], [23] or far-field antennas [24] are adopted depending on specific applications. Near-field coils are coupled to each other through inductive coupling, which is quite effective when operated in the near field, and the usual operating distance is around 10 mm. However, when the distance is increased, the efficiency drops significantly. Therefore for long distance

operation, coupling antenna pairs resonating at the same frequency are adopted [24].

1.2 Frequency Bands, Tissue Properties and Safety Issues

1.2.1 Frequency Bands for Biomedical Telemetry

For the operation of wireless links, normally High Frequency (HF) at 3 MHz to 30 MHz is adopted for power transfer [17]-[21], while Very High Frequency (VHF) at 30 MHz to 300 MHz and Ultra High Frequency (UHF) at 300 MHz to 3 GHz are adopted for data transfer [16], [24], [24]. However, most of the times, the selection of frequency bands are based on specific applications rather than being in the strictly predefined range. For instance, in the case of Figure 1-2 (b) [16], three different frequency bands are selected. A low-frequency (f_P < 1 MHz) carrier is selected for power transfer from the external side to the inside. A medium-frequency (f_{FD} = 1 ~ 100 MHz) carrier is selected for the forward data telemetry. And a high-frequency (f_{BT} > 400 MHz) carrier is selected for the back telemetry.

Table 1-1 Common frequency bands for data communication for biomedical application

Frequency range	Name of band
402 ~ 405 MHz	Medical Implant Communication Services (MICS)
1395 ~ 1400 MHz	Wireless Medical Telemetry Services (WMTS)
2.4 ~ 2.5 GHz	Industrial Scientific Medical (ISM)
3.5 ~ 4.5 GHz	Ultra-wideband (UWB)

In general words, for wireless power transfer, the frequency is often located at around several megahertz or dozens of megahertz range. For data communication in the far-field, there are several frequently used bands, such as 402 MHz ~ 405 MHz Medical Implant Communication Services (MICS) band [26]-[35], 1395 ~ 1400 MHz Wireless Medical Telemetry Services (WMTS) band [36], 2.4 ~ 2.5 GHz Industrial Scientific Medical (ISM) band [37]-[39], and 3.5 ~ 4.5 GHz Ultra-wideband (UWB) [40]. We summarize the

frequency bands for data communication for biomedical applications in Table 1-1. For ISM band, there are also other band ranges as listed in Table 1-2. However, 2.45 GHz is most commonly used for data communication for biomedical implants [9], [37]-[39].

MICS band is allocated to biotelemetry applications according to Recommendation ITU-R SA.1346, and later superseded by RS. 1346 [41]. However, the band 401-406 MHz is previously allocated to the Meteorological Aids Service, in order to reduce the harmful interference that might occur to the operation of Meteorological Aids, a maximum limit of -16 dBm on the Effective Isotropically Radiated Power (EIRP) of MICS is specified.

Table 1-2 Frequency bands for ISM band

Frequency range (MHz)	**Centre frequency (MHz)**	**Frequency range (GHz)**	**Centre frequency (GHz)**
6.765 ~ 6.795	6.78	2.4 ~ 2.5	2.45
13.553 ~ 13.567	13.56	5.725 ~ 5.875	5.8
26.957 ~ 27.283	27.12	24 ~ 24.25	24.125
40.66 ~ 40.70	40.68	61 ~ 61.5	61.25
433.05 ~ 434.79	433.92	122 ~ 123	122.5
902 ~ 928	915	244 ~ 246	245

For ISM band, there are a few frequency ranges, which are summarized in Table 1-2 [42]. For some of the lower bands in ISM, it is also used for wireless power transfer, such as 6.78 MHz [21] or 13.56 MHz [18]. 13.56 MHz is also a Radio-frequency Identification (RFID) band. The higher bands at 433.92 MHz, 915 MHz, 2.45 GHz and 5.8 GHz for data communication are thoroughly compared in previous work [43]. For all ISM bands, 2.45GHz is most commonly adopted for data transmission for biomedical applications.

1.2.2 Tissue Properties and Human Models

The dielectric properties at different frequencies for different body tissues have been investigated [44]. Here in Figure 1-4 we show a graph of the relative permittivity and conductivity of the most commonly used human tissues: skin, fat and muscle. The figure is plotted with respect to a frequency span from 0.1 GHz to 10 GHz.

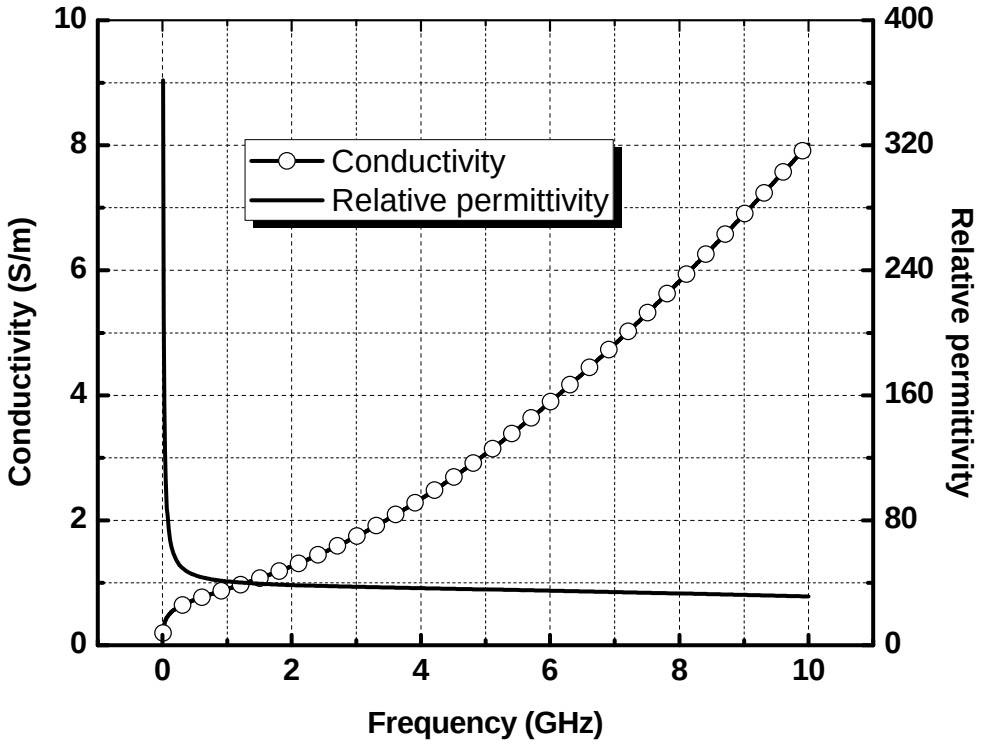
Conductivity
Relative permittivity
Conductivity (S/m)
Relative permittivity
Frequency (GHz)
0
2
4
6
8
10
0
80
160
240
320
400

(a)

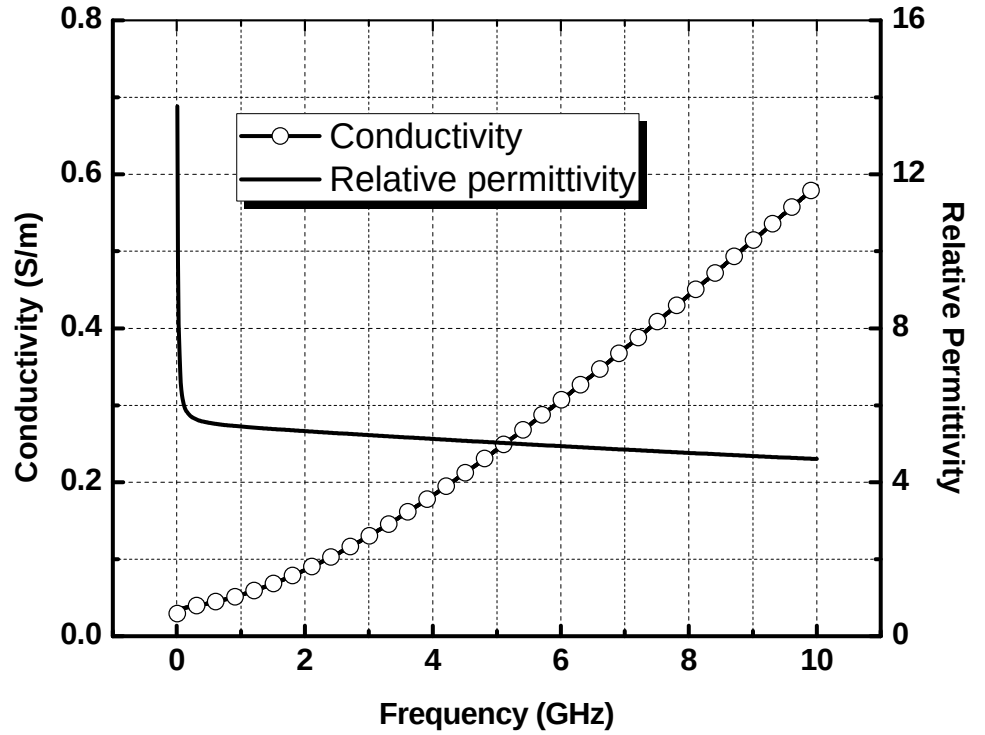
Conductivity
Relative permittivity
Conductivity (S/m)
Relative Permittivity
Frequency (GHz)
0.0
0.2
0.4
0.6
0.8
0
4
8
12
16

(b)

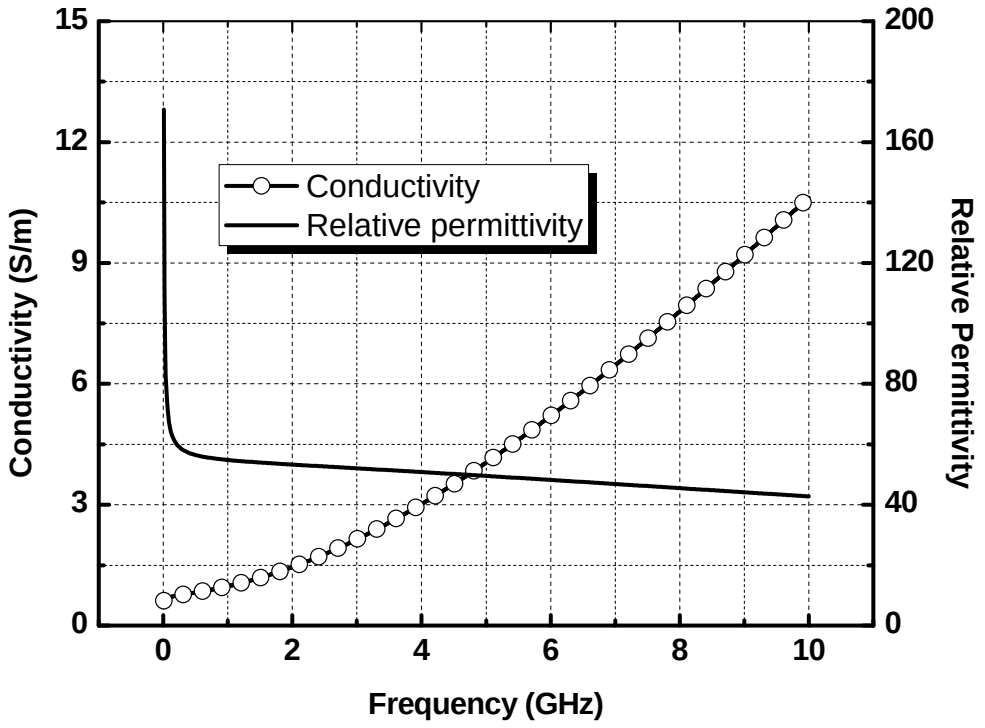

(c)

Figure 1-4 Relative permittivity and conductivity of (a) skin-dry (b) fat (c) muscle [44].

From the figure, we can see that three tissue materials are all quite lossy, mainly contributed by conductive loss, especially at higher frequency range. Also, the permittivity is quite large compared to most substrate materials. It helps in reducing the size of an implantable antenna but also reducing its gain. Additionally, we can see that the dielectric properties of skin are closer to muscle, while fat has a much lower relative permittivity.

Tissue model composed of these three layers is often used to evaluate the performance of an implantable antenna. Also one layer model of skin or muscle is also frequently adopted. From our experience, the size of tissue model does not have a big influence on the reflection coefficient of implantable antennas. However, it will influence their gain and radiation pattern.

Additionally, human models such as three-dimensional FDTD head model and shoulder model are used in previous work [26]. Because the actual human model is composed of many delicate tissue voxels, the simulation of which

would be quite time-consuming even for workstations. Therefore for the saving of simulation time, often part of the human body rather than the whole human model is imported in the simulation software. And we list various human models from Computer Simulation Technology (CST) Microwave Studio in Table 1-3 as an example. And the figures for these human models are shown in Figure 1-5 [45]. We can see that the human models are quite complete, including baby, child, male adult, female adult and pregnant woman.

Table 1-3 CST human models

Model	Age/Sex	Size/cm	Mass/kg	Resolution / mm
Baby	8-week female	57	4.2	0.85 × 0.85 × 4.0
Child	7y female	115	21.7	1.54 × 1.54 × 8.0
Donna	40y female	176	79	1.875 × 1.875 × 10
Emma	26y female	170	81	0.98 × 0.98 × 10
Gustav	38y male	176	69	2.08 × 2.08 × 8.0
Laura	43y female	163	51	1.875 × 1.875 × 5.0
Katja	43y pregnant, 24w	163	62	1.775 × 1.775 × 4.84

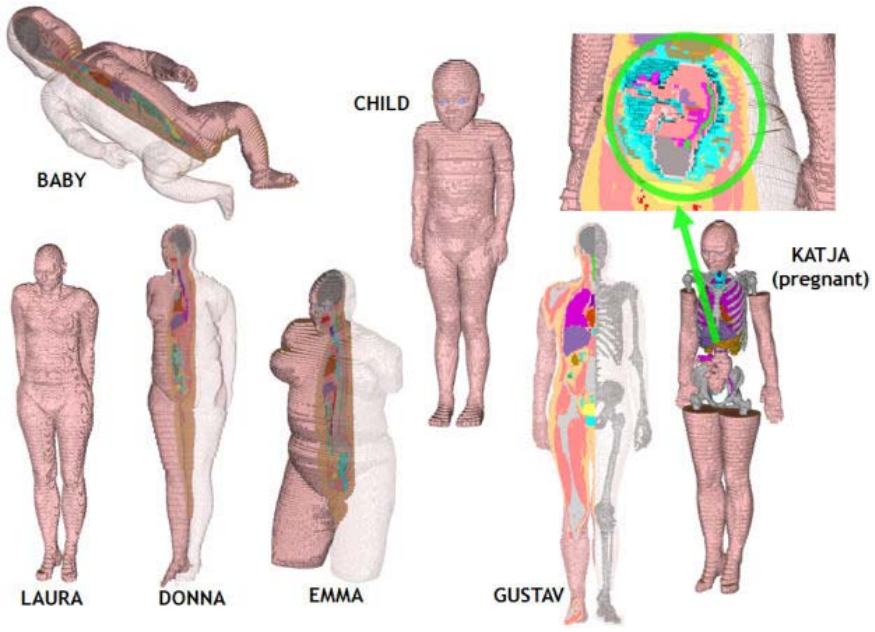

Figure 1-5 Various human models which can be used in CST simulation.

1.2.3 Safety Issues

For safety concerns, we should evaluate Specific Absorption Rate (SAR). The SAR is a measure of power absorbed by the human tissue exposed to electromagnetic radiation, which is also used to evaluate the heating issues brought by mobile phones previously. The definition of SAR can be given by

equation (1-1), the time derivative of the incremental energy (dW) absorbed by (dissipated in) an incremental mass (dm) contained in a volume element (dV) of given density (ρ). SAR is expressed in units of watts per kilogram (W/kg) [46].

$$\mathrm{SAR} = \frac{\mathrm{d}}{dt}\left(\frac{dW}{dm}\right) = \frac{d}{dt}\left(\frac{dW}{\rho dV}\right) \tag{1-1}$$

The standards for SAR are regulated by IEEE. IEEE C95.1-1999 standard stipulates that the maximum 1-g averaged SAR should not be larger than 1.6 W/kg, as averaged over any 1 g of tissue (defined as a tissue volume in the shape of a cube) [46]. However, the new C95.1-2005 standard defines the SAR with respect to 10-g averaged tissue, which should be less than 2 W/kg over a 10-g volume of tissue [47]. The new standard is much less stringent than the previous one.

1.3 Original Contributions and Thesis Outlook

The thesis covers a complete wireless link used for both wireless power transfer and data transmission, the organization of which can be summarized as follows:

Chapter 1: Introduction

This chapter firstly introduces the background for wireless telemetry system. Then it gives a complete list of the frequencies commonly used for communications between external systems and implanted devices, including power and data transmission purpose. Also human tissue properties and human models are introduced. Finally, safety issues concerning SAR evaluation are explained.

Chapter 2: Wireless Power Transfer for Rectangular Coils

Original contribution: this chapter not only provides a new and simple method for calculating the power efficiency for wireless power transfer, but also proposes a method of solving the practical problem for the optimization

of rectangular coils by using the filament method of calculating the self and mutual inductance.

Description: The wirelessly coupled coils are crucial for efficient power transmission in various applications, and the rectangular coils' advantage lies in two aspects. For one thing, compared with circular or elliptic coils, rectangular or square coils have larger coupling area with the same horizontal and vertical dimensions. For another, during some practical applications, the space left for power coils design presents a certain shape other than spiral and square. In this case, rectangular coils serves as a more general and favorable alternative. In this chapter, rectangular coils are characterized and optimized by lumped component model. The design procedure was executed in Matlab, and validated by simulation from HFSS and measurement from a network analyzer.

Chapter 3: Differentially Fed Dual Band Implantable Antenna Operating near MICS Band for Wireless Neural Recording Applications

Original Contribution: A novel implantable antenna is proposed to realize both differential feeding and dual-band operation for the first time.

Description: This chapter proposes a differentially fed dual-band implantable antenna for neuro-recording application operating near MICS band for the first time. The antenna can be connected with a Burst-Mode Injection-Locked Complementary Metal–Oxide–Semiconductor (CMOS) transmitter based Frequency-shift keying (FSK), and it operates at two center frequencies of 433.92 MHz and 542.4 MHz, which are both close to the MICS band, to support sub-GHz wideband communication for high-data rate implantable neural recording application. The SAR distribution and the communication link budget are also examined. Finally, co-testing results with the transmitter connected before the differential antenna of the communication link are presented.

Chapter 4: Differentially Fed Dual Band Implantable Antenna Operating at MICS Band and ISM Band

Original contribution: this chapter proposes a differentially fed dual-band implantable antenna with biocompatible insulation operating at both 403 MHz MICS and 2.45 GHz ISM bands for the first time. The antenna is firstly proposed in a planar form, and its possible use in flexible form for capsule application is also evaluated. The bandwidth of this antenna is much larger than the one proposed in previous chapter.

Description: antennas with dual band capability can be used in a system with two modes: sleep mode and wake-up mode, reducing the energy consumption and extending the lifetime of the implant. Also, an antenna with differential configuration can be directly connected to a transmitter with differential outputs, eliminating the loss introduced by baluns and matching circuits. Finally, in vitro test in minced pork are performed to test the reliability of the antenna in real implantation cases.

Chapter 5: Interference Evaluation for Power and Data Link

Original contribution: Previous work only deals with interference with both power link and data link composed of coil pairs. This chapter presents the investigation of the mutual effect between coupling coils and coupling antennas for biomedical applications for the first time.

Description: For neuro-recording systems, as the bandwidth requirement for data coils is larger, we use coupling antennas operating at MICS band rather than several megahertz for data transfer. Due to the possible close distance between the power link and the data link, the performance of each other may be affected. In this chapter, the interference between power link and data link immersed in human tissue model is evaluated.

Chapter 6 Conclusion

This chapter gives the conclusion remarks and the future work that can be performed.

Chapter 2

Wireless Power Transfer for Rectangular Coils

2.1 Introduction

During recent years, wireless sensor networks [48] and near-field communication systems [49], [50] have been gradually drawing the attention of researchers. In all these systems, the communication link is realized by either far-field wideband antennas [51], [52] or near-field inductive coils and antennas. And wireless power transfer plays an important role. For instance, wireless power transfer can be applied in portable telephone battery chargers [53]. Also, they can be realized in a system for monitoring conduit obstruction [54], and sometimes they are in the shape of a wireless capsule for endoscopy [55]. Furthermore, wireless power transfer can be utilized in an online electric vehicle [56].

In this chapter, we focus on the link intended for power transmission. Wireless power transfer is achieved by two inductively coupled coils transferring energy from one coil to the other. Also, if a rechargeable battery is connected to the secondary coil, this power link acts as a vital part for wireless charging. It is obvious that how to enhance the power efficiency between these two coupled coils is the critical part during power transmission. Some early design works of inductive links were constructed by circular spiral coils made of filament wires in the form of single or multiple individually insulated strands [16], [21], [57], [58]. This type of filament wire is called Litz wire, which presents a smaller effective series resistance (ESR) and a larger quality factor, therefore enhancing the power transmission efficiency. However, this type of coil cannot be batch-fabricated without sophisticated fabrication

technology. Other wireless links were constructed by lithographically defined square spiral coils [17], [18], [59]. Some of the coils are based on rigid substrates such as printed circuit board (PCB), and others are based on flexible substrates such as polyimide [60] or parylene [61]. For the design procedure, some systematic design methods for optimizing the coils were proposed [17], [62]. However, none of them are suitable for improving the efficiency between rectangular coils. Because for one thing, rectangular or square coils has larger coupling area compared with circular or elliptic coils with the same horizontal and vertical dimensions. For another, during some practical applications, the space left for power coils design presents a certain shape other than spiral and square. In this case, rectangular coils serves as a more general and favorable alternative. Additionally, previous expression of mutual inductance for square coils is based on an experiment-based coefficient adapted from circular coils [17], which proves inefficient when applied in the case of rectangular coils. In this chapter, we propose a new method for calculating the mutual inductance and present a method of how to characterize and optimize rectangular coils used in inductive link, and a transferring frequency of 3 MHz is assumed.

Because the simulation of multi-turn coil pairs in HFSS consumes a very large memory and a considerable amount of time even for work stations, therefore we can first build up some lumped component models for the coils. Subsequently, these models are programmed into Matlab and we utilize these Matlab codes to determine the initial values of the coils' geometrical parameters, which is much faster than Finite element-Method (FEM) based HFSS simulation. Eventually, we can use HFSS to do the final adjustments to further improve the efficiency. Therefore the advantage of our design method is due to the fact that it can speed up the design process and help us determine the geometrical parameters of the coils intended for power transfer efficiently.

With the coil being modeled as an inductor in series with a resistor, the usually adopted schematic for an inductive link is a serial-parallel type circuit, as shown in Figure 2-1. The primary circuit is in serial resonance to provide a low-impedance load to the source connected before the primary coil, and the

secondary circuit is in parallel resonance at the same frequency to better drive a nonlinear rectifier load [63].

In Section 2.2, we propose a simple equation for calculating the efficiency and evaluate the effect of various lumped component on the inductive link. Then in Section 2.3, we give the equations for the modeling of self inductance, mutual inductance, resistance due to skin effect and parasitic capacitance. Subsequently, in Section 2.4, a systematic design procedure executed in Matlab (MathWorks, Natik, MA) has been put forward for optimizing rectangular coils, with verification from simulation of HFSS (Ansoft, Pittsburgh, PA) and measurement results. The comparison of results from three approaches is presented in Section 2.5, followed by conclusion remarks in Section 2.6. The preliminary results have been presented [19].

2.2 Power Efficiency

2.2.1 Power Efficiency

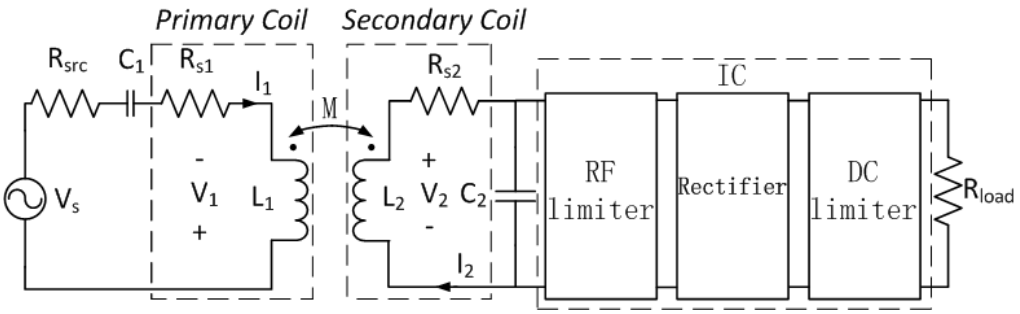

Figure 2-1 The equivalent circuit schematic of wirelessly coupled system with lumped elements.

Different ways for calculating power efficiency have been proposed [21], [22], [62], [64], [65]. Here we present a simple and accurate way of calculating the efficiency. From Figure 2-1, if we omit the IC part, we can get a simplified schematic diagram, as shown in Figure 2-2 (a).

For the secondary coil, we do a parallel-to-series conversion (from Figure 2-2 (a) to Figure 2-2 (b)), which is called narrowband approximation, and it is shown that the error caused by this approximation is negligible [62]. From Lee [66], we can get

$$L_{p2} = L_2\left(1+Q_2^{-2}\right) \approx L_2 \tag{2-1}$$

$$R_{p2} = R_{S2}\left(1+Q_2^{2}\right) \approx R_{S2}Q_2^2 = \omega^2 L_2^2 / R_{s2} \tag{2-2}$$

where $Q_2 = \omega L_2/R_{s2}$ is usually much larger than 1 (During our application, the typical value for Q is around 20 ~ 60).

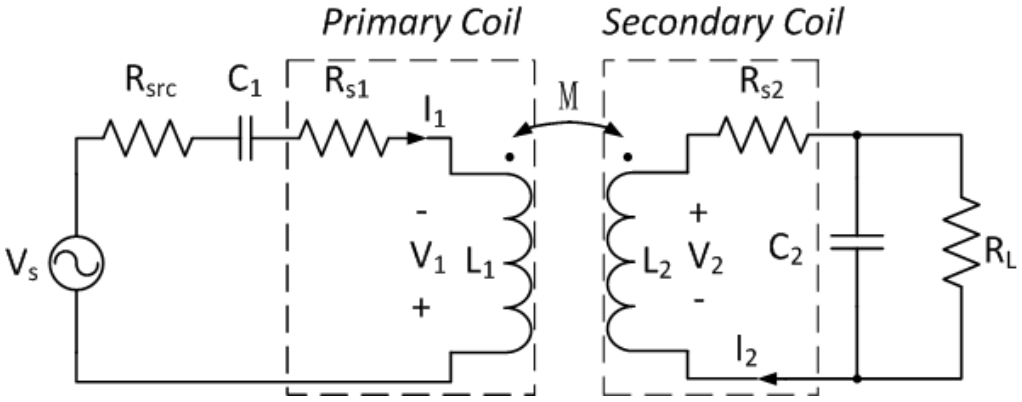

(a)

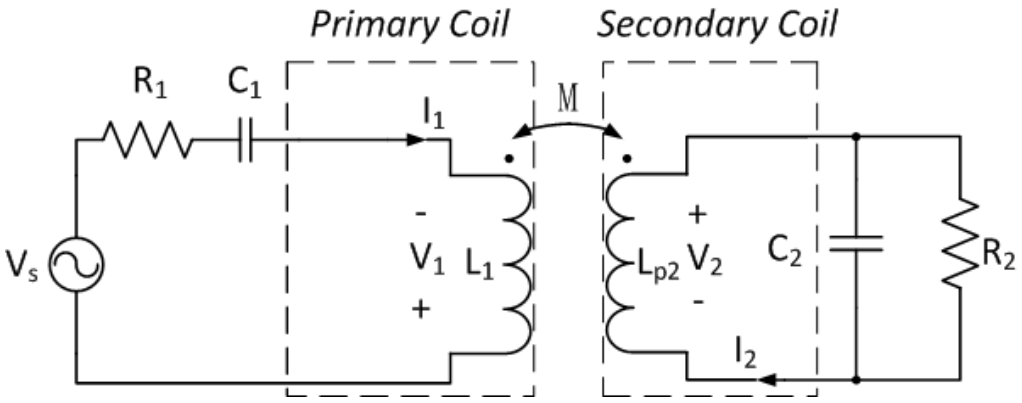

(b)

Figure 2-2 (a) The original schematic for inductive link without the IC part. (b) The schematic after we do a parallel-to-series conversion.

The R_1 and R_2 in Figure 2-2 (b) are defined as

$$R_1 = R_{src} + R_{s1} \tag{2-3}$$

$$R_2 = R_L \left\| R_{p2} \right. \tag{2-4}$$

where R_{src} is the source resistance.

From Figure 2-2 (b), we can get

$$\begin{bmatrix} V_s \\ 0 \end{bmatrix} = \begin{bmatrix} Z_1 & -j\omega M \\ -j\omega M & Z_2 \end{bmatrix} \begin{bmatrix} I_1 \\ I_2 \end{bmatrix} \tag{2-5}$$

where

$$Z_1 = R_1 + j\omega L_1 + 1/\left(j\omega C_1\right) \tag{2-6}$$

$$Z_2 = j\omega L_{p2} + 1/\left(1/R_2 + j\omega C_2\right) \tag{2-7}$$

M is the mutual inductance between two coupling coils. From equation (2-5), after some mathematical manipulations, we can arrive at

$$V_s = \left[Z_1 + \frac{\left(\omega M\right)^2}{Z_2} \right] I_1 \tag{2-8}$$

Therefore the reflected resistance from secondary side to primary side is

$$R_{reflect} = \mathrm{Re}\left[\frac{\left(\omega M\right)^2}{Z_2} \right] = \frac{\left(\omega M\right)^2 R_2}{L_{p2}^2\omega^2 + R_2^2\left(C_2 L_{p2}\omega^2 - 1\right)^2} \tag{2-9}$$

The power efficiency is defined as the power received by the load divided by the power provided by the source, and because reactive component will not dissipate power, the efficiency can be expressed as

$$\begin{aligned} \eta &= \frac{R_{reflect}}{R_1 + R_{reflect}} \frac{R_{p2}}{R_{p2} + R_L} \\ &= \frac{k^2 L_1 L_{p2} R_2}{R_1 L_{p2}^2 + R_1 R_2^2 \left(C_2 L_{p2}\omega - \frac{1}{\omega} \right)^2 + k^2 L_1 L_{p2} R_2} \frac{R_{p2}}{R_{p2} + R_L} \end{aligned} \tag{2-10}$$

where k is the coils coupling coefficient defined as

$$k = \frac{M}{\sqrt{L_1 L_2}} \tag{2-11}$$

When ω reaches $1/\sqrt{C_2 L_{p2}} \approx 1/\sqrt{C_2 L_2}$, η reaches maximum

$$\eta_{\max} = \frac{1}{1 + 1/\left(k^2 Q_1' Q_2'\right)} \frac{R_{p2}}{R_{p2} + R_L} \tag{2-12}$$

where $Q_1^{'} = \omega L_1 / R_1$ and $Q_2^{'} = R_2 / \omega L_{p2} \approx \mathrm{R}_2 / \omega L_2$. Because maximum efficiency is desired for power transfer, the whole circuit operates at its resonance mode.

2.2.2 Effect of C_1 on the Inductive Link

It can be seen from equation (2-12) that the efficiency at resonance is independent of the primary capacitor C_1. However, the voltage transfer ratio $|V_L/V_s|$ is a function of C_1. The expression of $| V_L/V_s |$ with respect to C_1 is too lengthy to be listed here, but the optimum C_1 where maximum $| V_L/V_s |$ is achieved can be found mathematically by a simple expression. At resonance, C_1 can be determined by the following equation.

$$C_1 = \frac{1}{\left(L_1 - \frac{k^2 L_1 L_2}{L_{p2}} \right) \omega^2} \approx \frac{1}{\left(1 - k^2\right) \omega^2 L_1} \tag{2-13}$$

And this equation tallies with the equation proposed in [62].

2.2.3 Effect of R_L on the Inductive Link

During the design process, a fixed R_L is assumed. However, after the coils according to a particular R_L are designed, we can further maximize the efficiency by an adequate changing of R_L.

From equation (2-12), the inverse of η_{max} can be expressed as a function of R_L

$$\mathrm{f}\left(R_L\right) = \frac{1}{\eta_{\max}} = 1 + \frac{2}{k^2 Q_1^{'} Q_2} + \frac{\omega L_2}{k^2 Q_1^{'}} \frac{1}{R_L} + \left(1 + \frac{1}{k^2 Q_1^{'} Q_2} \right) \frac{1}{R_{p2}} R_L \tag{2-14}$$

where $f\,(R_L)_{min}$ occurs at

$$\mathrm{R}_L = \sqrt{\frac{\omega L_2}{k^2 Q_1^{'}} \Bigg/ \left[\left(1 + \frac{1}{k^2 Q_1^{'} Q_2} \right) \frac{1}{R_{p2}} \right]} = \frac{R_{p2}}{\sqrt{k^2 Q_1^{'} Q_2 + 1}} \tag{2-15}$$

Therefore, if a matching circuit is designed to change the actual load to the value specified in equation (2-15), the efficiency will be enhanced. This method has been proved effective in [67].

2.2.4 Effect of R_{src} on the Inductive Link

As R_{src} increases, the efficiency will reduce. Therefore, this is no optimal value for R_{src}. However, R_{src} will have an influence on determining the geometrical parameters of the coils, for instance, the width of the coil trace. This would be explained in Step 3 of the design procedure elaborated in section 2.4.

2.3 Modeling

Previous papers dealing with inductive coils only covered circular coils made of Litz wires [16], [21], [57], [58] or square coils [17], [18], [59], [68]. Circular coils made of Litz wire present a smaller ESR and a larger quality factor, therefore boosting the final power transmission efficiency. However, due to the fact that this type of coils cannot be batch-fabricated without sophisticated fabrication technology, planar printed spiral coils are preferred. For this type of coils, considering the same horizontal and vertical dimensions, square coils have a larger coupling area than the circular ones and therefore found their application in many published papers. But still, square coils with same side lengths have their restrictions, limiting their use in the application when the space left for inductive coils design presents a different shape. In this circumstance, rectangular coils serve as a more general and favorable option. For instance, previous expression for the self inductance of square coils is expressed as [17], [68].

$$L=\frac{1.27\mu_0 n^2 d_{avg}}{2}\left[\ln\left(\frac{2.07}{\varphi}\right)+0.18\varphi+0.13\varphi^2\right] \tag{2-16}$$

$$\varphi=\frac{d_o-d_i}{d_o+d_i} \tag{2-17}$$

where n is the number of turns, d_o and d_i are the outer and inner diameters of the coil, and $d_{avg} = (d_o + d_i)/2$.

For this self inductance equation to be true, we should assume a uniform d_o for two side lengths, which is not the case for rectangular inductive power coils. Consequently, this equation is not applicable to rectangular cases. In

addition, previous equations for mutual inductance of square coils adopt an experiment-based coefficient from circular coils, which may cause error and become unusable for the case of rectangular coils. Therefore, for the calculation of self and mutual inductance of rectangular coils, we should use filament method based on the Greenhouse method [69].

2.3.1 Self Inductance

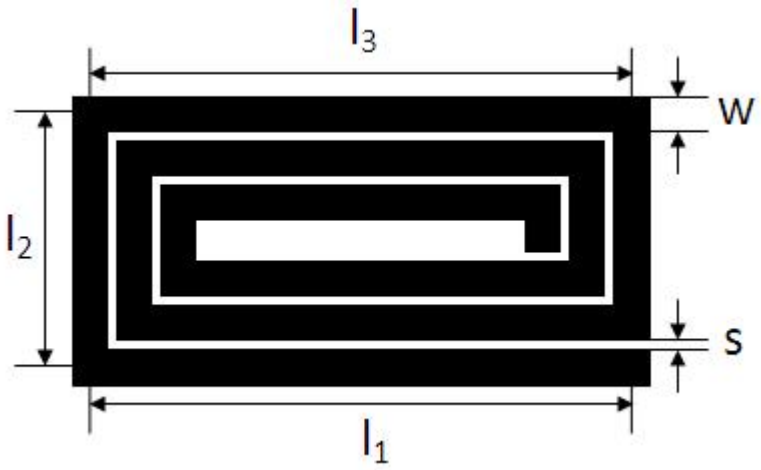

Figure 2-3 Geometrical parameters of a rectangular spiral coil.

Based on the Greenhouse method, the inductance of a rectangular coil can be obtained by summing up the self inductance of each segment, the positive and the negative mutual inductance between all pairs of segments. Also, this method is further used to calculate the inductance taking into account of the substrate eddy currents [70]. In this chapter, we further extend this method to calculate the mutual inductance between the primary rectangular coil and the secondary one, which is a novel approach and can be programmed into Matlab to determine the power efficiency quickly instead of time-consuming HFSS simulation.

For an n-turn rectangular coil shown in Figure 2-3, the length of one segment can be given by

$$l_i = \frac{l_1 + l_2 + (-1)^i (l_2 - l_1)}{2} - \left\langle \frac{i}{2} - 1 \right\rangle (w + s) \tag{2-18}$$

where <> denotes the integer part of the expression in brackets and i denotes the segment number (from outmost to innermost). The total self inductance can be determined by [69]

$$L_s = \sum_{i=1}^{4n} L_i = \sum_{i=1}^{4n} \frac{\mu_0}{2\pi} l_i \left[\ln\left(\frac{2l_i}{w+t} \right) + 0.5 + \frac{w+t}{3l_i} \right] \tag{2-19}$$

where L_i denotes one segment's self inductance. From [71], we can get the mutual inductance between two parallel wire segments with lengths l_i and l_j

$$M_{i,j} = M\left(l_i + \delta\right) - M\left(\delta\right) \tag{2-20}$$

where

$$M(l) = \frac{\mu_0}{2\pi} l \left\{ \ln\left[\frac{l}{GMD} + \sqrt{1 + \left(\frac{l}{GMD} \right)^2} \right] - \sqrt{1 + \left(\frac{GMD}{l} \right)^2} + \frac{GMD}{l} \right\} \tag{2-21}$$

$$GMD = \exp\left(\ln d - \frac{w^2}{12d^2} - \frac{w^4}{60d^4} - \frac{w^6}{168d^6} - \frac{w^8}{360d^8} - \frac{w^{10}}{660d^{10}} \right) \tag{2-22}$$

$$\delta = \left(l_j - l_i\right) / 2 \tag{2-23}$$

Consequently, the positive mutual inductance between segments can be calculated by

$$M_{T+} = 2 \sum_{i=1}^{n} \sum_{j=i+1}^{n} \sum_{k=1}^{4} M_{4(i-1)+k,4(j-1)+k} \tag{2-24}$$

where i, j indicate the turn number (from outermost to innermost), k is the segment number in that turn. The distance between them can be given by

$$d_+ = \left(j - i\right)\left(w + s\right) \tag{2-25}$$

The negative mutual inductance between segments can be calculated by

$$M_{T-} = 2 \sum_{i=1}^{n} \sum_{j=1}^{n} \sum_{k=1}^{2} M_{4(i-1)+k,4(j-1)+k+2} \tag{2-26}$$

The distance between them can be given by

$$d_{-} = \frac{l_1 + l_2 + (-1)^i (l_1 - l_2)}{2} - (i + j - 2)(w + s) \tag{2-27}$$

Therefore, the total inductance of a rectangular coil can be obtained by

$$L = L_S + M_{T+} - M_{T-} \tag{2-28}$$

2.3.2 Mutual Inductance

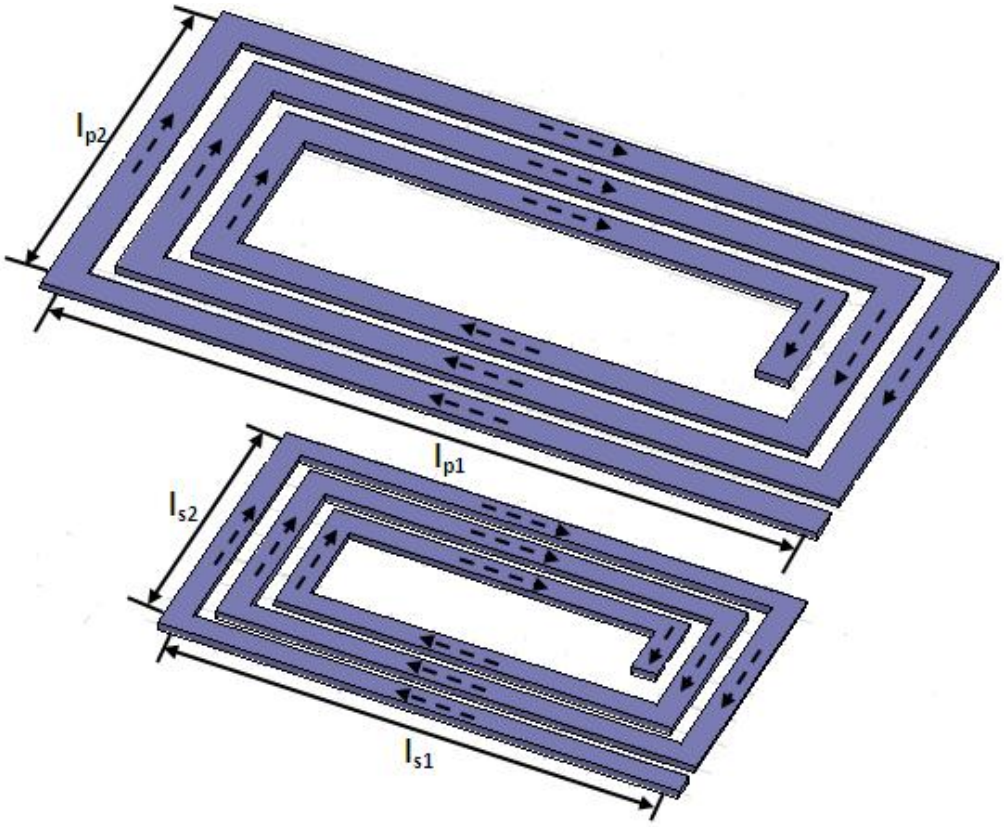

Figure 2-4 Mutual inductance between the primary coil and secondary coil, and the arrow in the traces indicates the direction of current.

Subsequently, we can get the mutual inductance between primary and secondary coil by summing up all the mutual inductance between all pairs of segment. From Figure 2-4, we can see that those segments with current of same direction would have a positive mutual inductance, and segments with current of opposite direction would have a negative mutual inductance. For example, l_{p2}, l_{p6}, l_{p10} and l_{s2}, l_{s6}, l_{s10} would have positive mutual inductance, l_{p2}, l_{p6}, l_{p10} and l_{s4}, l_{s8}, l_{s12} would have negative mutual inductance.

Now we can get the distance between one segment and center of the rectangular coil, for the primary coil

$$d_1(i) = \frac{l_{p1} + l_{p2} + (-1)^i (l_{p1} - l_{p2})}{4} - \left\langle \frac{i-1}{4} \right\rangle (w_1 + s_1) \tag{2-29}$$

For the secondary coil

$$d_2(i) = \frac{l_{s1} + l_{s2} + (-1)^i (l_{s1} - l_{s2})}{4} - \left\langle \frac{i-1}{4} \right\rangle (w_2 + s_2) \tag{2-30}$$

where subscript 1 or *p* denotes the parameters of the primary coil, and 2 or *s* denotes those of the secondary coil.

From Figure 2-4, we can see that positive mutual inductance (the mutual inductance between traces with current of same direction) can be calculated by

$$M_+ = \sum_{i=1}^{n1} \sum_{j=1}^{n2} \sum_{k=1}^{4} M_{4(i-1)+k,4(j-1)+k} \tag{2-31}$$

Assuming that the coils are perfectly aligned along the center, the distance between segments can be given by

$$d_+ = \sqrt{\left[d_1(4(i-1)+k) - d_2(4(j-1)+k) \right]^2 + D^2} \tag{2-32}$$

where *D* is the distance between primary coil and secondary coil along the center axis.

Negative mutual inductance can be calculated by

$$M_- = \sum_{i=1}^{n1} \sum_{j=1}^{n2} \sum_{k=1}^{4} M_{4(i-1)+k,4(j-1)-k+(-1)^k+5} \tag{2-33}$$

The distance between them can be given by

$$d_- = \sqrt{\left[d_1(4(i-1)+k) - d_2(4(j-1)-k+(-1)^k+5) \right]^2 + D^2} \tag{2-34}$$

During the calculation of mutual inductance between a pair of segments, the widths of these two segments have to be the same equation (2-28). However, in actual cases, the widths of segments for the secondary and primary coil are not always the same. Therefore, we made an approximation here by assuming

$$w = \frac{w_1 + w_2}{2} \tag{2-35}$$

Eventually, the total mutual inductance of two rectangular coils would be obtained by

$$M = M_+ - M_- \tag{2-36}$$

2.3.3 Serial Resistance

For the resistance of coils, two factors need to be taken into consideration. One is the resistance caused by skin effect, and the other one is the proximity effect or current crowding effect. Resistance caused by skin effect has been included in our model. The proximity effect has been investigated [18], [72], which is more pronounced when the operating frequency approaches 10 MHz for the coil size of our case. Because our operating frequency is only 3 MHz, we neglect this in our model. The AC resistance caused by skin effect can be expressed as [18], [73].

$$R_S = \frac{\sum_1^{4n} l_i}{w\sigma t_{eff}} = \frac{\sum_1^{4n} l_i}{w\sigma\delta\left(1 - e^{-t/\delta}\right)\left(1 + t/w\right)} \tag{2-37}$$

where t is the thickness and w is the width of the copper, and t_{eff} is the effective thickness due to skin effect. l_i is defined in equation (2-18), and δ is the skin depth of the conductor given by

$$\delta = \sqrt{\frac{2}{\omega\mu\sigma}} \tag{2-38}$$

2.3.4 Parasitic Capacitance

For the parasitic capacitance, we use the empirical equation proposed in [17].

$$C_P = C_{pc} + C_{ps} \approx \left(\alpha\varepsilon_{rc} + \beta\varepsilon_r\right)\varepsilon_0 \frac{t}{s} l_g \tag{2-39}$$

where C_{pc} is the capacitance through air and C_{ps} is the capacitance through substrate. ε_{rc} and ε_r are the dielectric constant of the copper and substrate

respectively. α and β are empirically determined coefficient for the capacitance proportion. l_g is the length of the gap, given by the following equation

$$l_g = \sum_{i=1}^{4(n-1)} \frac{l_1 + l_2 - (w+s) + (-1)^i (l_2 - w - s - l_1)}{2} - \left[\frac{i}{2} - 1\right](w+s) \quad (2\text{-}40)$$

2.3.5 Efficiency Calculation

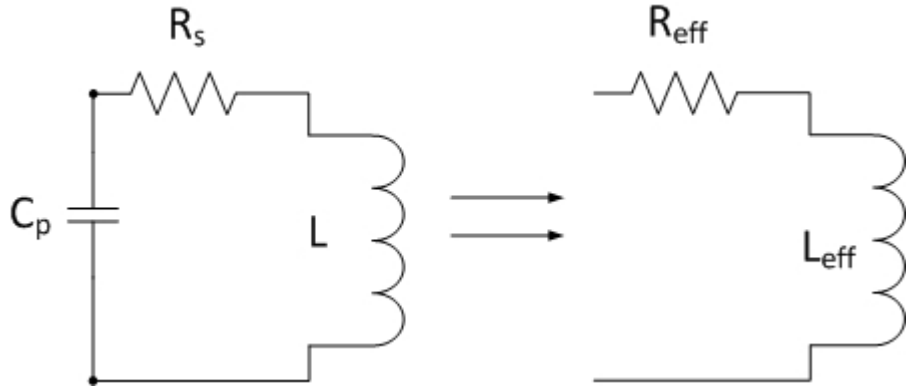

Figure 2-5 Equivalent transformation.

After the model for the coil has been set up, we can do an equivalent transformation as shown in Figure 2-5 and substitute L_{eff} and R_{eff} into (12) to calculate the final efficiency, where

$$R_{eff} = \frac{R_s}{1 - 2C_p L\omega^2 + C_p^2\omega^2\left(R_s^2 + L^2\omega^2\right)} \quad (2\text{-}41)$$

$$L_{eff} = \frac{L - C_p R_s^2 - C_p L^2\omega^2}{1 - 2C_p L\omega^2 + C_p^2\omega^2\left(R_s^2 + L^2\omega^2\right)} \quad (2\text{-}42)$$

2.4 Design Procedure

Design procedures have been proposed in [17], [62]. In this chapter, we take a similar method. The complete flowchart for the design procedure is shown in Figure 2-6.

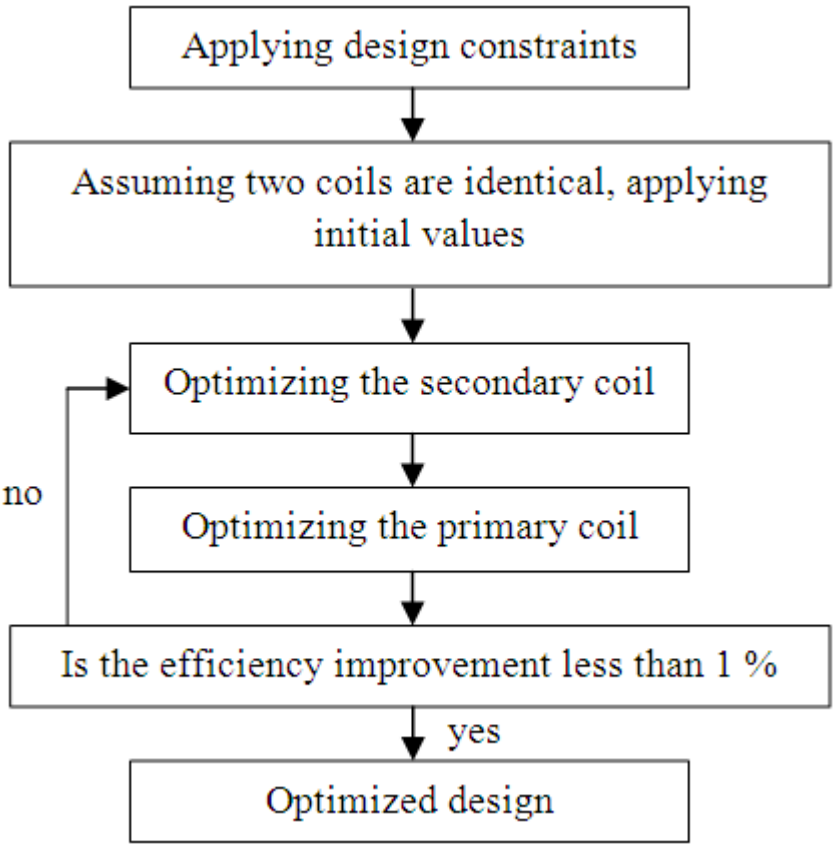

Figure 2-6 Flowchart for the design procedure.

2.4.1 Step 1: Applying Design Constraints

Design constraints are generally imposed by fabrication technology (minimum width) and the space available for secondary coils. Here we list all the parameters in Table 2-1.

From HFSS simulation, we found that the substrate has insignificant effect on the value of mutual inductance and other parameters that would cause a difference in the final efficiency. Therefore we used the substrate of commonly available FR4 to support the coils. This may be due to the fact that near-field induction is largely a magnetic coupling, considering most materials are non-magnetic, any supporting substrate will not cause any significant change on the simulation and measurement result.

Table 2-1 Design constraints

Parameter	Symbol	Value
Linking frequency	f	3 MHz
Maximum dimension for secondary coil	$a \times b$	25 mm×10 mm
Minimum conductor width	w_{min}	0.1 mm
Minimum conductor spacing	s_{min}	0.1 mm
Source resistance	R_{src}	3 Ω
Loading resistance	R_L	1000 Ω
Distance between the coils	D	10 mm
Conductor thickness	t	1 oz ≈ 35 μm
Conductor conductivity (copper)	σ	5.8×10^7 S·m^{-1}
Substrate thickness (FR4)	t_s	0.8 mm
Substrate dielectric constant	ε_r	4.4

2.4.2 Step 2: Initial Values

We first assume that two coils are identical. And we initialize the parameters as $l_{p1} = l_{s1} = 25$ mm and $l_{p2} = l_{s2} = 10$ mm. For the spacing between turns, we just keep it at the minimum value for improvement of efficiency and coupling [17], [62]. Also, we introduce a ratio r to ensure the length of innermost segment is larger than 0, which is defined as

$$r = \frac{l_{4n}}{l_2} \tag{2-43}$$

By substituting equation (2-18) into equation (2-43), we can get

$$n = \frac{1}{2}\left[\frac{(1-r)l_2}{w+s} + 1\right] \tag{2-44}$$

2.4.3 Step 3: Optimizing Secondary Coil

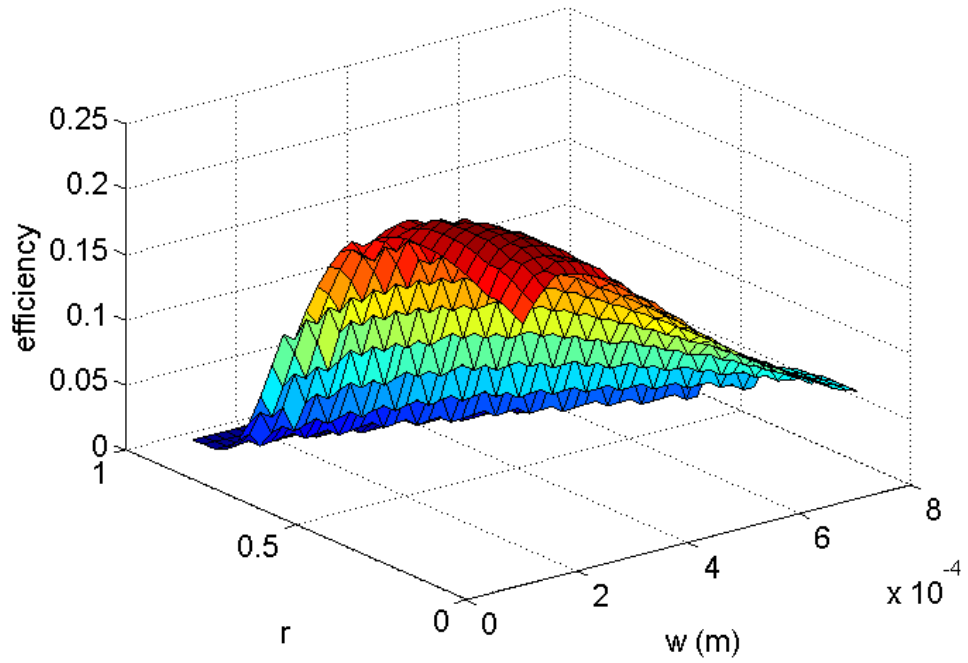

(a)

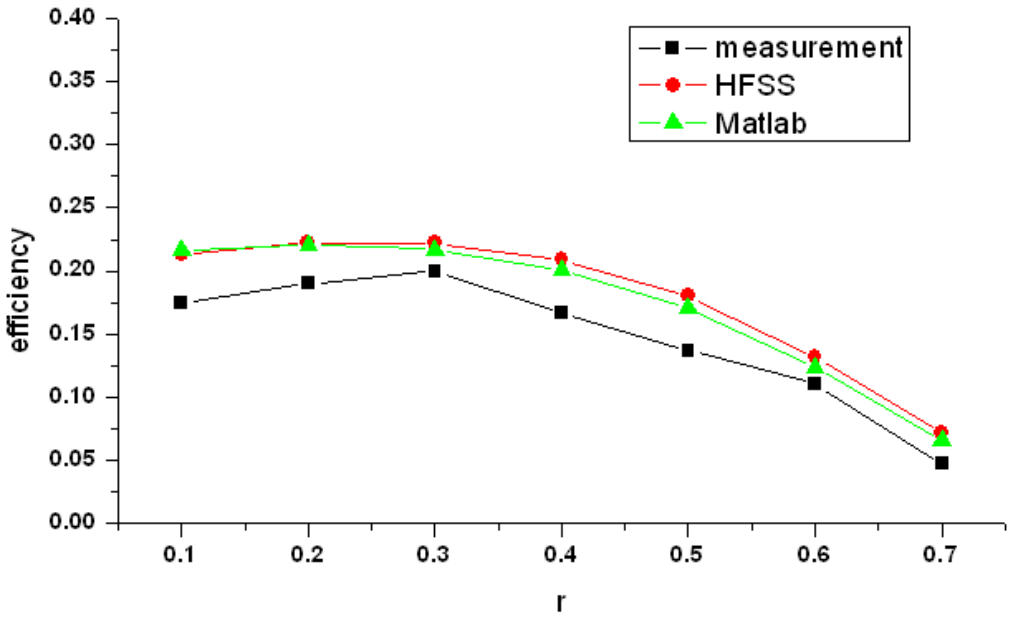

(b)

Figure 2-7 Optimize the *r* ratio and *w* of coil while assuming the dimensions for the secondary and primary coil are the same. (a) Efficiency versus *r* and *w*. (b) Efficiency versus *r* assuming *w* = 150 mm.

For a rectangular coil, there are five geometrical parameters: l_1, l_2, w, s and r. And the parameter n (number of turns) is interrelated with the defined ratio r, as shown in equation (2-44). Now we can plot the efficiency versus the left two variables w and r in Matlab to find out the optimum geometrical parameters.

From the curve shown in Figure 2-7 (a) and the result of Matlab code, we can see that at w = 150 μm, r = 0.21, and a maximum efficiency of 24.2% is achieved. In order to validate the results, we assume a fixed value 150 μm for w, and vary r from 0.1 to 0.7. We get the comparison curves from three approaches shown in Figure 2-7 (b). The calculated, simulated and measured efficiency agree with each other reasonably. And from the results, we can see that as r is further reduced below a certain value (in our case, it is around 0.2 ~ 0.3), which means more turns in the center of coils, the efficiency remains almost the same or reduces by a small amount. This agrees with the conclusion in [16], [17] that turn very close to the center of the coils does not help in increasing the coupling and the final efficiency.

For the impact of R_{src} on the power efficiency, we changed R_{src} from 0 to 10 Ω, and we found that the best w where maximum efficiency is achieved varies from 0.22 mm to 0.12 mm. This means that when the outer dimension is fixed, if there is a larger source resistance, we should decrease w to increase the overall quality factor. This is because that when a large source resistance is present, a smaller w means both a larger resistance and a larger inductance, but the inductance increasing is faster compared to the resistance increasing, therefore leading to a larger overall quality factor and a large efficiency accordingly.

2.4.4 Step 4: Optimizing Primary Coil

As the size limitation for primary coil is less stringent, after the secondary coil is fixed, we can increase the dimension of primary coil to further increase the efficiency. In this step, we assume $r_1 = r_2 = 0.21$ and the ratio of l_2/l_1 for the primary coil remains at 0.4 as the secondary coil.

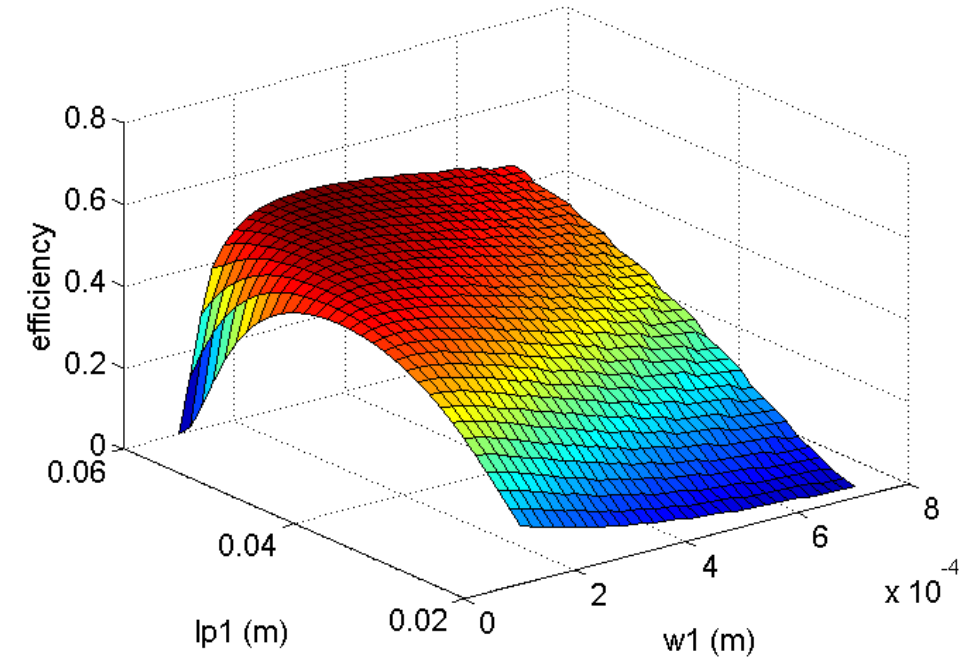

(a)

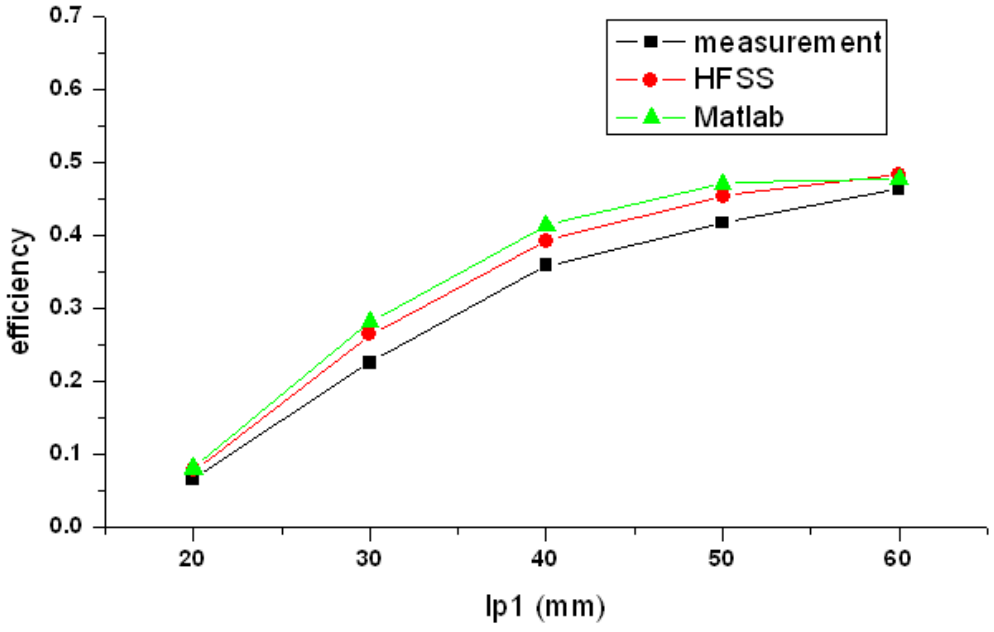

(b)

Figure 2-8 Optimize the outer dimensions l_{p1} and w_1 of primary coil. (a) Efficiency versus l_{p1} and w. (b) Efficiency versus l_{p1} assuming w_1 = 250 mm.

From the curve shown in Figure 2-8 (a), we can see that as we increase the outer dimension l_{p1}, the efficiency increases gradually. However, beyond a certain point, in our case l_{p1} = 60 mm, the efficiency remains almost the same, which is around 48%, as shown in Figure 2-8 (b). For w_1 < 200 mm, the

efficiency reduces sharply when l_{p1} is larger than 50 mm. Because when w_1 is extremely small, for the same size constraint of the external coil, the number of turns will increase. Therefore smaller cross-section of the metal trace will lead both to a larger resistance and a larger inductance, but the previous effect would be more significant, leading to the reduction of the Q factor and the power efficiency.

2.4.5 Step 5: Optimized Design

Table 2-2 Geometrical parameters of optimized coils

	l_1 (mm)	l_2 (mm)	w (mm)	s (mm)	n
primary coil	60	24	0.25	0.1	27
secondary coil	25	10	0.15	0.1	16

For our design iteration, the further increase in the size of external coil does not help a lot in increasing the efficiency, and the optimized parameters for coupling coils are summarized in Table 2-2.

2.5 Measured Performance

Figure 2-9 Fabricated coupling coils with supporting and connecting materials.

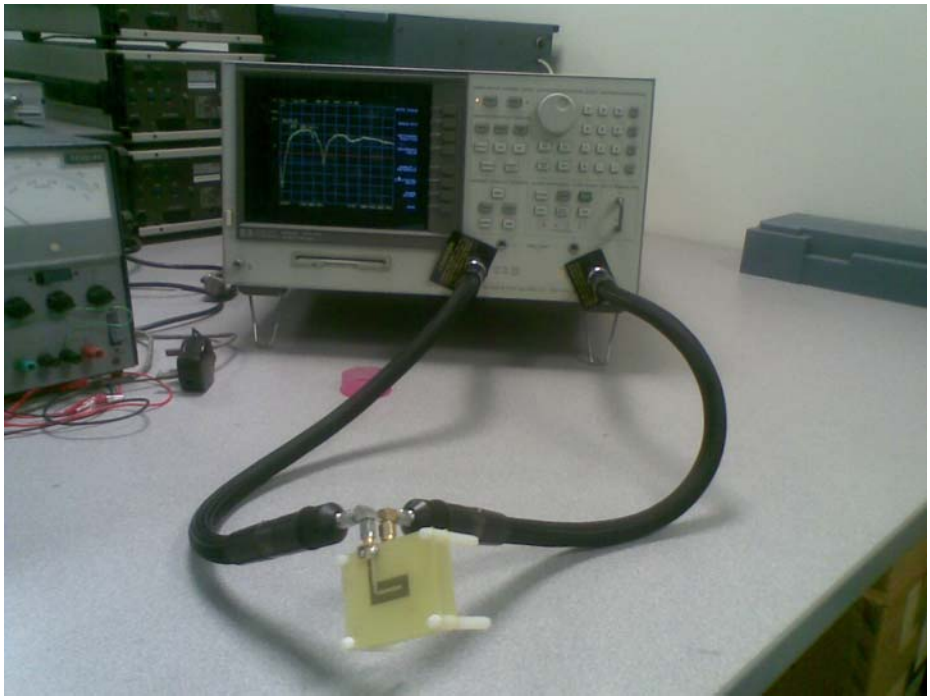

Figure 2-10 Measurement setup for the coupling coils.

The fabricated coupling coils are shown in Figure 2-9. From the figure, we can see some holes at the corners of the substrate, through which we can use some plastic fixtures to support and separate the coupling coils. The measurement setup is shown in Figure 2-10. For the measurement process, first, network analyzer (HP 8753D) was used to measure the S-parameters of the coupling coils. Subsequently, the S-parameters were converted to Z-parameters which contain the information of self-inductance, mutual inductance and serial resistance. Finally, an equivalent circuit of Figure 2-2 (a) was set up in ADS (Advanced Design System) to find the power efficiency. The comparison results from three approaches are shown in Table 2-3.

From Table 2-3, we can see that except a slight overestimation of L_1 and therefore an overestimated Q_1, all the other parameters from three different approaches agree with each other excellently. The quality factor of the secondary coil is only around 25. Due to size limitation, and the quality factor of the primary coil is between 45 and 55. Both of them satisfy the condition for the simplification process in equations (2-1) and (2-2) of Section 2.2.

Table 2-3 Comparison results from three approaches of optimized coils

	Calculated results	**Simulated results**	**Measured results**
M	1.101 μH	1.142 μH	1.141 μH
L_1	38.88 μH	33.60 μH	34.34 μH
L_2	4.78 μH	4.74 μH	4.79 μH
R_{s1}	13.43 Ω	13.63 Ω	14.10 Ω
R_{s2}	3.62 Ω	3.66 Ω	3.60 Ω
Q_1	54.6	46.5	45.9
Q_2	24.9	24.4	25.1
k	0.081	0.090	0.089
η	47.8 %	48.3 %	46.4 %

The final optimized efficiency given by measurement result is 46.4%, presenting a slight difference from Matlab calculation and HFSS simulation. The main reason is that for the self inductance and mutual inductance, the results from three methods agree well with each other, however, for the resistance, simulation and calculation method lead to underestimated result when compared to measurement most of the time, leading to a smaller measured efficiency. In all, the difference between different approaches may be caused by the following factors: 1) the inherent inaccuracy of the equation proposed to model the rectangular coil. Some secondary effect, for instance, the current crowding effect has not been included in our model 2) The SubMiniature version A (SMA) connector will introduce some resistance which was neglected both in simulation and calculation method 3) the inevitable misalignment between the coils will cause some reduction in efficiency.

2.6 Conclusion

Unlike previous methods which are only suitable for optimizing square or circular coil, we have proposed a method of how to model and optimize the geometrical parameters of rectangular coils for power transmission, which can be used in a wider scope of application. Our major contribution lies on two aspects: (a). we provide a new and simple method for calculating the power

efficiency; (b). we propose a method of solving the practical problem for the optimization of rectangular coils by using the filament method of calculating the self and mutual inductance.

The design procedure was executed in Matlab, and validated by simulation from HFSS and measurement from network analyzer. The advantage of this design method lies on the fact that with the help of Matlab codes, we can first determine the initial values for geometrical parameters of coupled coils in a more rapid way, sparing the effort of the time-consuming HFSS simulation. After the initial parameters of the coils have been decided, then we can use HFSS to do some final adjustments to the coils' geometrical parameters to further enhance the efficiency.

Chapter 3

A Differentially Fed Dual Band Implantable Antenna Operating near MICS Band for Wireless Neural Recording Applications

3.1 Introduction

Implantable microsystems are gradually becoming the focus of research, in which the wireless link acts as a vital role in the communications between the implants and the external devices. In this chapter, we focus on the link intended for data transfer, i.e. the implanted antennas.

Early works of implantable antennas are in the form of a microstrip antenna or a planar inverted-F antenna (PIFA), operating at a single frequency band, which is 402-405 MHz MICS band [26], [27]. In recent years, dual-band implanted antennas emerged. C.-M. Lee etc. proposed a π-shape antenna with double L-strips operating at two closely spaced frequencies of 375 MHz and 427 MHz to enhance the bandwidth [29]; T. Karacolak etc. proposed an antenna with serpentine configuration operating at 402-405 MHz MICS band and 2.4-2.48 GHz ISM band [9]; C. J. Sánchez Fernández etc. adopted a microstrip patch antenna based on short-circuited ring and spiral resonators, also operating at MICS and ISM bands [74]. The design and realization of a 3D-spiral small antenna was also proposed at MICS band [33]. Most recently, a triple-band implantable antenna was proposed, operating at 402 MHz, 433 MHz and 2.45 GHz [75]. Additionally, due to the size limitation of implantable antennas, stacked structures were also adopted [28], [74], [75][39].

In this chapter, we propose for the first time a differentially-fed dual-band implantable antenna, which can be connected more easily with differential

circuitries, eliminating the loss introduced by baluns and matching circuits. The antenna operates at two center frequencies of 433.9 MHz and 542.4 MHz, which are both near MICS band, to work with a sub-GHz wideband transceiver designed for high-data rate implantable neural recording [76]. The simulated and measured bandwidths are 7.3 % and 7.9 % at the first resonant frequency, 5.4 % and 6.4 % at the second resonant frequency, respectively.

The organization of this chapter is summarized as follows. In Section 3.2, we get into design application, geometrical details of the proposed antenna and mixed mode theory for general applications. Subsequently, in Section 3.3, the operating principle of the proposed dual-band differentially-fed antenna, simulation results of differential return loss in different tissue models and SAR distribution from HFSS are presented. Measurement results inside a tissue-mimicking solution and analysis are given in section 3.4, followed by the link budget characterization of a communication pair with two dual-band antennas in Section 3.5. Co-testing results with the circuits are given in Section 3.6. Finally, the conclusion remarks are summarized in Section 3.7.

3.2 Antenna Design and Mixed-mode Theory

The proposed antenna is to be connected with a dual-band CMOS transmitter operating at 542.4 MHz and 433.92 MHz for neural signal recording [76].

3.2.1 Antenna Design

The proposed antenna is fabricated on the substrate of Rogers 6010 (ε_r = 10.2, $tan\delta$ = 0.0023), covered by a superstrate with the same material, each with a thickness of 25 mil (0.635 mm). The superstrate layer is used to protect the antenna from direct contact with the semi-conducting tissue. Also, the superstrate acts as a buffer between the metal radiator and human tissues by reducing RF power at the locations of lossy human tissues [26]. The total size of the antenna is 27 mm × 14 mm × 1.27 mm (480.06 mm^3). Because the antenna is a differentially-fed one, we proposed a structurally symmetrical antenna where a spiral shaped branch is connected to the main path to create the second resonance. The operating principle concerning the resonance path

would be explained further in Section 3.3.2. The feeding location is on the same side of the antenna for better connection with differential circuitry. The geometry of the proposed antenna is given in Figure 3-1, and we can see from the figure that the antenna is symmetrical with respect to the *x* axis. Therefore, in Figure 3-1, we only label the geometrical dimension for one side. The differential input impedance of the proposed antenna is 100 Ω, meaning an impedance of 50 Ω for each port. The detailed values of geometrical dimension are summarized in Table 3-1.

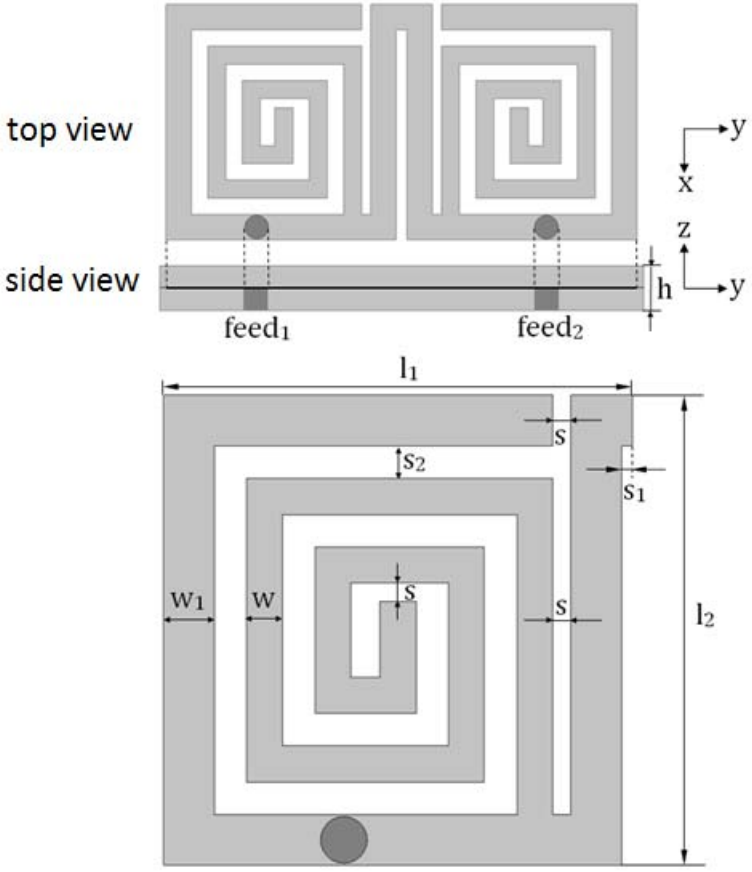

Figure 3-1 Geometry of the proposed dual-band differentially-fed antenna.

Table 3-1 Geometrical dimension of proposed antenna

Symbol	Value (mm)
l_1	13.1
l_2	13.2
s	0.5
s_1	0.3
s_2	0.9
w	1.0
w_1	1.4
h	1.27

3.2.2 Differential Reflection Coefficient Characterization

For characterizing the reflection coefficient of a differential antenna, the theory of mix-mode S parameters is commonly employed [77]. Following this work, the input impedance, mixed-mode S-parameters and various measurement techniques of differential systems and antennas have been systematically investigated [78]-[86]. The derivation and some basic theory about mixed-mode S parameters for 1-port differential structure (meaning 2 ports for the conventional structure) are shown below.

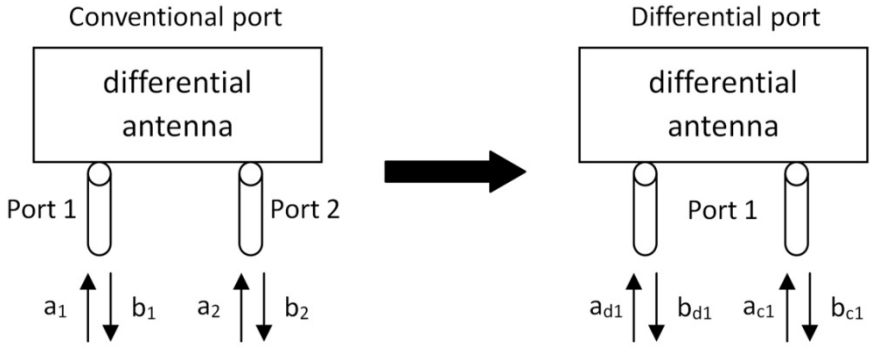

Figure 3-2 Simple schematic for conventional single-ended port to differential port conversion.

The simple schematic for conventional single-ended port to differential port conversion is shown in Figure 3-2. The conventional S-parameters can be expressed as

$$\begin{bmatrix} b_1 \\ b_2 \end{bmatrix} = \begin{bmatrix} S_{11} & S_{12} \\ S_{21} & S_{22} \end{bmatrix} \begin{bmatrix} a_1 \\ a_2 \end{bmatrix} = [S_{std}] \begin{bmatrix} a_1 \\ a_2 \end{bmatrix} \tag{3-1}$$

where a_i and b_i represents the stimulus and response wave of port i, and S_{std} is the standard S-parameters matrix.

In contrast, when port 1 and port 2 are viewed as a single differential port 1, the mixed-mode S-parameters of Figure 3-2 can be expressed as

$$\begin{bmatrix} b_{d1} \\ b_{c1} \end{bmatrix} = \begin{bmatrix} S_{dd11} & S_{dc11} \\ S_{cd11} & S_{cc11} \end{bmatrix} \begin{bmatrix} a_{d1} \\ a_{c1} \end{bmatrix} = \begin{bmatrix} S_{mm} \end{bmatrix} \begin{bmatrix} a_{d1} \\ a_{c1} \end{bmatrix} \tag{3-2}$$

where a_{d1} and a_{c1} are the differential mode and common mode stimulus wave, and b_{d1} and b_{c1} are the differential mode and common mode response wave. And S_{mm} represents the mix-mode S-parameters matrix. S_{dd11} is the differential-mode S-parameter, S_{cc11} is the common-mode S-parameter, S_{dc11} and S_{cd11} is the mode-conversion or cross-mode S-parameter.

From [77], [78], we know that

$$\begin{bmatrix} a_{d1} \\ a_{c1} \end{bmatrix} = \frac{1}{\sqrt{2}} \begin{bmatrix} 1 & -1 \\ 1 & 1 \end{bmatrix} \begin{bmatrix} a_1 \\ a_2 \end{bmatrix} = M \begin{bmatrix} a_1 \\ a_2 \end{bmatrix} \tag{3-3}$$

$$\begin{bmatrix} b_{d1} \\ b_{c1} \end{bmatrix} = \frac{1}{\sqrt{2}} \begin{bmatrix} 1 & -1 \\ 1 & 1 \end{bmatrix} \begin{bmatrix} b_1 \\ b_2 \end{bmatrix} = M \begin{bmatrix} b_1 \\ b_2 \end{bmatrix} \tag{3-4}$$

Therefore from equation (3-1), (3-2), (3-3) and (3-4), we can get the following equation

$$S_{mm} = M S_{std} M^{-1} \tag{3-5}$$

$$\left.\begin{aligned} S_{dd11} &= \frac{1}{2}\left(S_{11} - S_{21} - S_{12} + S_{22}\right) \\ S_{dc11} &= \frac{1}{2}\left(S_{11} - S_{21} + S_{12} - S_{22}\right) \\ S_{cd11} &= \frac{1}{2}\left(S_{11} + S_{21} - S_{12} - S_{22}\right) \\ S_{cc11} &= \frac{1}{2}\left(S_{11} + S_{21} + S_{12} + S_{22}\right) \end{aligned}\right\} \tag{3-6}$$

For a symmetric balanced antenna, as in the case of our proposed implantable antenna, $S_{11}=S_{22}$ and $S_{12}=S_{21}$, equation (3-6) can be further reduced to

$$\left.\begin{aligned} S_{dd11} &= S_{11} - S_{12} \\ S_{dc11} &= 0 \\ S_{cd11} &= 0 \\ S_{cc11} &= S_{11} + S_{12} \end{aligned}\right\} \tag{3-7}$$

This means for a symmetrically balanced antenna, there is no conversion between differential mode and common mode.

In our differential feeding case, where the excitations of two ports are equal in amplitude and 180° out of phase, the key parameter of the proposed implantable antenna is the differential reflection coefficient or odd mode reflection coefficient, which is

$$\Gamma_{odd} = S_{11} - S_{12} \tag{3-8}$$

The mixed-mode theory is applicable to general applications, not limited by coupled transmission lines and shielded balanced transmission lines. And the difference between balanced cases and unbalanced cases is that when the structure is not balanced, mode-conversion will exist. For the following section, we will use this parameter Γ_{odd} to evaluate the reflection coefficient of the antenna.

3.3 Simulation Environment, Results and Operating Principle

3.3.1 Simulation Environment

We know that one- and three-tissue-layer models will not cause any big difference for the simulated return loss [26]. As a result, firstly we only set up one layer of tissue for simulation, and then test the robustness of antenna in the three-layer tissue model. The simplified geometry of one-layer tissue is given in Figure 3-3. Due to the fact that the antenna is intended for neural recording applications, we assume that the size of the tissue is 180 mm × 180 mm × 180 mm, the maximum dimension of which is the same as the human head model in [26]. For initial evaluation, a simple cubic tissue box is assumed, with 10 mm thickness of tissue above the antenna and 170 mm thickness of tissue below the antenna. For actual implantation where the

consideration of both the curvature of the human head and different implanting positions is needed, only some tuning of the geometrical parameters of this proposed antenna is necessary.

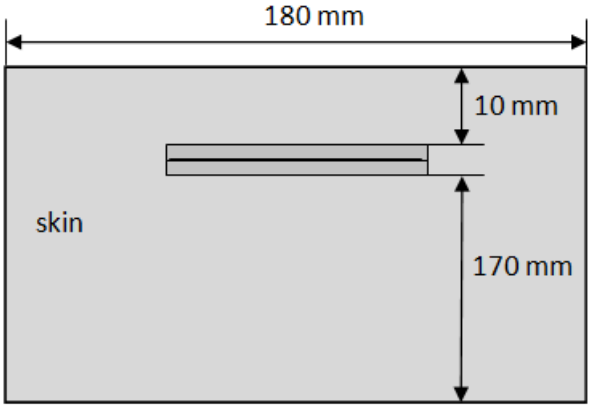

Figure 3-3 Simplified geometries for the one-layer tissue model (not in scale).

The permittivity and conductivity of the tissue for one-layer tissue model are from those of dry skin, and the dielectric properties of tissue vary with frequency. The numerical values of permittivity and conductivity for all tissues used in our models at our operating frequency are listed in Table 3-2 , which can be found in [44]. Because our antenna is operating at two closely spaced frequencies, we take the arithmetic average of two frequencies in which the dielectric properties of simulation model are chosen. For instance, for the dry skin used as the one layer model, a permittivity of 45.2 and a conductivity of 0.72 are assumed.

Table 3-2 Dielectric properties of tissues

biological tissues	**433.9 MHz**		**542.4 MHz**		**arithmetic average**	
	ε_r	σ **(S/m)**	ε_r	σ **(S/m)**	ε_r	σ **(S/m)**
Fat	5.57	0.04	5.53	0.04	5.55	0.04
Muscle	56.9	0.81	56.2	0.83	56.6	0.82
Skin	46.1	0.70	44.3	0.74	45.2	0.72

3.3.2 Operating Principle

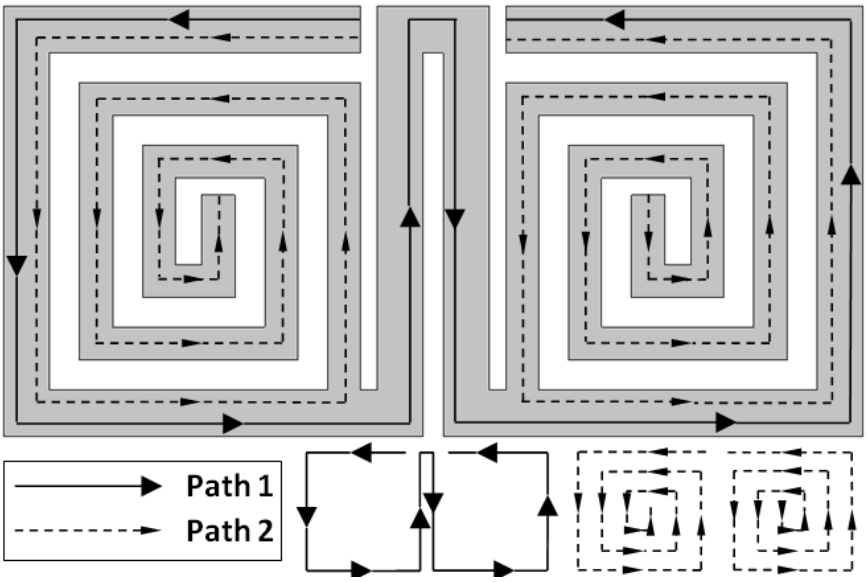

Figure 3-4 Electric current paths of the proposed dual-band differentially-fed antenna.

In order to explain the operating principle of the proposed antenna, a simplified schematic of the antenna is given in Figure 3-4 and two electric current paths are indicated in the figure. Path 1 is with the same conductor track width (w_1). For spiral-shaped Path 2, from the turning point between the third and fourth segments (counting from the outermost to the innermost), the conductor track width changes from w_1 to w, and the spacing between each turn is fixed at s_2. It is observed that the first resonance around 433.9 MHz is controlled by both Paths 1 and 2, while the second resonance around 542.4 MHz is mainly controlled by Path 2.

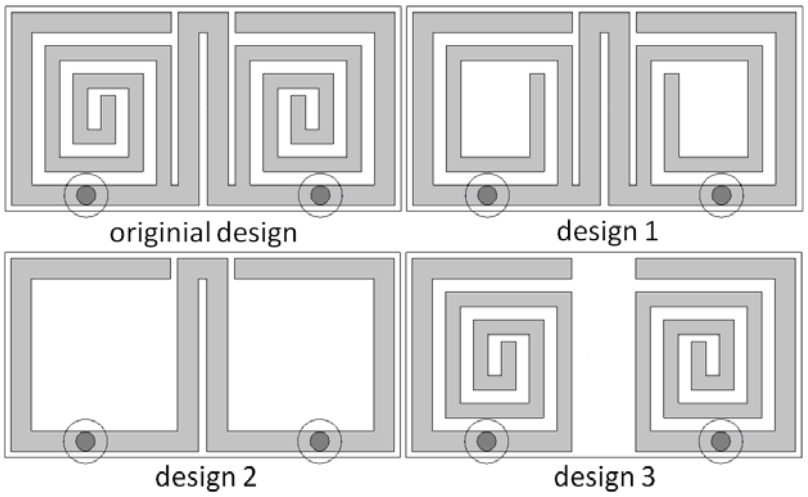

Figure 3-5 Antenna design variations to validate the operating principle.

To validate this point, we modified the antenna based on the original one and get three variations, as in Figure 3-5. At first, we gradually cut the inner segments of the spiral-shaped path and get two antenna designs designated as design 1 and design 2, and then we removed the part for connecting two spirals of the original antenna and designate it as design 3.

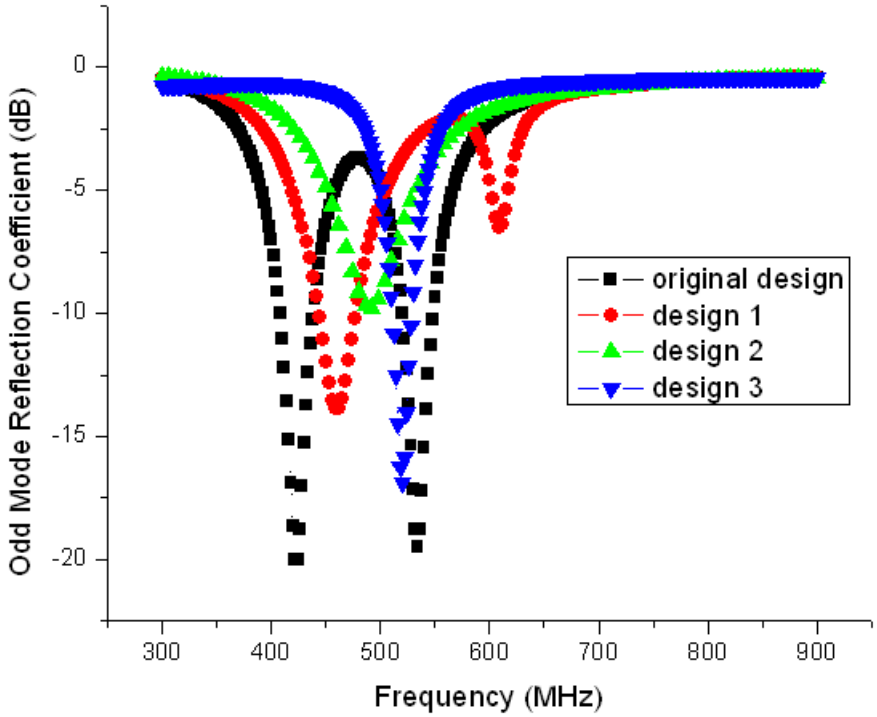

Figure 3-6 Odd mode reflection coefficient comparison of the original design and three modified designs for validating the operating principle.

Then we simulate these structures in FEM based HFSS. To ensure differential feeding, we should edit the source for two ports in HFSS to be 180° out of phase and keep the power magnitude of two ports to be equal. Then the odd mode reflection coefficients of these three modified designs are compared with the original antenna in Figure 3-6.

From Figure 3-6, we can observe that as the spiral segments are removed gradually, the second resonant frequency shifts up and differential S_{11} becomes worse, meanwhile the first frequency also shifts up a little. When the spiral part is completely removed as in the case of design 2, the second resonance disappears and the first resonance remains with certain frequency shift and reduction of the reflection coefficient. For further verification we removed the part for connecting two spirals of the original antenna and

designate it as design 3. From the comparison in Figure 3-6, we can see that the second resonance is almost unaltered while the first resonance disappears, which means that the second resonance is mainly controlled by the spiral part.

Then in order to investigate the influence of tissue thickness on the antenna, we changed the thickness of tissue and compared the simulation results of the differential S_{11}, and we found that neither the thickness of tissue above nor below the antenna has any effect on the odd mode reflection coefficient. Also, from our simulation, we found that the size of tissue does not affect the reflection coefficient as well.

3.3.3 Three-layer Tissue

The thickness of each layer for the three-layer tissue model is from [26]. For the three-layer tissue model, we also evaluate the effect of antenna position in different tissue layers on the simulation results of the differential S_{11}.

(a)

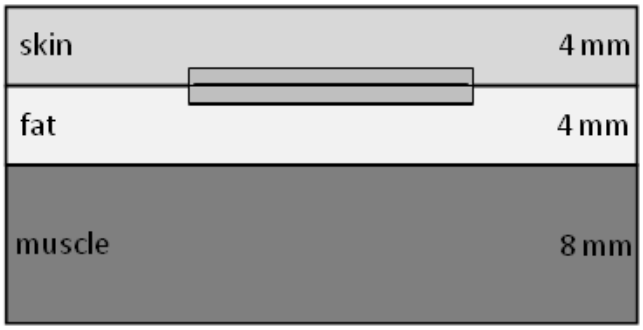

(b)

(c)

(d)

Figure 3-7 Simplified geometries for the three-layer tissue models, with antenna implanted (a) in the middle of skin layer (b) between skin and fat layer (c) in the middle of fat layer (d) in the middle of muscle layer.

The simplified geometries for the three-layer model with different implant positions are as shown in Figure 3-7, the size of tissue in the *x-y* plane is the same as that for the one-layer tissue model. Then we do the simulation in HFSS and compare the odd mode reflection coefficient in Figure 3-8.

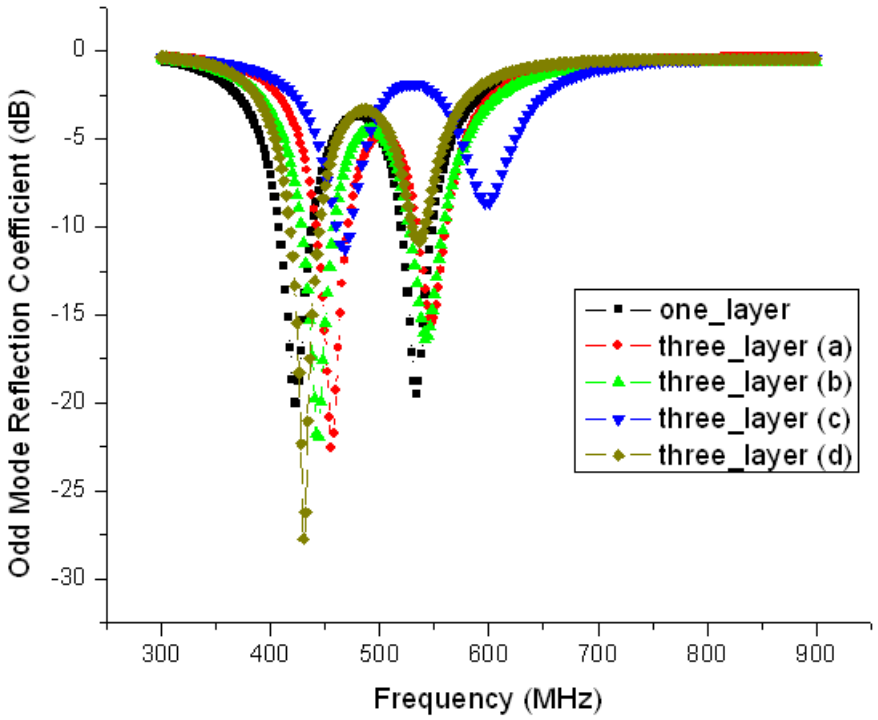

Figure 3-8 Comparison of odd mode reflection coefficient in different tissue models and in various positions.

From this figure, we can see that the odd mode reflection coefficient of the antenna does not change much when the simulation environment varies. However, there is some frequency shift and certain off-resonance. For instance, when the simulation environment is changed from one-layer skin tissue model to the three-layer model of Figure 3-7 (a), the first resonant frequency shifts 34 MHz higher and the second resonant frequency shifts 14 MHz higher. Additionally, when the antenna is implanted in the fat layer as shown in Figure 3-7 (c), some off-resonance can be observed, and the minimum value of differential $|S_{11}|$ of two resonant frequencies changes to -11.3 dB and -8.7 dB, respectively. Also for the implantation as shown in Figure 3-7 (c), the first resonant frequency shifts 11 MHz higher and the second one shifts 49 MHz higher when compared with Figure 3-7 (a). For the implantation in muscle layer as shown in Figure 3-7 (d), the second resonance is relatively weak, and the differential $|S_{11}|$ becomes worse to -10.7 dB. These are caused by the fact that the permittivity and conductivity of fat are much lower than those of skin and muscle, while the dielectric properties of skin and muscle are relatively close to each other at our operating frequency. Therefore for implantation in

different tissue layers, the antenna's geometrical parameters should be tuned accordingly to achieve a better reflection coefficient.

3.3.4 SAR Distribution

For safety concerns caused by the implanted device on the human body, we should evaluate SAR, a measure of power absorbed by the tissue. The standards of SAR are regulated by IEEE. For C95.1-2005 standard, the 10-g averaged SAR should not exceed 2 W/kg [47]. From [76], we know that the maximum output power for the transmitter chip is -19 dBm, meaning 6.29 μW for each port. After editing the input power and offset phase of two ports and simulate the structure in HFSS, we find the SAR for two resonant frequencies to be 9.30×10^{-4} W/kg and 9.36×10^{-4} W/kg respectively at the y-z plane, which is well below the maximum limit. Also, assuming a SAR of 2 W/kg, we can get that the maximum input power for each port of this differential antenna is 13.5 mW. The SAR value for the x-z plane is also evaluated, and the maximum SAR values in *y-z* plane and *x-z* plane at two resonant frequencies and the allowed maximum input power for this antenna in one-layer tissue are summarized in Table 3-3.

Table 3-3 Maximum SAR values and maximum allowed input power

Maximum SAR Values	***y-z* plane**		***x-z* plane**		**Maximum allowed input power (mW)**
	423 MHz	532 MHz	423 MHz	532 MHz	
C95.1-2005, 10-g averaged SAR (mW/kg)	0.930	0.936	0.895	0.933	13.5

In addition, the 1-g averaged SAR distributions of two resonant frequencies at the *y-z* plane are given in Figure 3-9. For 1-g averaged SAR, the maximum is 2.44×10^{-3} W/kg and 2.66×10^{-3} W/kg for two resonant frequencies. From the SAR distribution shown in Figure 3-9 (a), we can see that maximum SAR is distributed around the central region, with some small influence from two spiral shapes, and from Figure 3-9 (b), we can clearly see that two

maximum SAR field areas which are situated above two spiral-shaped region at each side of the symmetrical structure. Therefore from this 1-g averaged SAR distribution, we can further validate the operating principle about the proposed dual-band antenna elaborated in Section 3.3.

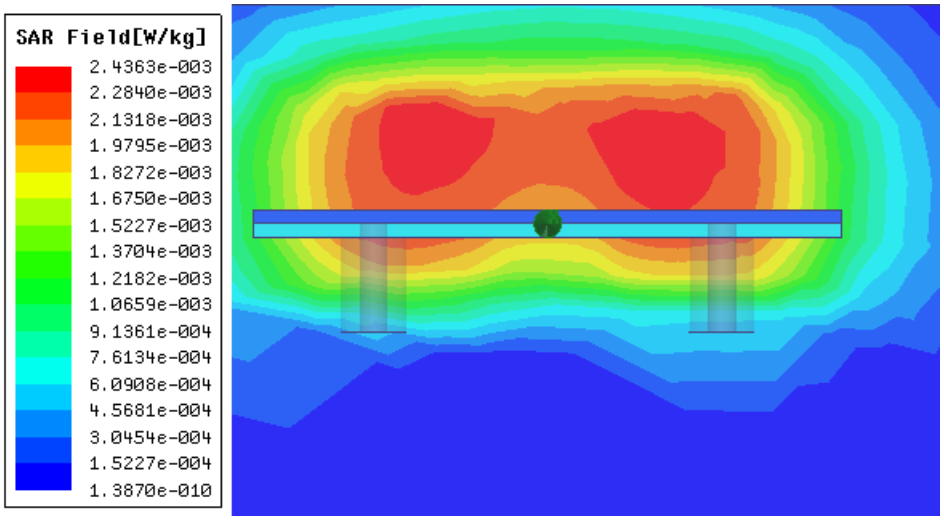

(a)

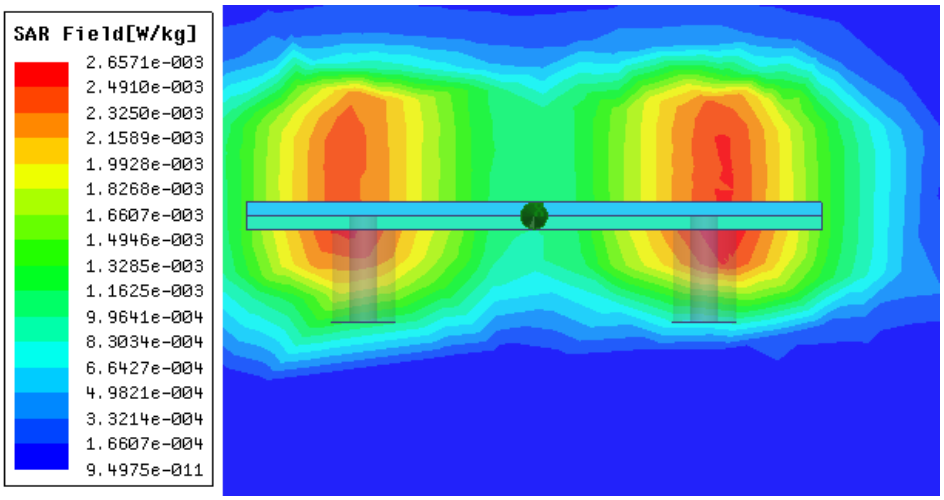

(b)

Figure 3-9 SAR distribution of proposed antenna at the operating frequency of (a) 423 MHz, *y-z* plane (b) 532 MHz, *y-z* plane (input power for each port: 6.29 μW).

3.4 Measurement Results

The measurement environment surrounding the antenna is a tissue-mimicking solution filled in a plastic box, and the solution we adopted is some skin-mimicking gel, the recipe of which was proposed by [9]. For MICS band,

the recipe is 56.18 % sugar, 2.33 % salt and 41.49 % deionised water. The fabricated antenna is shown in Figure 3-10.

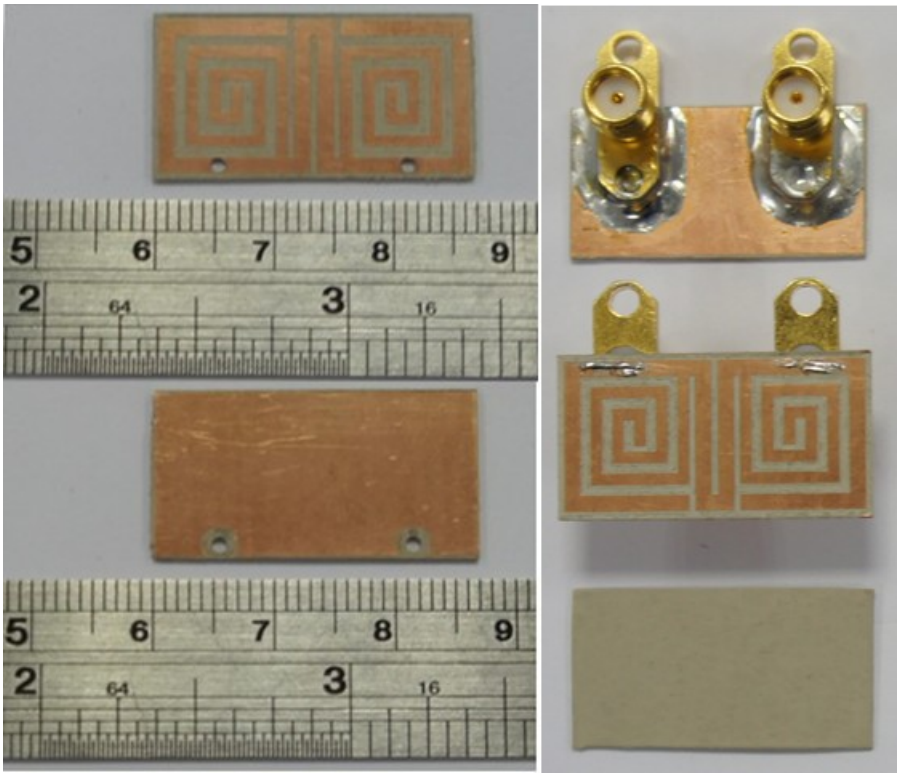

Figure 3-10 Top and bottom views of the fabricated implantable antenna.

For the measurement of differential antennas, although traditional two-port VNA may suffice, a real-time display of the differential reflection coefficient in the network analyzer cannot be guaranteed. Consequently, a four-port network analyzer with direct mix-mode measurement capability would be preferable. As a result, Agilent N5222A four-port PNA Microwave Network Analyzer was used to do the measurement, the setup of which is shown in Figure 3-11. The comparison of simulation and measurement results in air and liquid tissue is given in Figure 3-12.

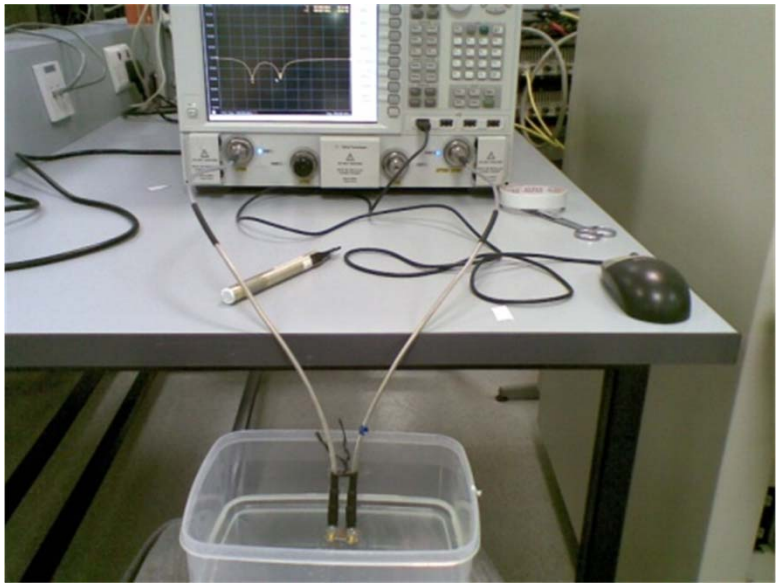

Figure 3-11 Measurement setup for the implanted antenna.

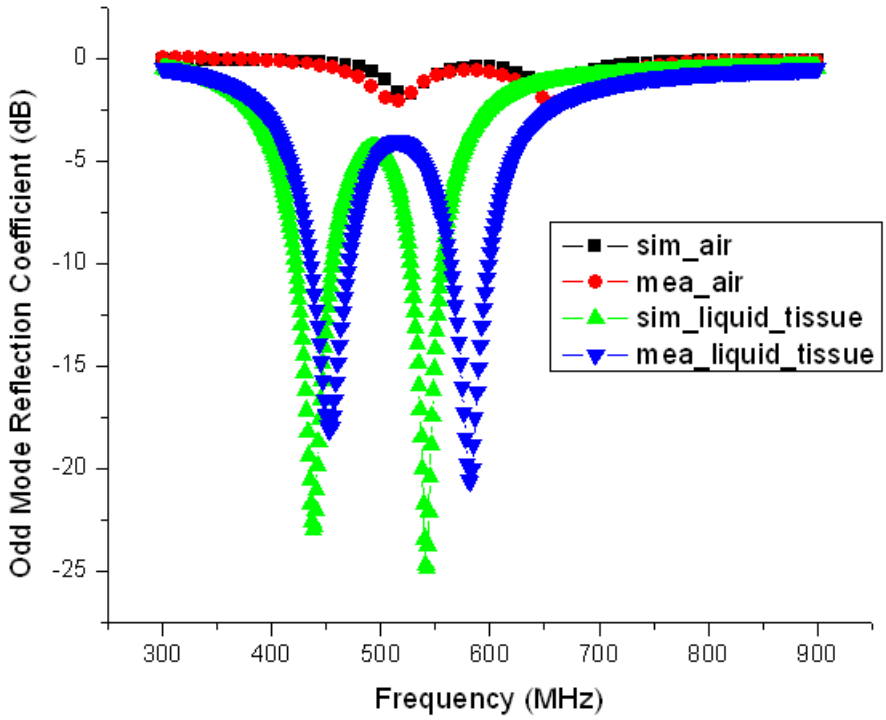

Figure 3-12 Simulation and measurement results comparison of odd mode reflection coefficient for the proposed antenna in air and in liquid tissue.

From Figure 3-12, it can be seen that we can view the tissue as a superstrate with a high dielectric constant and high loss tangent, having the effect of decreasing the resonant frequency, widening the bandwidth and reducing the gain. The simulated and measured results are quite close, with a frequency shift of around 14 MHz and 36 MHz for two resonant frequencies in the liquid tissue. The simulated and measured frequency bands (differential

$|S_{11}|$ < -10dB) in tissue for the first resonant frequency are 408 MHz ~ 439 MHz (7.3 % bandwidth) and 435 MHz ~ 471 MHz (7.9 % bandwidth), respectively. For the second resonant frequency, they are 520 MHz ~ 549 MHz (5.4 % bandwidth) and 563 MHz ~ 600 MHz (6.4 % bandwidth), respectively.

3.5 Communication Link

Because the implanted transmitting antenna is a dual-band one, we also adopted a dual-band configuration for the external antenna, the geometry of which is the same as proposed in [87]. The detailed geometrical parameters of the external antenna are given in Figure 3-13, and the antenna is symmetrical with respect to both the *x* axis and *y* axis. The antenna is a typical dipole with two U-shaped slots of the same width along the slot path in each arm to create another resonance. The antenna is supported by the commonly used FR4 substrate, and the differential input impedance for this dipole is 100 Ω, the same as that for the implanted antenna. However, the difference is that for the implanted antenna, there are two separate feeding ports; for the external dipole antenna, there is only one feeding port which is located at the center.

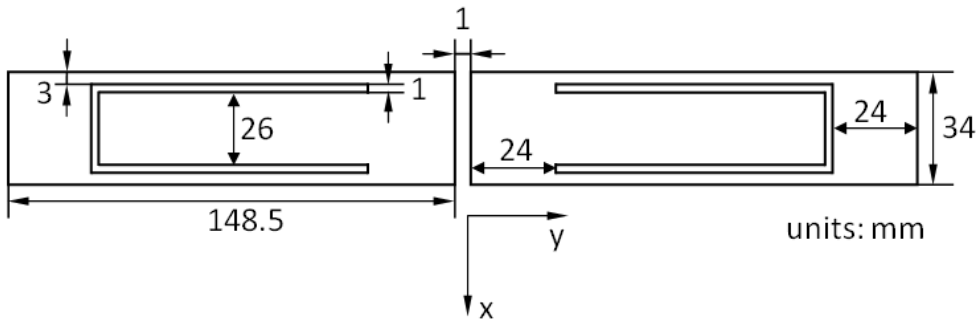

Figure 3-13 Geometry of the external antenna.

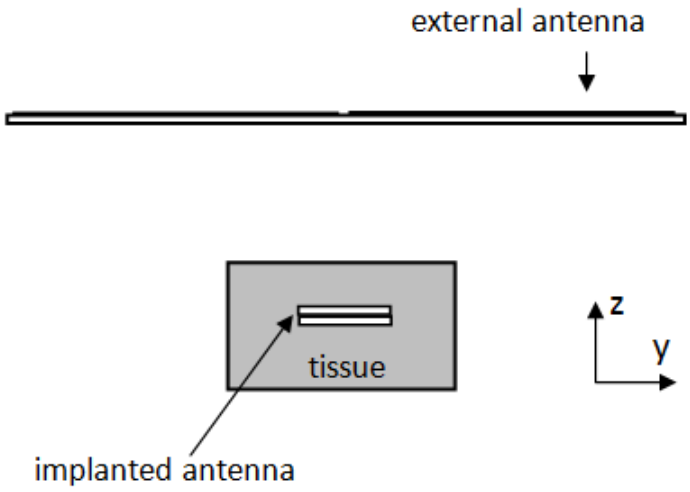

(a)

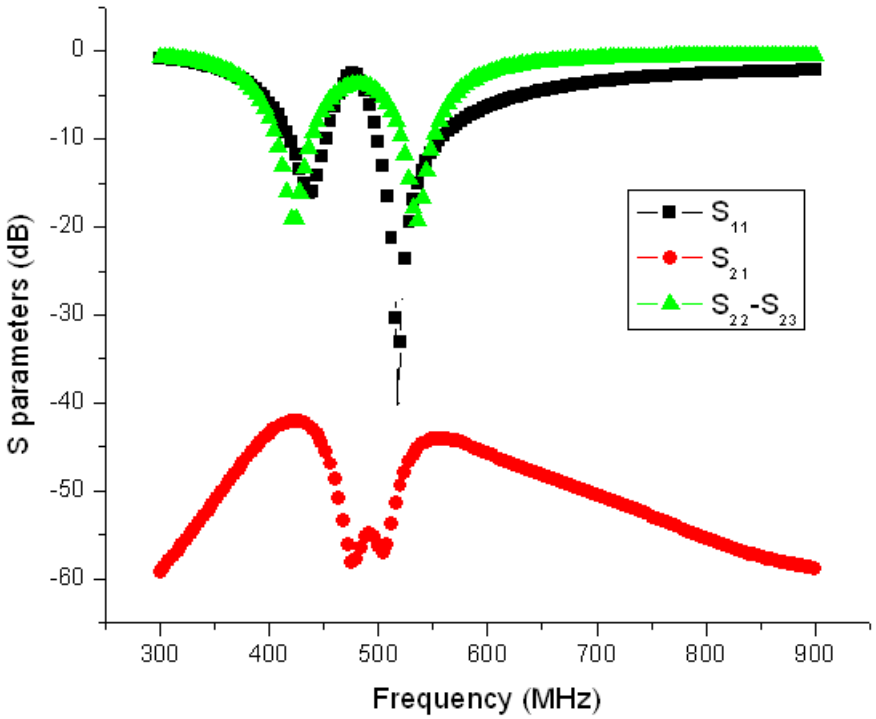

(b)

Figure 3-14 (a) Simulation setup for characterizing the communication link (length of antenna is not in scale). (b) S parameters of the antenna pair.

For the characterization of the communication link, we assume a one-layer tissue model for the implanted antenna and space two antennas at 130 mm apart and evaluate the coupling between them. The simulation setup is given in Figure 3-14 (a), and the simulated S parameters of two antennas are given in Figure 3-14 (b). We assume the differential port of the external antenna as port 1 and two bottom-feeding ports of the internal implanted antenna as port

2 and port 3. Because port 2 and port 3 are symmetric, we can take either S_{21} or S_{31} as the coupling strength between two antennas. Therefore, S_{11} is the reflection coefficient of the external antenna, and S_{22}-S_{23} (Γ_{odd}) is the odd mode reflection coefficient of the implanted antenna. From Figure 3-14 (b) we can see that we achieved a maximum coupling strength of -42.4 dB and -44.6 dB at 433.92 MHz and 542.4 MHz.

The near field boundary is $\lambda/2\pi$ = 88~110 mm (λ = 553~691 mm, the operating frequency 433.92 MHz, 542.4 MHz). For our application, we assume the distance between transmitting and receiving antennas is 130 mm, the same distance as in [7]. Therefore, we would say the system is working in the intermediate region, and close to the near field condition. Additionally, we found that the size of tissue will affect the radiation direction and maximum gain significantly. Due to all these reasons, the far-field radiation pattern may not be able to provide some useful information. Therefore as long as we set up an external receiving antenna and get a satisfactory coupling and reasonable link margin between the implanted antenna and the external one, the proposed antenna would serve as a perfect candidate of data transmission for neural recording applications.

When two antennas are perfected matched, the S-parameter $|S_{21}|$ quantifies the power transmission, and therefore it also gives the value of path loss.

$$\left|\mathrm{S}_{21}\right|^2 = P_R / P_T \tag{3-9}$$

where P_R is the received power and P_T is the transmitted power. When expressed in decibel, $|S_{21}|$ should be the same value of P_R/P_T and the negative value of path loss. Now we summarized the various parameters of the link budget in Table 3-4.

Table 3-4 Parameters of the link budget

Operating frequency	433.9 MHz	542.4 MHz
Tx power	-19 dBm	
Distance	130 mm	
Path loss	42.4 dB	44.6 dB
Implementation loss	6 dB	
Receiver noise floor	-101 dBm	
SNR (BER=1E-5)	14 dB	

The link margin (LM) can be expressed as

$$\begin{aligned} \mathrm{LM} &= P_T - PL - RNF - IL - SNR \\ &= -19\,dBm - 44.6\,dB + 101\,dBm - 6\,dB - 14\,dB \\ &= 17.4\,dB \end{aligned} \tag{3-10}$$

where *PL* is path loss and *RNF* is receiver noise floor and *IL* is implementation loss and *SNR* is the signal to noise ratio of the receiver. For the value of PL in the calculation of link margin, we take the larger one for the path loss at two resonant frequencies. The distance between two antennas is the same as that in [7]. And the values of receiver noise floor and *SNR* are from [41]. If the receiver BER (Bit Error Rate) is not as stringent as 1×10^{-5}, the link margin may be improved further.

Additionally, we gradually increased the distance along the *z* axis between two antennas from 100 mm to 500 mm and evaluate the coupling strength with distance. The simulation results of $|S_{21}|$ and the resulting link margin at two resonant frequencies are given in Figure 3-15. After the distance along the *z* axis between two antennas is increased from 100 mm to 500 mm, a decrease of 14.2 dB for link margin can be seen, and even at a large distance of 500 mm between two antennas, a minimum link margin of 6.3 dB can be obtained.

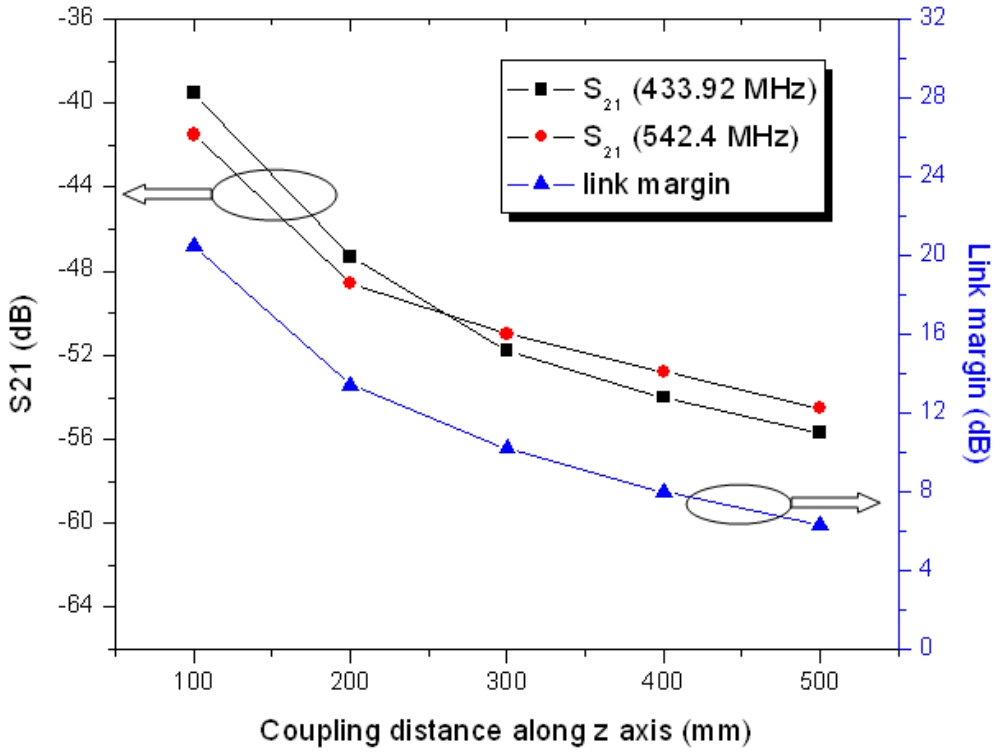

Figure 3-15 Variation of $|S_{21}|$ and link margin with respect to the distance between two antennas.

3.6 Co-testing with the Circuits in Minced Pork

After evaluation of the communication link, we do the co-testing with the circuits of the communication link in minced pork. The system overview of the co-testing platform is shown in Figure 3-16, and Figure 3-17 shows the communication link overview.

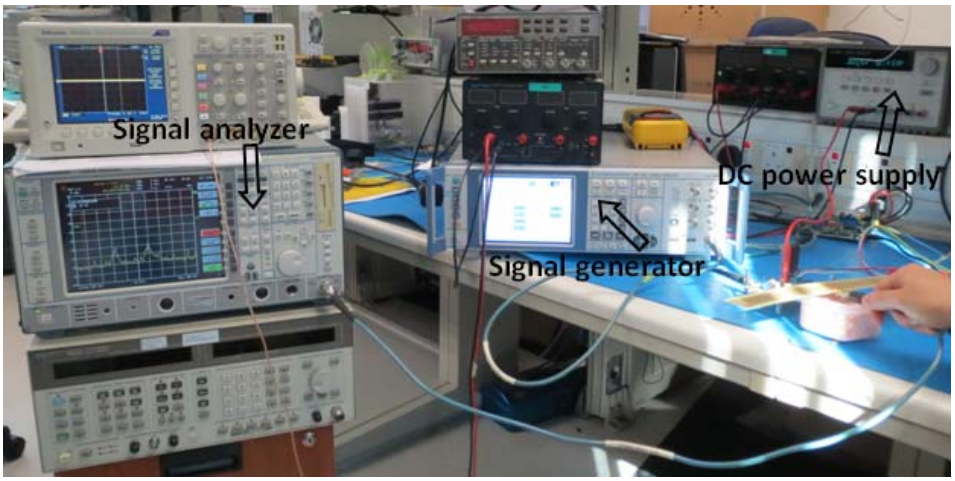

Figure 3-16 System overview of the co-testing platform.

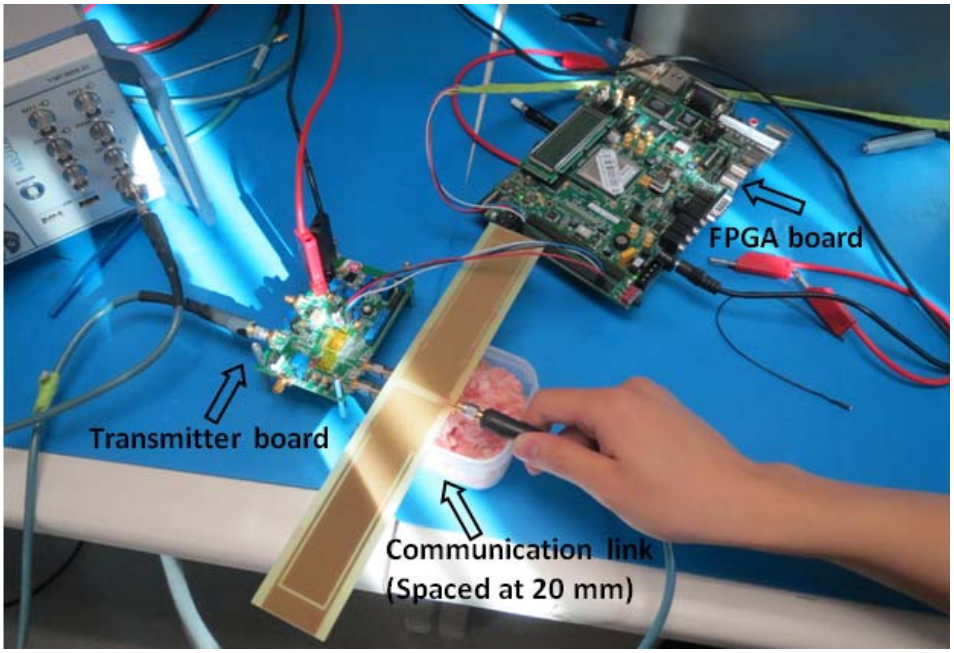

Figure 3-17 Communication link overview.

The signal generator generates the clock of the transmitter, which is 13.56 MHz. The FPGA board generates the data for transmission. Two frequencies of transmitter output are 433.92 MHz and 542.4 MHz. To have a better understanding of the communication link, we give the block diagram of the proposed burst-mode injection-locked FSK transmitter in Figure 3-18 [32].

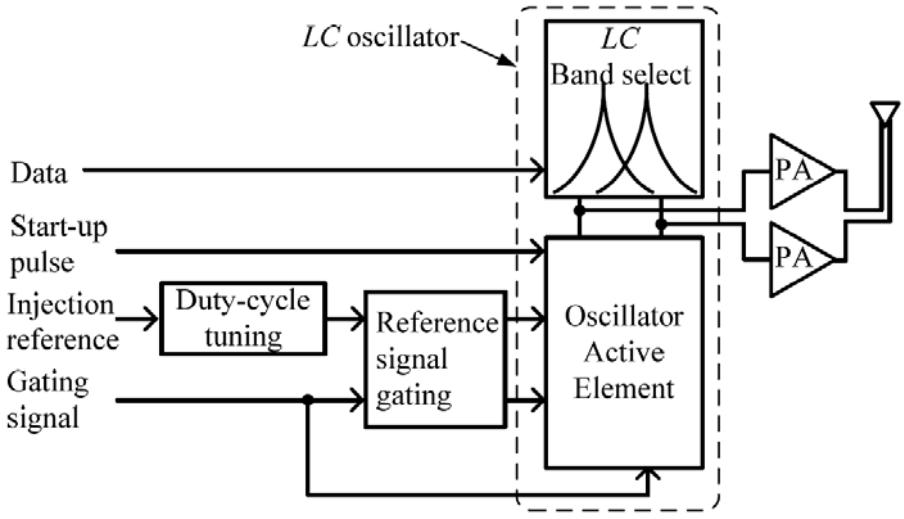

Figure 3-18 Block diagram of the proposed burst-mode injection-locked FSK transmitter [32].

The transmitter is directly connected with the differential dual-band implantable antenna embedded in minced pork, eliminating the usage of baluns and matching circuits. The external half-wavelength dual-band dipole,

which is spaced 20 mm apart from the implanted antenna, is connected with the signal analyzer.

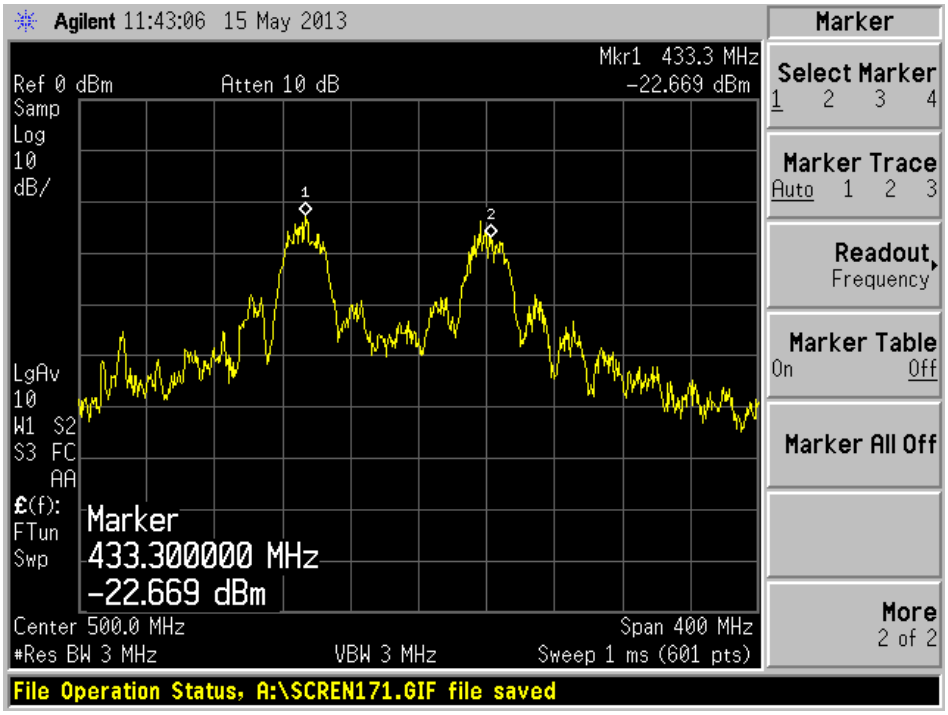

Figure 3-19 Screen snapshot of output power of the transmitter.

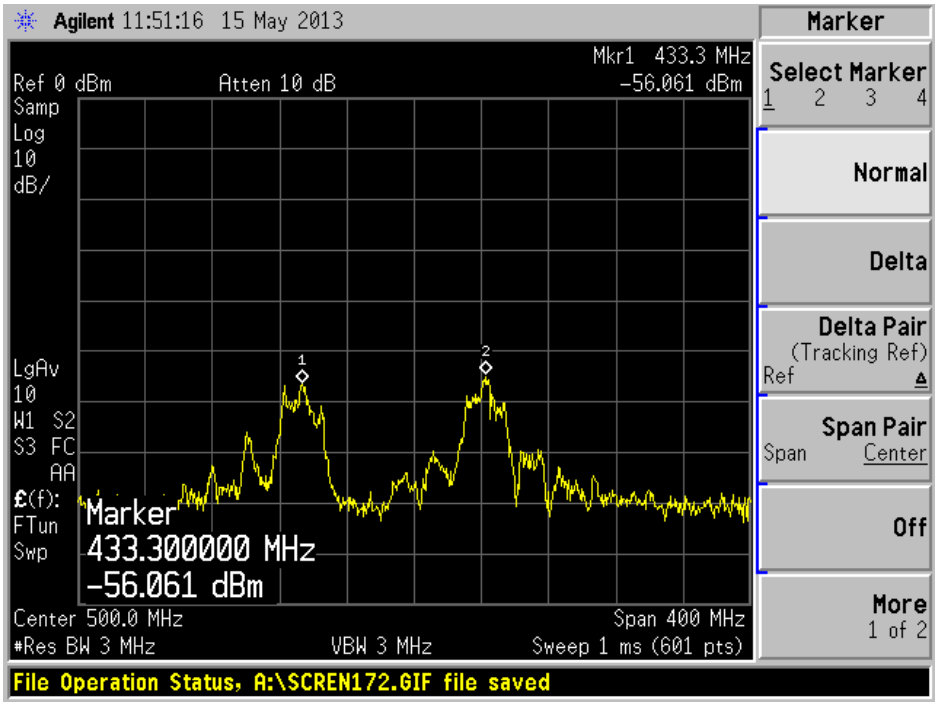

Figure 3-20 Screen snapshot of received power by the external dipole.

Figure 3-19 shows screen snapshot of output power of the transmitter, which is around -22.6 dB. Figure 3-20 shows the screen snapshot of received power by the external dipole, which is around -56.0 dB.

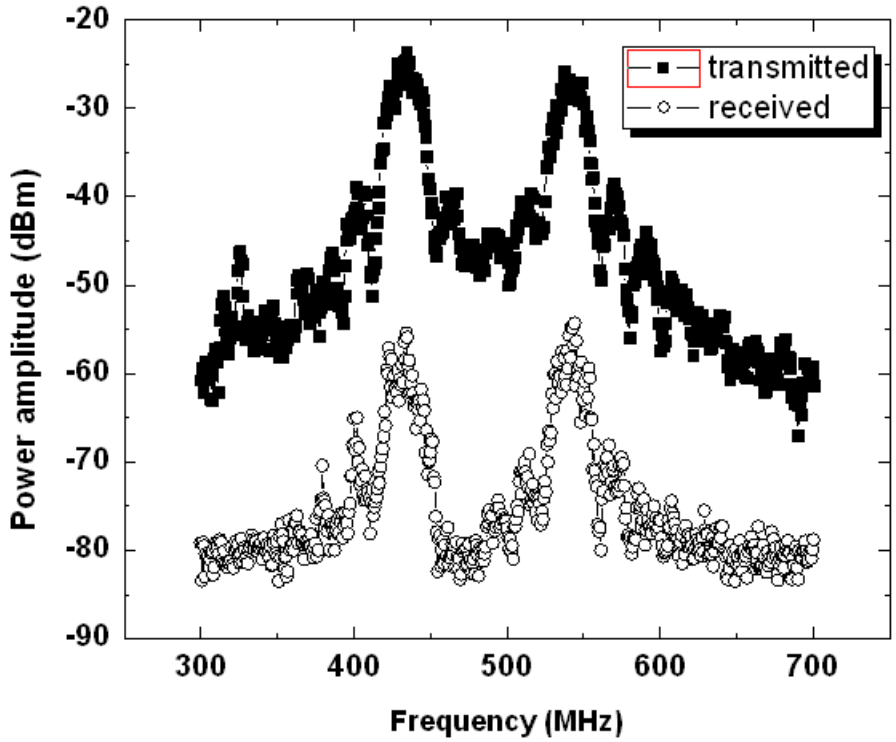

Figure 3-21 Data plot of the transmitted power and received power.

Figure 3-21 shows data plot of the transmitted power and received power. The transmitter output power is around -23 dBm, the received power by the external dipole is around -56 dBm. Therefore the path loss is around 33 dB, and the theoretic result from HFSS simulation of the coupling strength is around -29 dB at a coupling distance of 20 mm, which is close to the measurement result.

3.7 Conclusion

We have proposed an implantable antenna which achieves both differential feeding and dual-band operation for biomedical applications for the first time. The operating theory of the proposed antenna is presented, and the robustness of the antenna in different tissue models and different simulation environment is evaluated. Additionally, SAR distribution is presented, and the simulation and measurement results of the odd mode reflection coefficient are compared.

Finally, a communication link with dual-band configuration for both the external and internal antennas is characterized, and experimental results with the transmitter circuits are presented

The differential configuration of the antenna can facilitate its easy connection with differential circuits, eliminating the additional loss introduced by baluns and matching circuits. Also, two operating frequencies of the proposed antenna are quite close, therefore for single band application we can also tune the geometrical parameters of this antenna to achieve bandwidth enhancement. The proposed antenna is compact, easy to be fabricated and of low cost, which can be used in modern wireless data communication link for biomedical implantable systems.

Chapter 4

A Differentially Fed Dual Band Implantable Antenna Operating at MICS Band and ISM Band

4.1 Introduction

Implantable devices have been utilized to improve patient's quality of life for a long time [88]. For the operating frequency of implanted antennas for data transfer, MICS band is most commonly used [26]-[35]. MICS band is allocated to biotelemetry applications according to Recommendation ITU-R SA.1346, and later superseded by RS. 1346 [41]. However, the frequency band 401-406 MHz is previously allocated to the Meteorological Aids Service, in order to reduce the harmful interference that might occur to the operation of Meteorological Aids, a maximum limit of -16 dBm on the EIRP of MICS is specified. Also, 2.4 GHz ISM band is adopted for some cavity slot antennas [37], [38] and a slot dipole antenna [39], and a 3.5-4.5 GHz wideband implanted antenna is proposed for UWB implanted device [40]. Most recently, dual-band and triple-band antennas operating at both MICS and ISM bands emerged [9], [75], [89]. In addition to the planar antennas, capsule antennas used in biotelemetry systems have also been proposed [36], [90]-[91].

We proposed a differentially fed dual-band implantable antenna operating near MICS band for neural signal recording applications in the last chapter. However, the resonant frequencies are both around MICS band, and its bandwidths are narrow. In addition, biocompatible material is not considered and its conformal application in capsule is not evaluated.

In this chapter, we propose a differentially fed dual-band implantable antenna operating at both MICS and ISM bands. An antenna with dual band capability at MICS and ISM bands can be used in a system with two modes, sleep mode and wake-up mode. When data transmission is needed in MICS band, a wake-up signal at ISM band can be sent to the implanted device to wake up the implanted system. When in normal condition, the implant will be in sleep mode. In this way, the total energy consumption is reduced and the lifetime for the implant is extended [92]. Additionally, an antenna with differential configuration can be directly connected to a transmitter with differential outputs, eliminating the loss introduced by baluns and matching circuits.

In the design of implantable antennas, several issues have to be paid attention to:

a) Size restriction. As the antenna is supposed to be implanted in a human body, the size has to be minimized. Depending on different applications, the size varies considerably. Stacked structures can be adopted to reduce the surface area. However, it will result in larger thickness and therefore the reduction of overall volume cannot be guaranteed. Therefore, for the antenna design in this chapter, only one layer of substrate is used.

b) Bandwidth requirement. Implantable environment changes significantly from person to person, therefore the antenna should have a large bandwidth to withstand the frequency shift when implanted in tissues with different dielectric properties. The multi-resonance method has been explored to widen the bandwidth of the implanted antennas [29], [93].

c) SAR evaluation. Due to the fact that the propagation of electromagnetic field will cause the rise of temperature in the human tissue, SAR is commonly used to evaluate the heating issues.

d) Biocompatibility. For real implantation cases, the whole implanted device should be covered by biocompatible material, which is a synthetic or natural material used to replace part of a living system or to function in intimate contact with living tissue. This encapsulation layer not only protects

the antenna from the conducting effect of human tissue, but also reduces the coupling of the antenna's high near field terms of the electromagnetic radiation with the surrounding human tissue [94]. Also the effect of the biocompatible encapsulation layer on the impedance matching and gain of the antenna is significant. Therefore we should take it into consideration when designing implantable antennas.

e) Radiation and coupling. For the implanted antenna, usually the gain is quite low. For instance, the gain usually ranges from -46 dBi to -24 dBi for MICS band operation depending on the size of the antenna [95]. The low gain is mostly contributed by the high conductive loss of the human tissue. Therefore in order to ensure robust communication between the implanted antenna and external receiving unit, link performance should be evaluated.

This chapter is organized as follows: Section 4.2 describes the simulation environment and planar antenna design and its flexible application specifics. Also, the simulation results of differential reflection coefficient in different tissue models from both HFSS and CST human model are presented. In Section 4.3, SAR distribution and radiation properties are given, and the link performance evaluation is also presented. Measurement results inside minced pork environment are given in section 4.4, followed by conclusion remarks in Section 4.5.

4.2 Planar Antenna Design

4.2.1 Simulation Environment

Various simulation environments have been proposed in the past research papers, three-layer tissue including skin, fat and tissue [26], skin mimicking tissue [9], and muscle equivalent tissue [91]. The shape of the body phantom is either a cubic box or a cylinder. Also, from past experience, the shape and size of the body tissue only present a negligible influence on the impedance matching of the implanted antenna, as long as the dielectric properties of the tissue remains the same [25], [91]. We set up a frequency dependent skin tissue model with a size of 100 mm × 100 mm × 100 mm, and the antenna is located 3 mm below the surface of the skin. For comparison, we list the

permittivity and conductivity of the skin, fat and muscle at 403 MHz and 2.45 GHz in Table 4-1, the data of which can be obtained from [44]. From Table 4-1 we can see that although the antenna is designed in skin tissue, it can be implanted in the muscle layer due to its close dielectric properties to skin. However when the antenna is supposed to be implanted in the fat layer, we should re-optimize the geometrical parameters [25].

Table 4-1 Dielectric properties of tissues at MICS and ISM band

Biological tissue	**403 MHz**		**2.45 GHz**	
	ε_r	**σ (S/m)**	**ε_r**	**σ (S/m)**
Skin	46.7	0.69	38.0	1.46
Muscle	57.1	0.80	52.7	1.74
Fat	5.58	0.04	5.28	0.10

4.2.2 Planar Antenna Design and Simulation Results

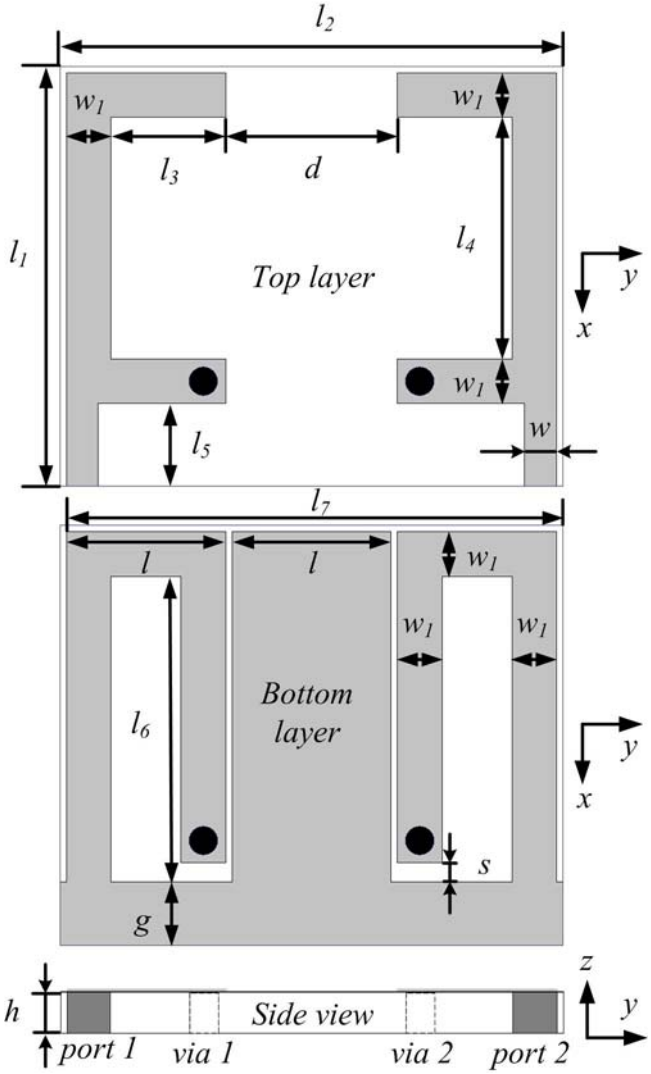

Figure 4-1 The geometry of the proposed planar antenna.

Figure 4-1 shows the geometry of the proposed antenna, which is symmetrical with respect to the *x* axis. And the geometrical parameters of the antenna are listed in Table 4-2. The substrate supporting the antenna is Rogers 3010 (ε_r = 10.2, $tan\delta$ = 0.0035), the thickness of which is 25 mil (0.635 mm). The via holes with a diameter of 0.9 mm are located in the center of the copper trace. The whole antenna is wrapped by a biocompatible material named parylene-C with a thickness of 0.1 mm (ε_r = 2.95, $tan\delta$ = 0.013). The total size of the antenna including the biocompatible encapsulation is 13.4 mm × 16 mm × 0.835 mm (179.0 mm^3). Larger thickness for encapsulation reduces the total power attenuation which is brought by both the encapsulation and the body tissue [94]. However, it increases the size of the whole antenna. Therefore a

compromise has to be made when the antenna is considered being integrated with the whole implanted device.

Table 4-2 Geometrical dimension of proposed planar antenna

Symbol	Value (mm)	Symbol	Value (mm)
w_1	1.4	l_5	2.6
w	1	l_6	9.6
l	5	l_7	15.4
l_1	13.2	g	2.0
l_2	15.8	s	0.6
l_3	3.6	d	5.4
l_4	7.6	h	0.635

For comparison, we used several different settings in simulation. For HFSS simulation, we firstly use two lumped ports, as shown in Figure 4-1. However, concerning that the size of SMA connectors would be comparable to the antenna and the ground size is very small, we also modeled some coaxial cable along the feeding line to investigate the effect of SMA connectors and cables on the performance of the antenna. In this case, two wave ports are applied to two coaxial feeds. Also, for further validation, we placed our antenna in the human model of CST Microwave Studio. In CST, we used two discrete ports to feed the antenna. The simplified simulation setup for HFSS and CST one layer model is shown in Figure 4-2 (a).

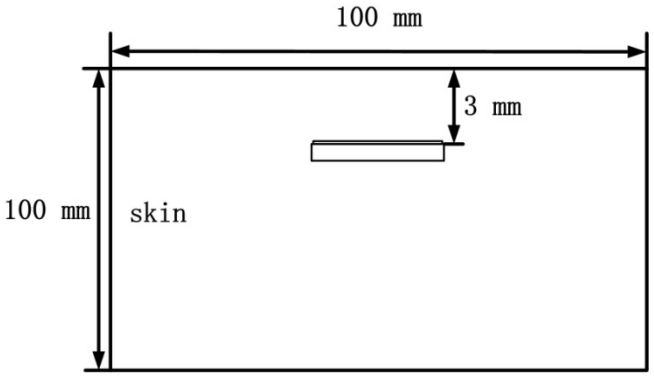

(a)

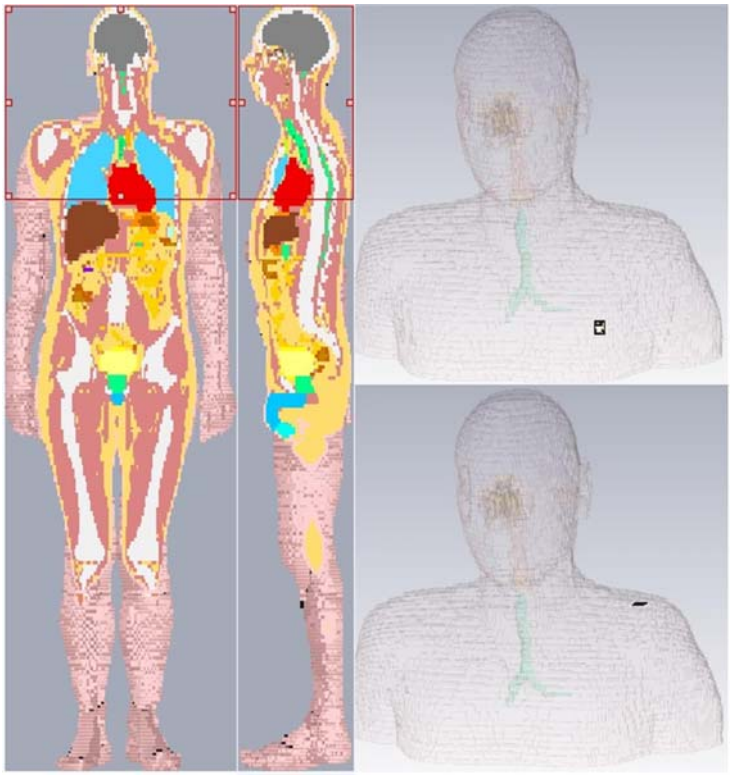

(b)

Figure 4-2 (a) Simulation setup in HFSS and CST for one skin layer model (not in scale). (b) Simulation setup in CST for chest and shoulder implantation.

For the simulation setup in the human model of CST, a male model Gustav is used. Also for reducing the simulation time, we only import the upper part of the human torso including the head. The front and side view of the human model are shown in Figure 4-2 (b). For evaluation of the performance of the implantable antenna, we place it in two different locations: the shoulder and the chest as shown in Figure 4-2 (b). The total volume for the Gustav human body is (0, 0, 0) – (256, 127, 882), and the selected part is (0, 0, 0) – (256, 127, 224). The resolution of the human voxel data is 2.08 × 2.08 × 2 mm^3, which means a total human size of 532.48 × 264.16 × 1764 mm^3.

For the evaluation of differential antennas, mixed mode S-parameters should be employed [77]. A conventional two port system can be reduced to a single differential port as shown in Figure 3-2 in previous chapter. The odd mode reflection coefficient (or differential reflection coefficient) for symmetrical structures can be expressed by the following equation [77], [85]:

$$S_{dd11} = S_{11} - S_{12} \tag{4-1}$$

For the case where the environment for port 1 and port 2 is not exactly symmetrical, for instance when the antenna is implanted in the actual human body of CST rather than a single tissue layer, the differential reflection coefficient should be expressed by the following equation:

$$S_{dd11} = \frac{1}{2}\left(S_{11} - S_{21} - S_{12} + S_{22}\right) \tag{4-2}$$

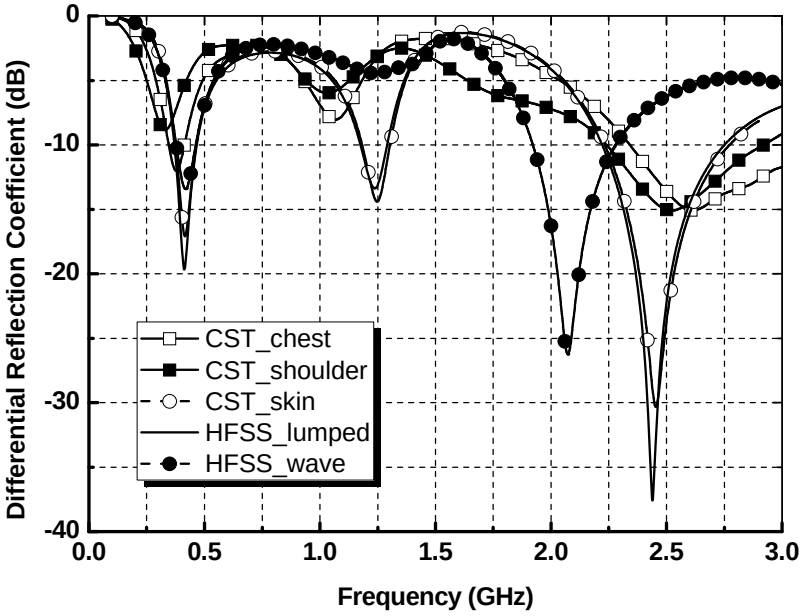

Figure 4-3 Comparison of differential reflection coefficient of planar antenna for different simulation setups.

The simulation results of differential reflection coefficient from HFSS and CST for different implantation setups are compared in Figure 4-3. From the figure we can see that the curves for CST and HFSS simulation results in one layer skin model almost coincide with each other. The resonant frequencies for HFSS lumped model simulation are 413 MHz and 2.44 GHz. The bandwidth ($|S_{11}| < -10$ dB) is 370 MHz ~ 466 MHz (23.0 %) for the lower band and 2.222 GHz ~ 2.752 GHz (21.3 %) for the upper band. For the actual implantation in chest and shoulder in CST Gustav human model, certain off-resonance can be seen. However, two resonant frequencies around 403.5 MHz MICS band and 2.45 GHz ISM can still be clearly noticed.

When the coaxial cables are applied to the feeding position as indicated by the curve HFSS_wave in Figure 4-3, the third resonance around 2.44 GHz shifts downwards to around 2.07 GHz, while the first resonance around 400

MHz remains more or less unaffected. This means that the antenna is more easily affected by the size of ground plane at higher frequency due to the fact that the SMA is electrically larger, the effect of which is neglected in lumped model simulation. We should take this in mind because for actual connection with IC chip, the effect of SMA should be absent while for antenna measurement alone, the effect will be quite evident, as can be seen from our measurement results presented in Section 4.4. The way to mitigate the effect is to increase the size of ground plane, which is obtained by increasing the value of *g* in Figure 4-1. This will not only change the resonance properties but will also increase the total size of the implantable antenna, which would be a disadvantage for actual implantation. However for system integration such as conformal capsule antenna case, the ground part can be intended for the position where battery is placed, as explained in the section 4.2.3 below.

4.2.3 Conformal Capsule Design and Simulation Results

When the antenna is designed on a flexible substrate, it can be wrapped around a cylinder-shaped device and be used in a biotelemetric capsule system for medical purposes. For actual implantation, physical size constraint has to be considered. From past researches, we can get that the approximate size of a capsule is 11 mm × 26 mm [36], 11 mm × 24 mm [90], and 10 mm × 32.1 mm [91]. The first number is the diameter and the second number is the length of the capsule.

We modified our planar antenna and designed a conformal one on a flexible substrate named polyimide (ε_r = 3.5, $tan\delta$ = 0.008) with a thickness of 0.15 mm. The outer and inner radius for the cylinder is 5 mm and 4.85 mm respectively. Also, the antenna is wrapped by parylene-C with a thickness of 0.1 mm and the whole size of the antenna including the encapsulation is 186.3 mm^3 ($\pi \times (5.1^2 - 4.75^2) \times 17.2$). The diameters for via holes are also 0.9 mm. The whole antenna (10.2 mm × 17.2 mm) is just slightly larger than a capsule's half size. Therefore for actual application we can extend the size of the ground plane and save this part of the capsule for implanting the battery and the necessary electronic circuits. The conceptual application in a capsule case is shown in Figure 4-4.

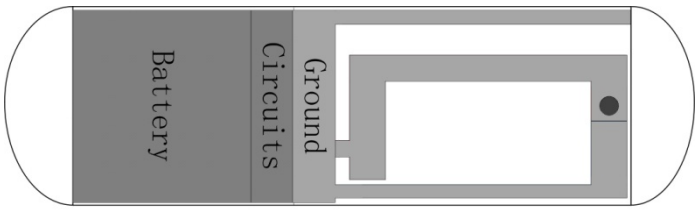

Figure 4-4 The conceptual application of the flexible antenna in a capsule.

The geometry of the flexible antenna is shown in Figure 4-5. The simulation environment in HFSS one layer skin model for the flexible antenna is the same as the planar one except that the center of the capsule cylinder is now 8 mm from the surface of the skin tissue. For HFSS simulation, we also add some coaxial cables along the feeding line to represent the effect of cables when doing actual measurement. In this case, wave port excitations are applied to the coaxial feeds. For CST simulation, we put the antenna in the stomach contents in Gustav human model. The selected volume for stomach implantation is (54, 0, 224) – (198, 127, 365). The simulation environment for CST stomach case is shown in Figure 4-5.

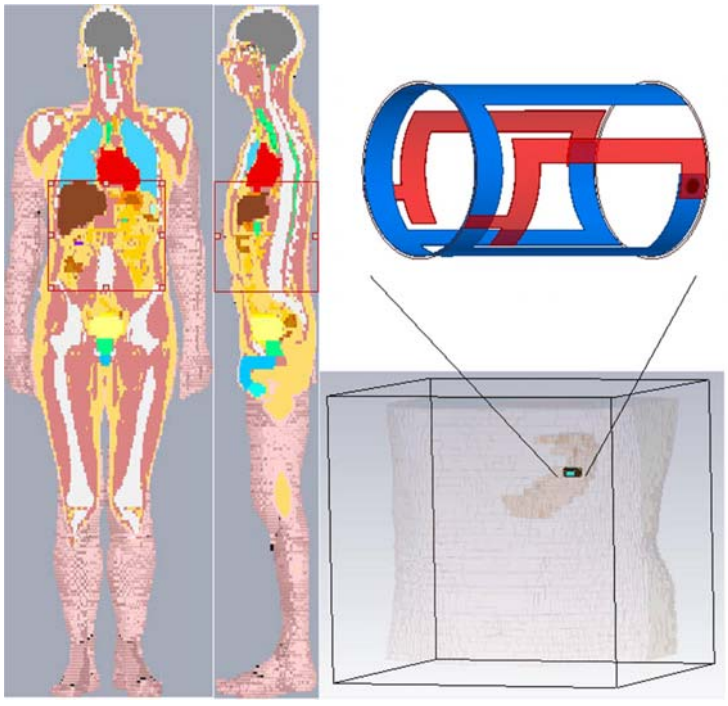

Figure 4-5 Geometry of the proposed flexible antenna and the simulation setup for CST stomach implantation.

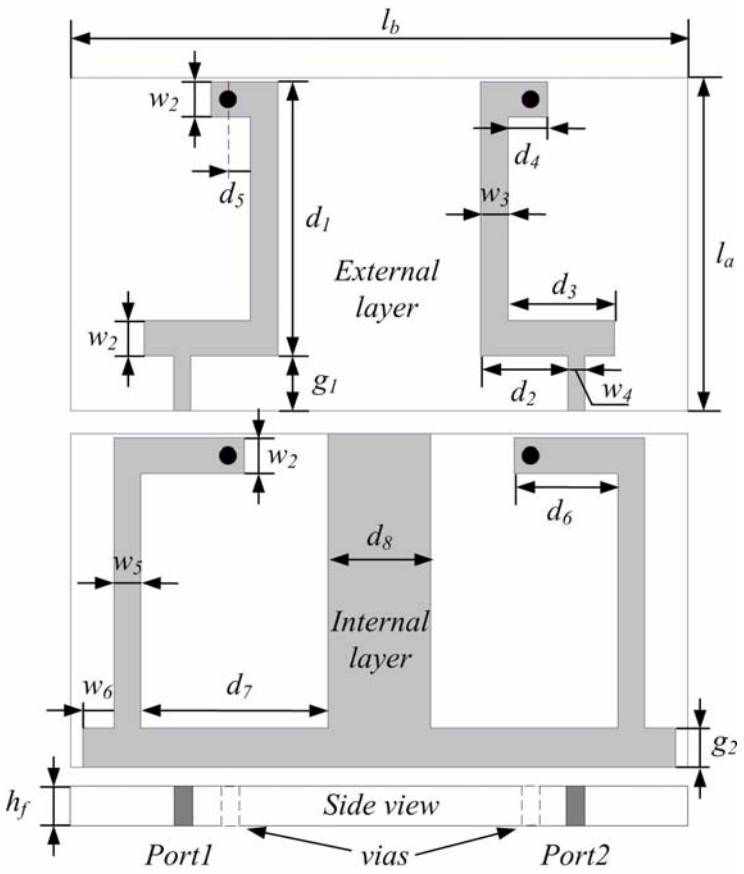

Figure 4-6 Geometrical parameters of the proposed flexible antenna when the conformal design is spread out.

For a clearer presentation of the conformal design, we make a cut at the bottom center of the antenna and spread the flexible substrate as shown in Figure 4-6, which is also the layout for fabrication. The geometrical dimensions of the design shown in Figure 4-6 are listed in Table 4-3.

Table 4-3 Geometrical dimension of proposed flexible antenna

Symbol	Value (mm)	Symbol	Value (mm)
l_a	17	d_1	14
l_b	31.4	d_2	4.45
w_2	1.8	d_3	5.41
w_3	1.4	d_4	2.01
w_4	0.87	d_5	1.15
w_5	1.34	d_6	5.28
w_6	1.59	d_7	9.53
g_1	2.8	d_8	5.24
g_2	2		

The comparison of simulation results from HFSS and CST for different implantation scenarios are shown in Figure 4-7. The bandwidths for the HFSS lumped case are 321 MHz ~ 532 MHz (49.5 %) for MICS band and 2.15 GHz ~ 2.74 GHz (24.1 %) for ISM band. From the figure we can see that for flexible case, 2.45 GHz ISM band is also more affected than 403 MHz MICS band. For the actual implant application in different scenarios, some further tuning of the geometrical parameters of the proposed antenna is necessary.

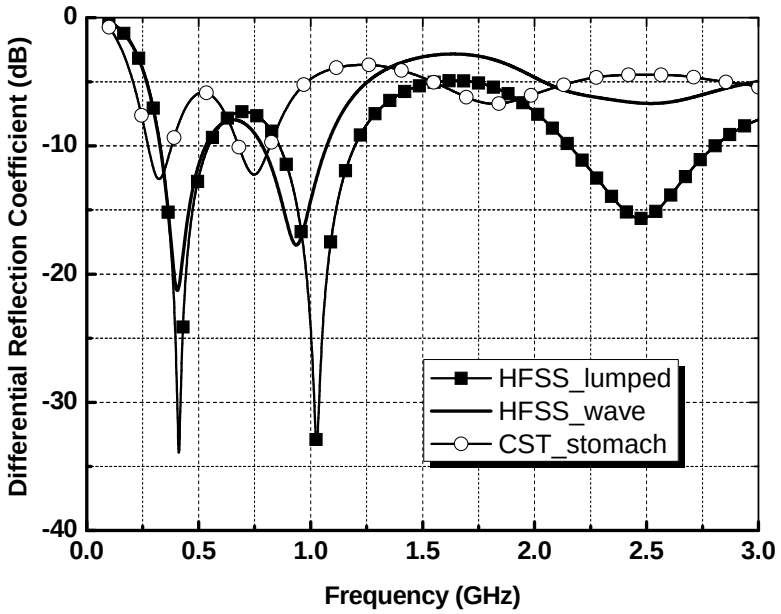

Figure 4-7 Comparison of differential reflection coefficient of flexible antenna for different simulation setups.

In consideration of the fact that the battery and the electronics may have effect on the performance of the antenna, we place a Perfect Electrical Conductor (PEC) cylinder with a size of 9.5 mm × 10 mm at the side of the antenna to test the robustness of matching performance as shown in case 1 of Figure 4-8. The inner part of the PEC coincides with the ground for a length of 2 mm. Therefore the total size of the antenna in case 1 is 10.2 mm × 25.2 mm, which is approximately the size of a capsule. For comparison, we also extended the size of ground plane (g_2 = 10 mm) as shown in case 2 of Figure 4-8. In all these cases, the feeding ports remain unchanged. Besides, for the ease of measurement, the inner part of the capsule is filled with tissue material for the original simulation model. In order to test the performance of the antenna in the real implantation application, we substitute the inner tissue

portion of the cylinder with a 9.5 mm × 10 mm vacuum layer, as in case 3 of Figure 4-8. Finally, we compare the HFSS simulation results of differential reflection coefficients from these three cases with the original one in Figure 4-9. For the feeding of all these structures, lumped ports are used.

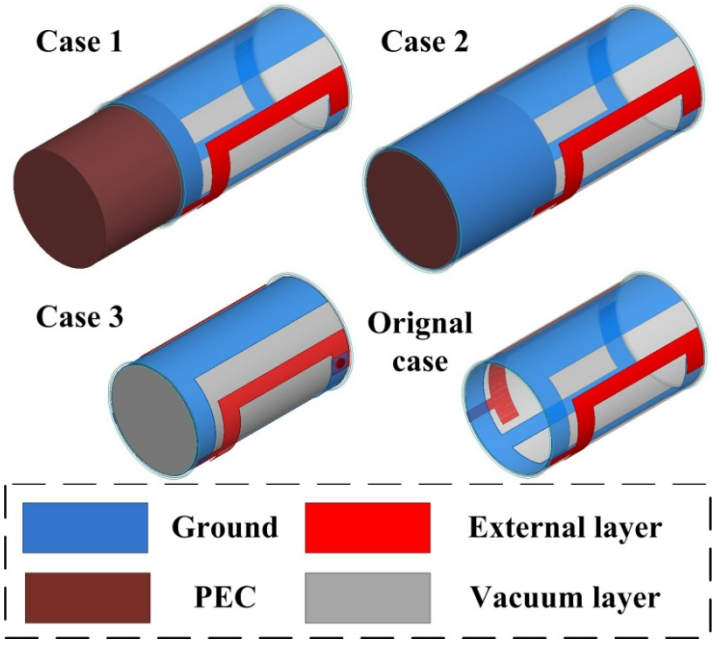

Figure 4-8 Simplified schematic for different simulation cases as in the real implantation scenarios.

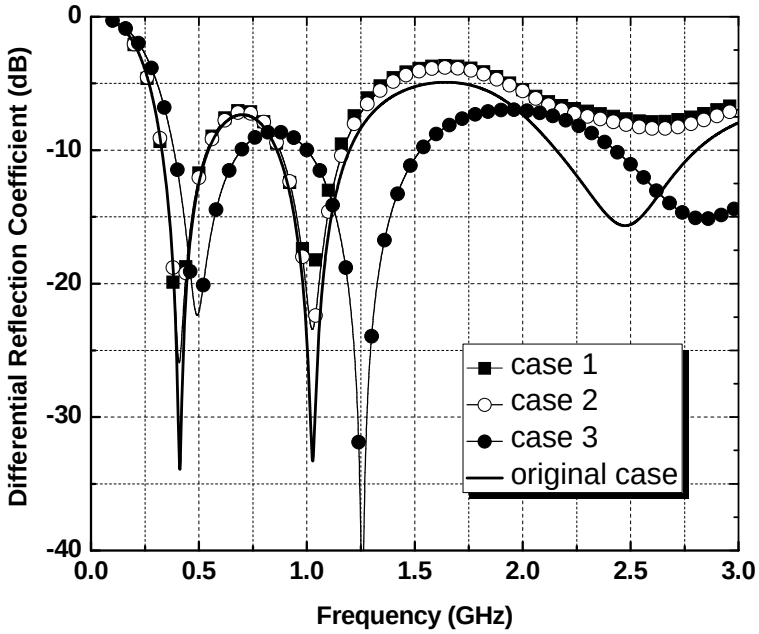

Figure 4-9 Comparison of differential reflection coefficients of flexible antenna for different simulation setups.

From Figure 4-9 we can see that compared with the original case, the first resonance remains unchanged with the PEC added (case 1), while the resonance around 2.45 GHz becomes weak, however the frequency shift is not significant. The curve of case 2 almost coincides with that of case 1, meaning extended ground plane will not affect the performance of the antenna as long as the positions of the feeding ports remain unchanged. With the inner portion of the capsule substituted by vacuum layer as in case 3, all resonance frequencies shift upwards. However, the matching is still decent for all resonance frequencies.

4.3 SAR and Radiation

For safety concerns, we should also evaluate the SAR, the standards of which are regulated by IEEE. IEEE Standard C95.1-2005 states that the 10-g averaged SAR should not exceed 2 W/kg [47]. The 10-g SAR values of the planar antenna and the flexible antenna at two resonant frequencies are listed in Table 4-4.

Table 4-4 SAR values of proposed antenna (Input power: 1 W)

Planar	**Value (W/kg)**	**Flexible**	**Value (W/kg)**
chest MICS	85.2	stomach MICS	72
chest ISM	77.8	stomach ISM	48.8
shoulder MICS	63.1		
shoulder ISM	76.0		

These values are obtained from a differential power input of 1 W, which means the maximum output power for the transmitter connected before the implantable antenna is 23.5 mW (13.7 dBm) for the planar antenna and 27.8 mW (14.4 dBm) for the flexible antenna. These values are much larger than most output power of transmitters (-25 dBm) for implantable applications [76], [42]. Also, it is much larger than the EIRP maximum limit of -16 dBm (25 μW). Or we can say that for a 25 μW input power, the maximum SAR value is 2.5e-5 × 85.2 = 2.13e-3 W/kg, which is much smaller than the stipulated 2 W/kg. As an example, SAR distributions of the planar antenna for chest and

shoulder implantation in MICS band for 1 W input power are shown in Figure 4-10.

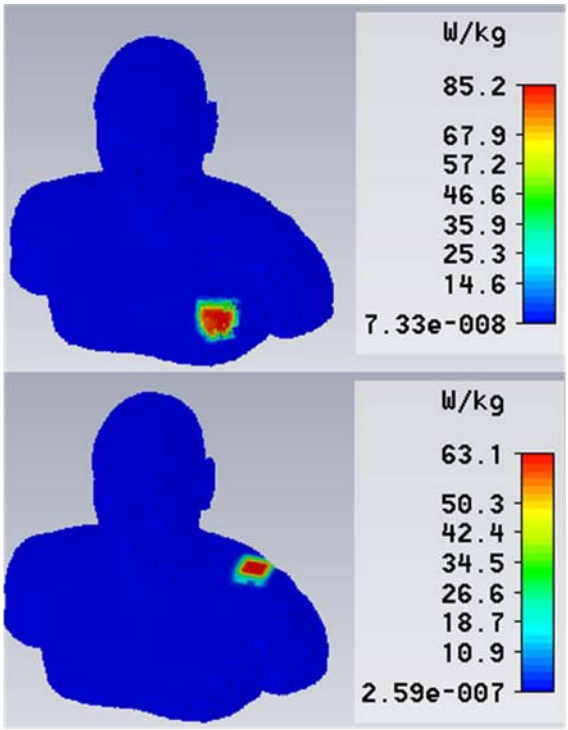

Figure 4-10 The SAR distribution of planar antenna for chest and shoulder implantation in MICS band (Input power: 1 W).

The radian distance $\lambda/2\pi$ is equivalent to 118mm and 20 mm for 403 MHz and 2.45 GHz. Therefore depending on the application, the external receiving unit may be in near-field or far-field region of the implanted antenna. And we evaluate both the radiation pattern and coupling strength S_{21} between the external half-wavelength dipole and the implanted antenna below. As an example, the radiation pattern for shoulder implantation for the planar antenna at both frequency bands is shown in Figure 4-11. From the figure we can see that the gain is –30.6 dB for 403.5 MHz MICS band and -19.1 dB for 2.45 GHz ISM band.

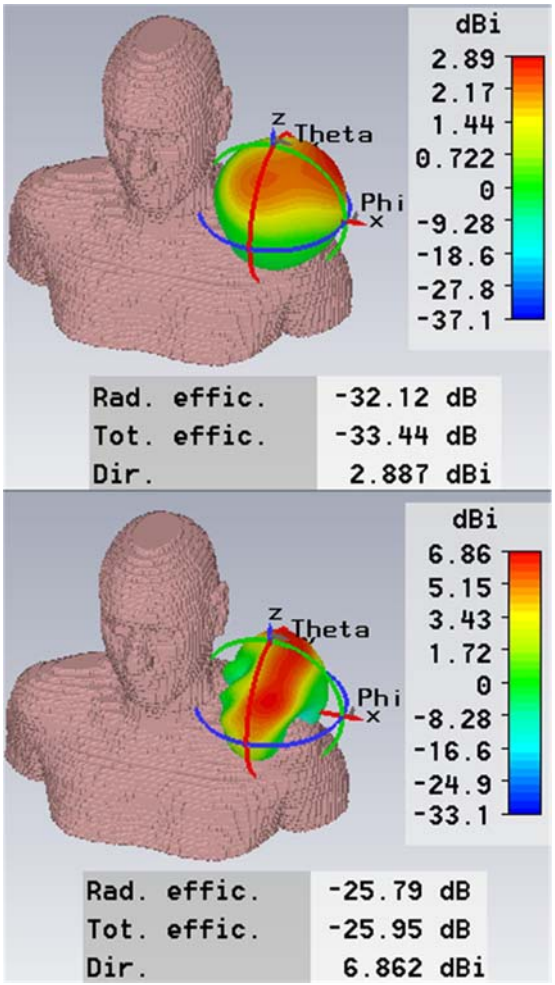

Figure 4-11 The radiation pattern of the planar antenna for shoulder implantation in MICS band and ISM band.

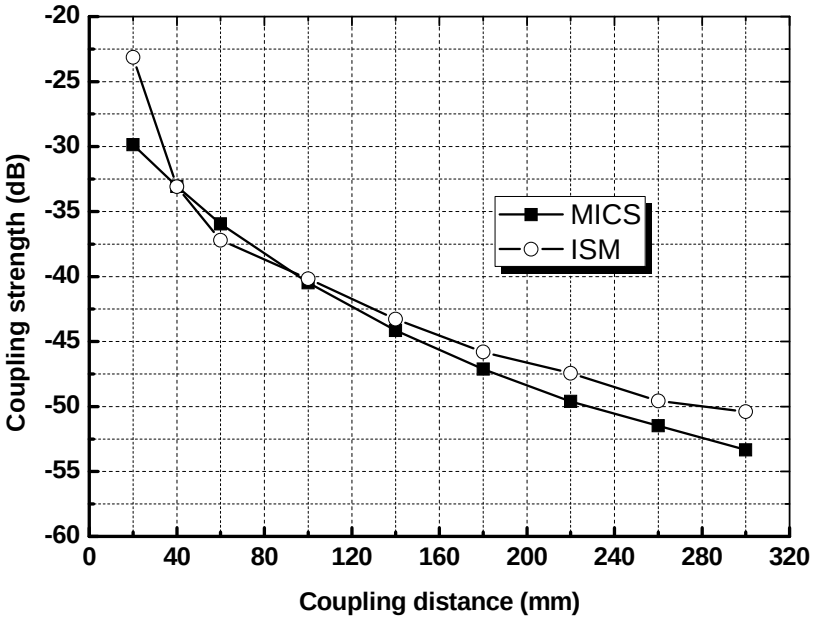

Figure 4-12 Coupling strength of external half-wavelength dipole with planar antenna in shoulder implantation for MICS band and ISM band.

The coupling strength between the external half-wavelength dipole and the implanted antenna is shown in Figure 4-12. The external dipole is constructed on board Roger 4003 (ε_r = 3.55, $tan\delta$ = 0.0027) with a thickness of 32 mil (0.813 mm). For each frequency band, a different dipole is adopted, and the total length of the dipole is 336.5 mm for MICS band and 51.5 mm for ISM band. From the figure we can see that for extreme close distance at 20 mm for instance, the coupling at ISM band is 6.7 dB higher than MICS band. Because for this distance, antennas are both within the near-field region and the gain for ISM band is larger. As the coupling distance increases, for ISM band it gradually enters the intermediate region, while for MICS band, it is still within near-field region. Therefore the coupling strength for MICS band takes over between a coupling distance of 40 mm and 100 mm. For coupling distance larger than 100 mm, the coupling at ISM band dominates again due to larger gain values. With this coupling strength, we can further do the link budget analysis as in section 3.5.

For the flexible antenna, as the gain for stomach implantation varied significantly as the antenna is moved from one position to another, we only give the gain of HFSS one layer implantation, which is -30.5 dB for MICS band, and -22.2 dB for ISM band. The gain values are similar to that of the planar case, so the coupling strength evaluation is not given for the flexible case.

4.4 Coating and In Vitro Measurement

4.4.1 Coating Process

After fabrication, both the planar antenna and the flexible antenna are coated by parylene-C with a thickness of 0.1 mm. The machine which is used to do the coating is shown in Figure 4-13.Some test samples are also used to confirm the final coating thickness. For the parylene to be coated on both sides of the antenna, we use some clips to hold the antennas and stick them up, and then pasted the clips to the coating platform. For every operating process of 8 hours, 25 um of parylene coating can be deposited, and 25 g of parylene is

needed according to our test samples. Therefore 4 iterations are performed for a total thickness of 100 um.

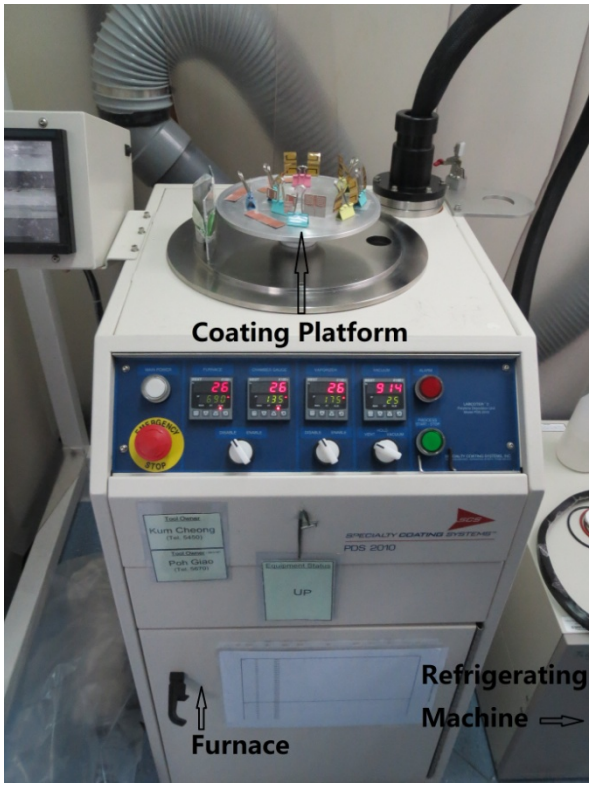

Figure 4-13 Machine used for coating the implantable antennas.

The general coating process is as follows:

Step 1: Switch on the refrigerating machine, which is connected to the main machine by the black tube shown in Figure 4-13. It will cool down the temperature of the coating platform so that a vacuum environment can be easily formed under the hermetic dome. The hermetic dome is not shown in Fig. 14 for better representation of the coating platform.

Step 2: 25 gram of parylene is weighed and put into the small furnace located in the bottom part of the machine.

Step 3: After around 30 minutes of cooling, put the hermetic dome over the coating platform and turn on the air evacuation switch.

Step 4: Turn on the furnace switch, and then parylene will be heated, vaporized and finally deposited on everything that has been placed within the hermetic dome.

4.4.2 In Vitro Measurement

The fabricated antennas after parylene coating are shown in Figure 4-14. The in-vitro measurement is performed in minced pork with a four-port network analyzer Rohde & Schwarz ZVA 50, which can perform differential return loss measurement directly, as shown in Figure 4-14.

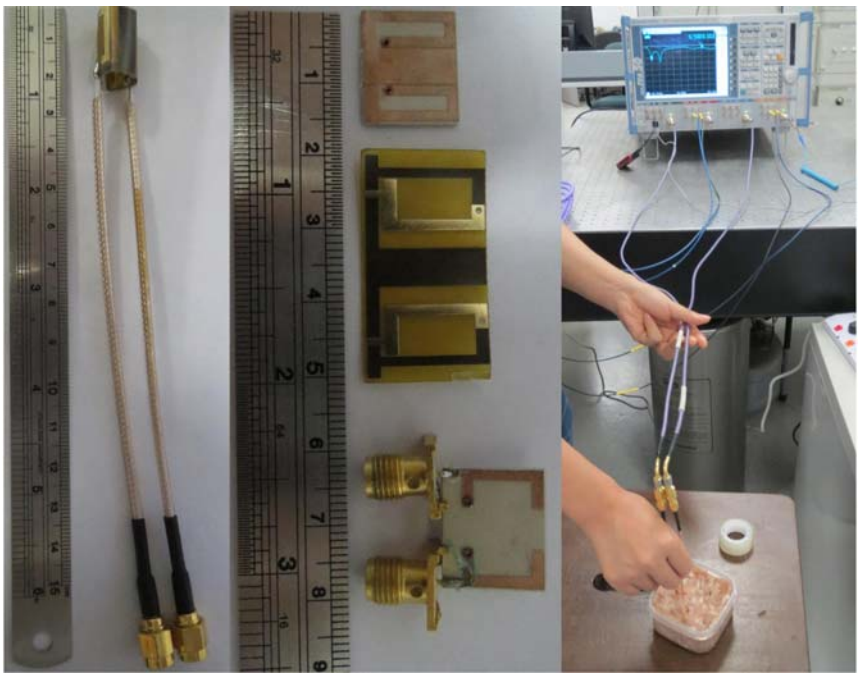

Figure 4-14 Fabricated implantable antenna and measurement setup for the implantable antenna.

The differential reflection coefficient of the planar antenna is shown in Figure 4-15. From the figure we can see that the results are generally the same at MICS band. While at 2.45 GHz ISM band, the curve of HFSS_lumped differs with the measurement result to a greater extent. This is caused by the effect of SMA connectors and cable being connected to the ports, which is neglected in lumped model. In wave port model, we add some cables alongside the ports, therefore the curve of HFSS_wave is closer to measurement result.

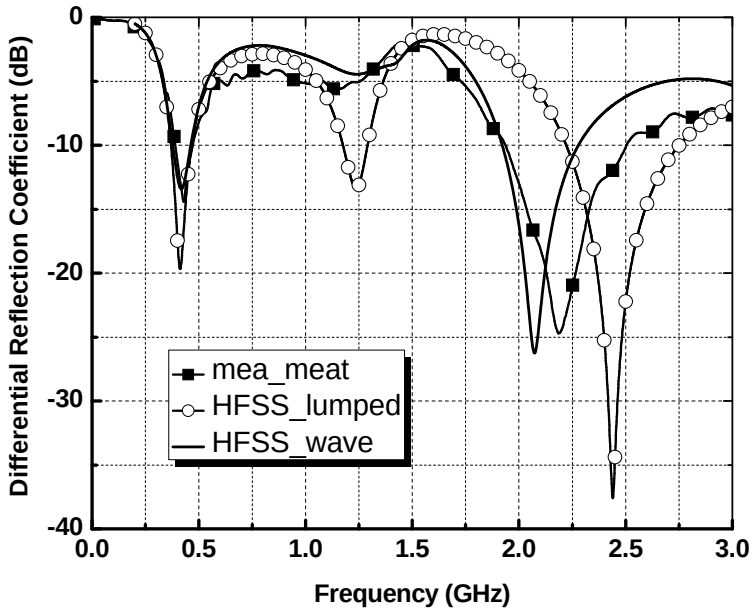

Figure 4-15 Comparison of differential reflection coefficients of measurement and simulation results for the planar antenna.

The comparison of differential reflection coefficients for flexible capsule antenna is shown in Figure 4-16. From the figure we can see that for the flexible antenna, 2.45 GHz ISM band is even more severely affected. Also, measurement result is closer to the curve of HFSS_wave due to the effect brought by the small ground and feeding cable.

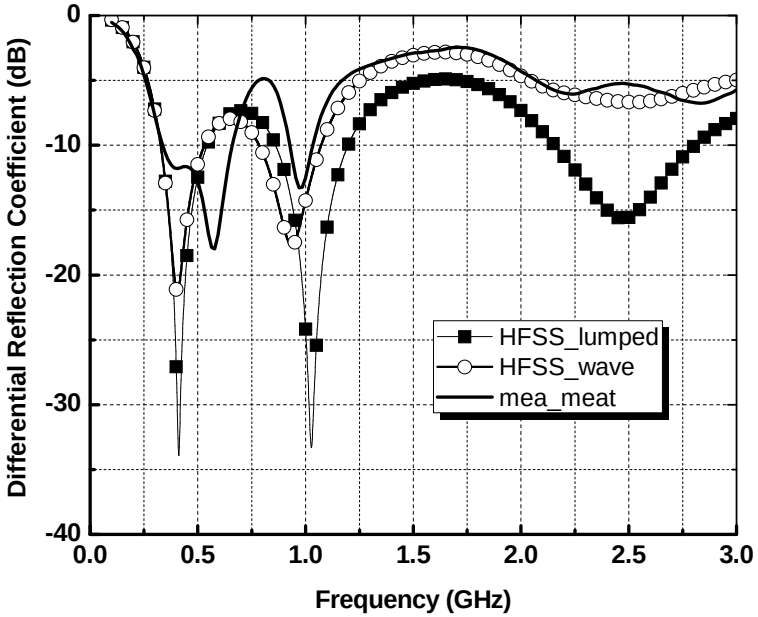

Figure 4-16 Comparison of differential reflection coefficients of measurement and simulation results for the flexible antenna.

4.5 Conclusion

A differentially-fed dual-band antenna operating at MICS and ISM bands has been proposed, and its possible application in flexible substrate can be intended for capsule antenna design. The radiation properties and SAR distribution are also evaluated. Measurement results in minced pork are compared with simulation in both HFSS one layer skin model and CST Gustav human model.

This type of antenna can be connected with a transmitter with differential output, eliminating the loss produced by baluns and matching circuits. Dual-band operation can be used in a circumstance with two modes: sleeping mode and work mode. During normal condition, the whole device would be in sleeping mode. When data transfer is required in 403.5 MHz MICS band, a wake up signal at 2.45 GHz ISM band is transmitted from external apparatus to start the internal device. In this way, power consumption can be reduced, extending the lifetime of the implanted device.

From our measurement, we found that 2.45 GHz ISM band is more easily affected when the environment changes, the case of which is also evident in previous dual-band work [9]. Therefore we should be more careful about the upper band and do some necessary tuning of the geometrical parameters of the design. Also, we may use some lower frequency band such as 915 MHz ISM band or 1.4 GHz WMTS band for startup signal to mitigate the detuning effect.

Chapter 5

Interference Evaluation for Power and Data Links

5.1 Introduction

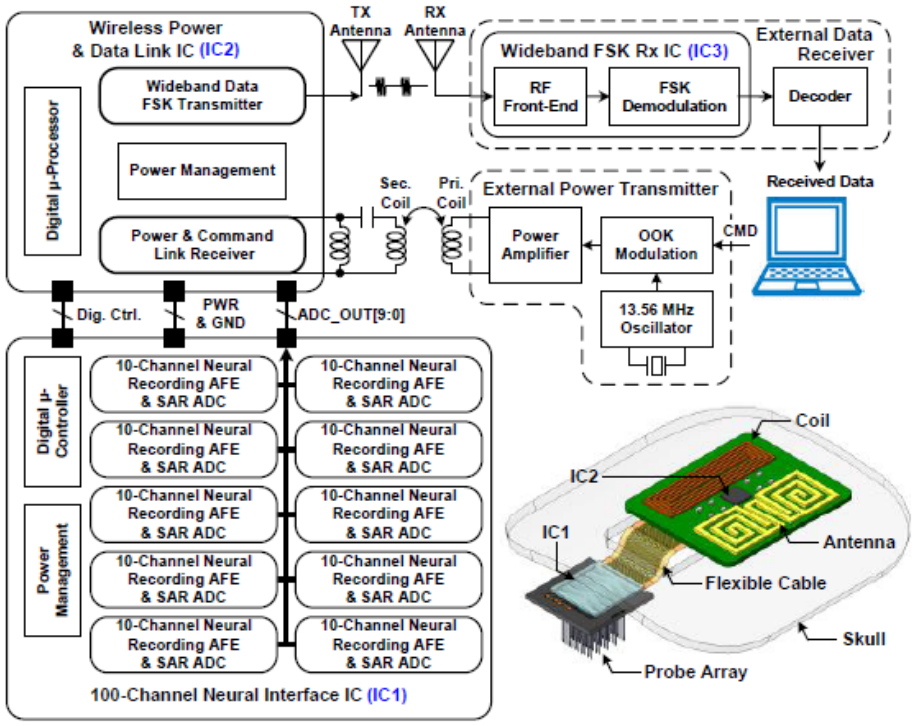

Figure 5-1 Overall system block diagram and conceptual drawing of fully implantable wireless neural recording microsystem [96].

For biomedical implantable applications, the wireless power link often requires high Q coils for maximum power transfer efficiency, while the data link requires low Q antennas or coils for larger bandwidth and a resulting larger data rate capability. Therefore for communication purposes, the wireless links are often realized by separate links, intended for power and data transfer respectively [16], [22]-[23], [96]. However, this may cause problems because of the interference between the power link and data link. For instance, the

overall system block diagram and conceptual drawing of fully implantable wireless neural recording microsystem is shown in Figure 5-1 [96].

IC1 is a 100-channel neural interface IC, which is connected with the probe array to collect the neural signals. IC2 is connected with IC1 by a flexible cable. IC2 is the wireless power and data link IC, which is responsible for collecting and sending the neural signal. For neural recording applications, the bandwidth requirement for the data link is comparatively larger, entering several or dozens of megahertz range. Therefore the data link is implemented by coupling antennas operating at UHF rather than traditional inductive coils operating at HF. The whole system is powered by a wireless power link composed of two rectangular coils. IC3 is the receiver IC, which is used to receive the neural signal and further send it to decoder and computer for process. In this figure, the power link is placed side by side with data link, causing possible interference. Therefore, in this chapter, we investigate this issue and evaluate the effect of them on each other.

5.2 Overview of the Communication Link

For the communication link evaluation, we assume that the implanted device is immersed in a skin tissue, the permittivity and loss tangent of which at all frequencies can be found in [44]. The implanted device is supported by Rogers 6010 with a permittivity ε_r of 10.2 and loss tangent $tan\delta$ of 0.0023. The thickness of the substrate is 25 mil (0.635 mm). Also, a superstrate with the same material and thickness as substrate is used for the protection of the implanted device from the conducting influence of human tissue.

For the investigation of the interference between power link and data link in this chapter, we also make some other assumptions as follows:

1) The distance between the power coils is 10 mm. The operating frequency is 13.56 MHz, which is both an RFID band and ISM band. The distance between data link, which operates at 403 MHz MICS band, is 100 mm.

2) Due to the size restriction for internal devices, we fix the total internal implant size at 25 mm × 25 mm. We leave half space for the implanted

antenna and half space for the internal power coil, and the spacing between them is 1 mm. Also, the spacing between each turn of both power coils is fixed at 0.1 mm.

3) There is a superstrate for both the internal power coil and the implanted antenna.

4) The power coils and the antennas are perfectly aligned respectively. We do not investigate misalignment issues in this chapter.

The simplified overview of the communication link implanted in a head model is shown in Figure 5-2, and we define the external power coil as P_{ex}, the internal power coil as P_{in}, the external antenna for data transfer as D_{ex}, and the internal antenna as D_{in}. These symbols will be used through this chapter.

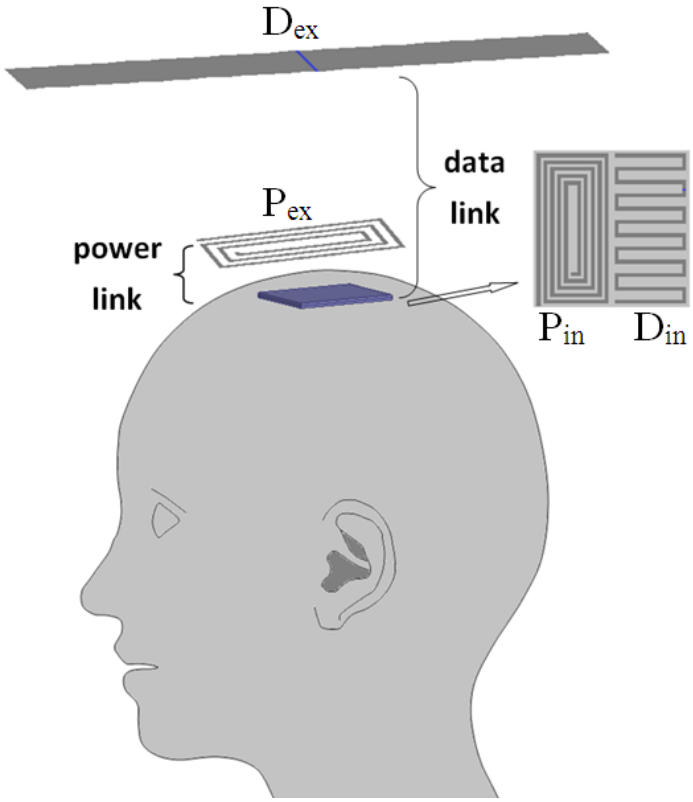

Figure 5-2 Overview of the communication link.

5.3 Investigation of Power and Data links and the Interference

5.3.1 Power Link

For simplification, we assume that the skin tissue size is a cubic box with a size of 100 mm × 100 mm × 50 mm, with 2 mm thickness of tissue above the implanted device. At first, we ignore the implanted antenna and optimize the power link alone. We leave a 0.5 mm margin between the edge of substrate and the internal coil. Because the spacing between implanted coil and antenna is 1 mm, the space for the secondary coil is 11.5 mm × 24 mm, and we assume the number of its turns is 10. For power coils optimization explained in Chapter 2, we found that the best ratio between the length of innermost turn and outermost turn is around 0.2 [20], meaning the trace width for the internal coil is 0.38 mm in this case.

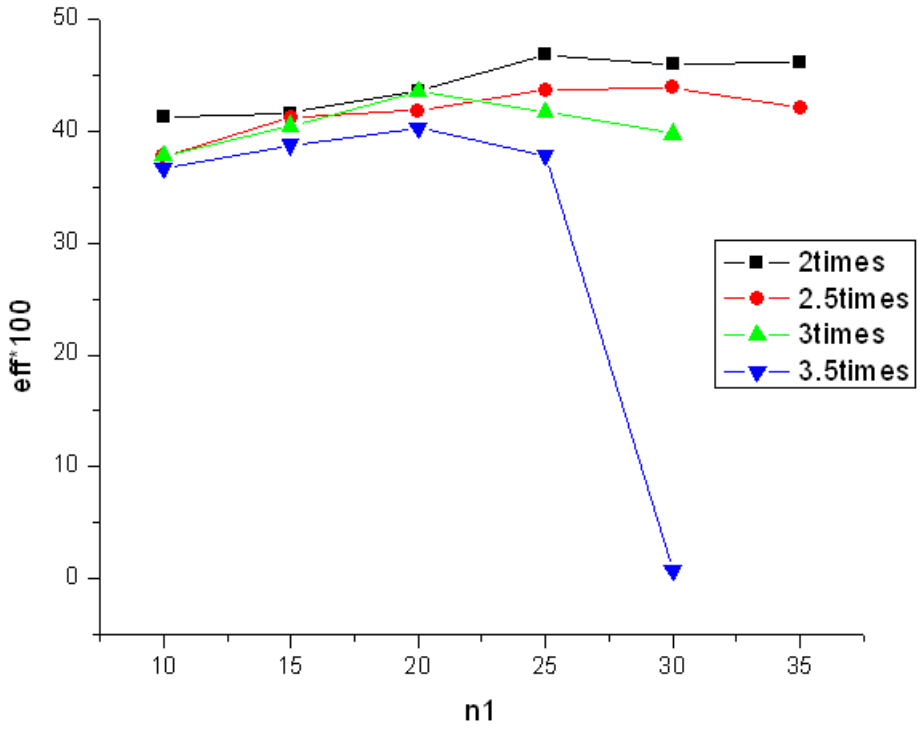

Figure 5-3 The optimization of external coil.

At first we assume the external coil to be the same size as the internal one. Then we gradually increase the size of external coil from two times the size of internal coil to three and a half times and compare the efficiency versus

number of turns n_1 for primary coil in Figure 5-3 according to the power efficiency equation proposed in [20].

From the figure we can see that when the size of external coil is 2 times and 2.5 times of internal coil, the maximum efficiency occurs when n_1 = 25, more turns will cause a slight reduction for the efficiency. When the size of external coil is 3 times and 3.5 times of internal coil, the maximum efficiency occurs when n_1 = 20, more turns for larger coil will cause the Self Resonant Frequency (SRF) to reduce and gradually approach 13.56MHz, leading to a serious reduction of efficiency. The size of final optimized external coil is 23 mm × 48 mm, the trace width and number of turns is 0.28 mm and 25 respectively.

5.3.2 Data Link

Data link are either realized by near-field data coil or far-field antennas. For implantable antennas, often 403 MHz MICS band [26] or 2.45 GHz ISM band [38] is selected as the operating frequency. A dual-band antenna operating at these two frequency bands was also proposed [9]. And the antenna structure is either in the form of a PIFA [9], [26] or a meandered dipole [24], [36]. A meandered dipole is used extensively for biomedical applications due to its small size, larger bandwidth and conformal capabilities. For the data link design, we also removed that power link and then designed an off-center fed meandered dipole operating at 403 MHz. The off-center feeding is to ensure better matching [36]. The size of the implanted antenna is also 11.5 mm × 24 mm. For the external antenna, we just designed a simple dipole antenna operating at 403 MHz.

5.3.3 Interference

The implanted coil together with the antenna is shown in Figure 5-4. The size of internal coil is 11.5 mm × 24 mm, the trace width and number of turns is 0.38 mm and 10 respectively. The size of the implanted antenna is also 11.5 mm × 24 mm, spaced 1 mm from the internal coil. From our simulation in HFSS, we found that the presence of the antenna does not have any influence on the efficiency for the power link.

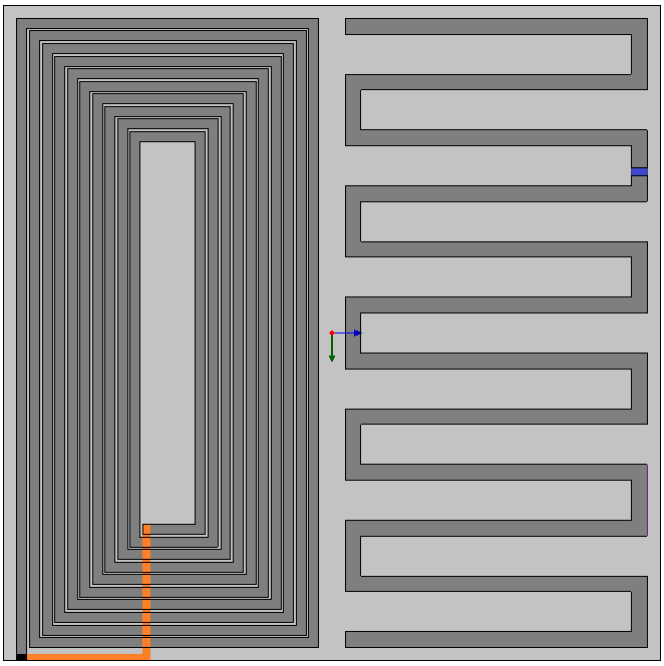

Figure 5-4 The implanted coil and off-center fed meandered dipole antenna.

For the effect of power link on the data link, we evaluate it from several aspects. Firstly, we view two antennas as a two-port system, and define the port of D_{ex} as port 1 and the port of D_{in} as port 2. And we evaluate the coupling strength S_{21} between D_{ex} and D_{in} with and without the power link. When expressed in decibel, $|S_{21}|$ should be the same value of received power over transmitted power P_R/P_T and the negative value of path loss. It can be further used to calculate the link margin for the whole system. The value of $|S_{21}|$ expressed in dB of the data coupling link versus the distance with and without the power coils are shown in Figure 5-5. From the figure we can see that the difference between $|S_{21}|$ with and without the power link is quite small, only about 1 dB.

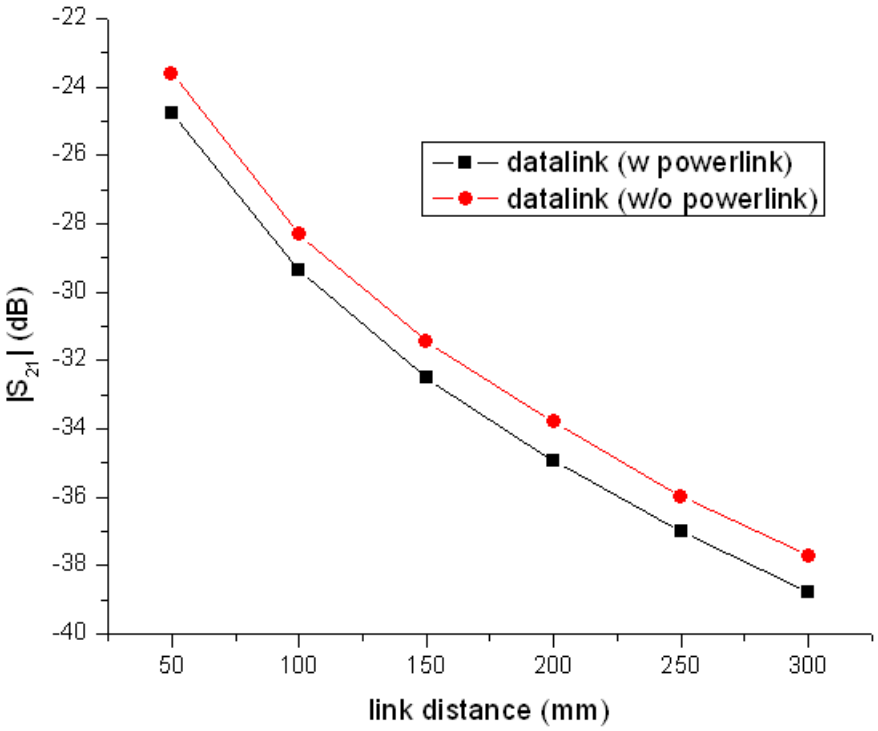

Figure 5-5 Coupling strength between external and internal antennas versus the distance between them.

Furthermore, we view the whole implanted coil, implanted antenna, external coil and external antenna as a four-port system. P_{ex} is the only source where power is generated from external apparatus. For the power link composed of P_{ex} and P_{in}, serial-parallel structure is used, meaning the primary side is in serial resonance and the secondary side is in parallel resonance. The topology selection of power link has been investigated previously [97].

S parameters of the whole structure is simulated in HFSS and then exported and used in the schematic of ADS as shown in Figure 5-6. Some power probes are added to simulate the power efficiency at 13.56 MHz. For the power link used in ADS schematic, the secondary power coil P_{in} is 1 kΩ loaded as in Chapter 2. And the data link composed of two antennas D_{ex} and D_{in} are both 50 Ω loaded.

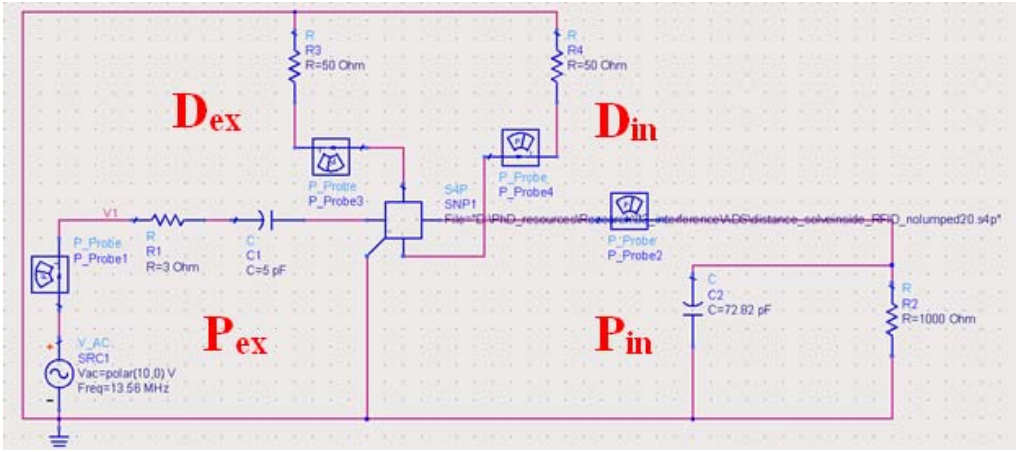

Figure 5-6 ADS schematic for calculating the coupling strength.

As the distance between D_{ex} and D_{in} is decreased from 100 mm to 20 mm, the power ratio of P_{Pin}/P_{Pex}, P_{Din}/P_{Pex}, P_{Dex}/P_{Pex} with respect to the distance between D_{ex} and D_{in} at 13.56 MHz is shown in Figure 5-7. The black curve indicates the power efficiency from P_{ex} to P_{in}, which is relatively stable. Two blue curves indicate the coupled power from P_{ex} side to the data link composed of D_{ex} and D_{in}.

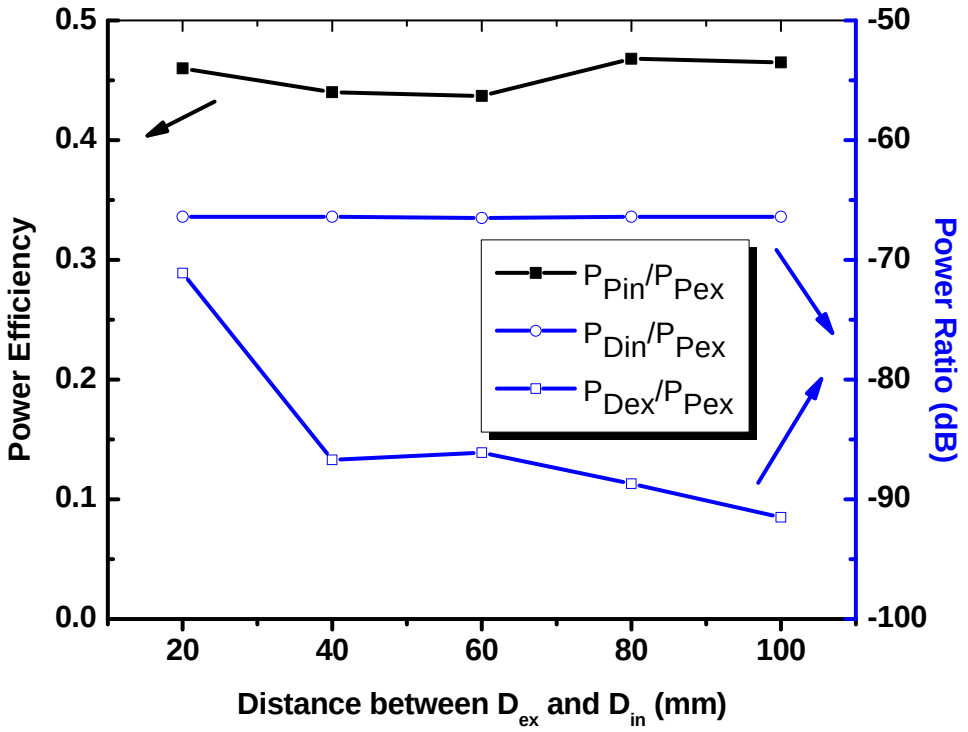

Figure 5-7 Power ratio of P_{Pin}/P_{Pex}, P_{Din}/P_{Pex}, P_{Dex}/P_{Pex} with respect to the distance between D_{ex} and D_{in} at 13.56 MHz.

From the figure, we can see that P_{Pin}/P_{Pex} and P_{Din}/P_{Pex} almost remain the same, while P_{Dex}/P_{Pex} becomes larger when the external antenna gets closer to the implanted system. The coupling strength between D_{ex} and D_{in} with the power link at 403 MHz is shown in Table 5-1.

Table 5-1 Coupling strength between D_{ex} and D_{in} with the power link at 403 MHz

distance (mm)	coupling (dB)
20	-20.4
40	-23.5
60	-25.8
80	-27.7
100	-29.3

For a specific example in the neural recording system [96], the power level is 14.2 dBm for P_{ex}, -25 dBm for D_{in} [8]. Therefore now we can get the desired power amplitude at 403 MHz and unwanted power amplitude at 13.56 MHz for both D_{ex} and D_{in}, as shown in Figure 5-8.

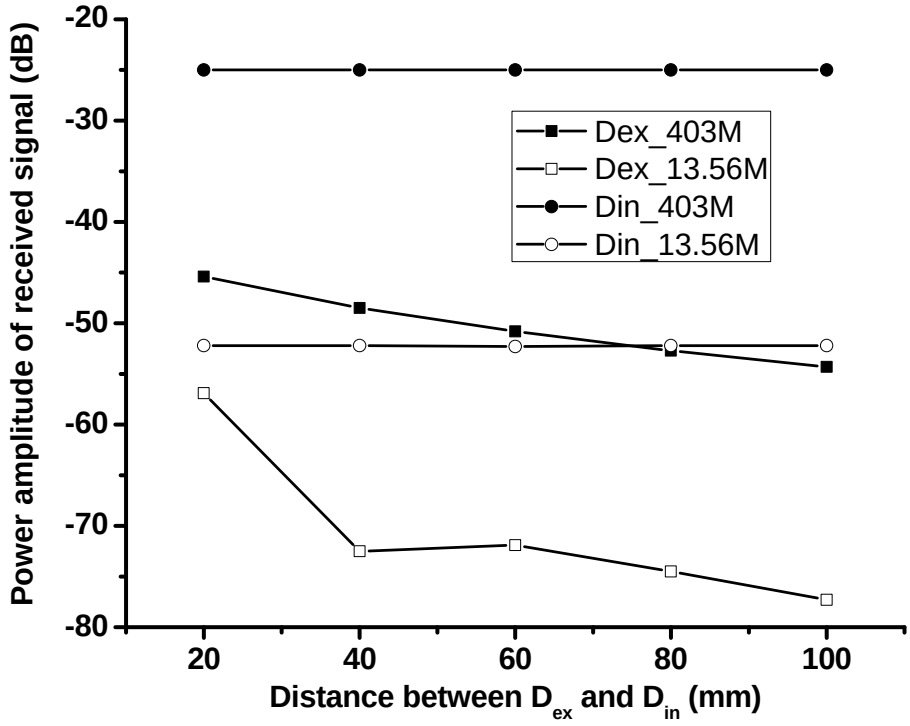

Figure 5-8 Desired power amplitude and unwanted power amplitude for D_{ex} and D_{in} versus the distance between D_{ex} and D_{in}.

From the figure we can see that when the distance between D_{ex} and D_{in} is reduced to 20 mm, the unwanted power amplitude at D_{ex} is closest to the desired power amplitude, which is still 11.4 dB lower. Therefore, the interference at 13.56 MHz indicated by the empty symbol line is negligible for both D_{ex} and D_{in}.

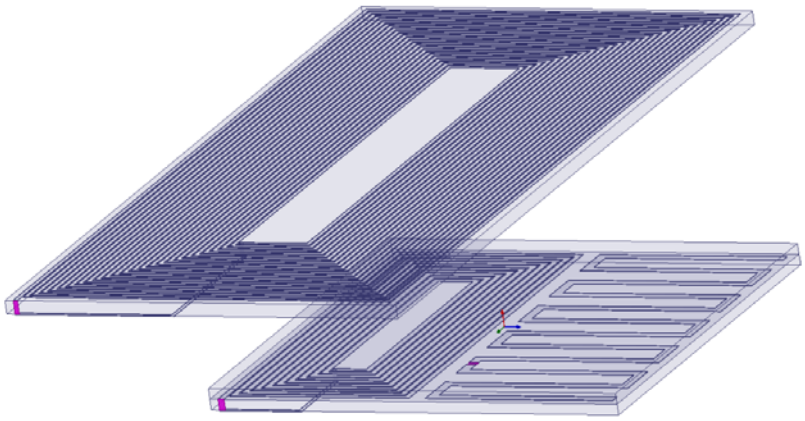

(a)

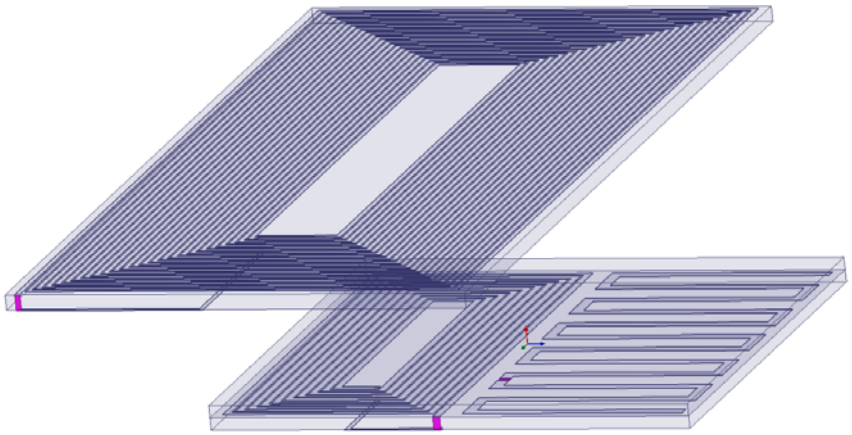

(b)

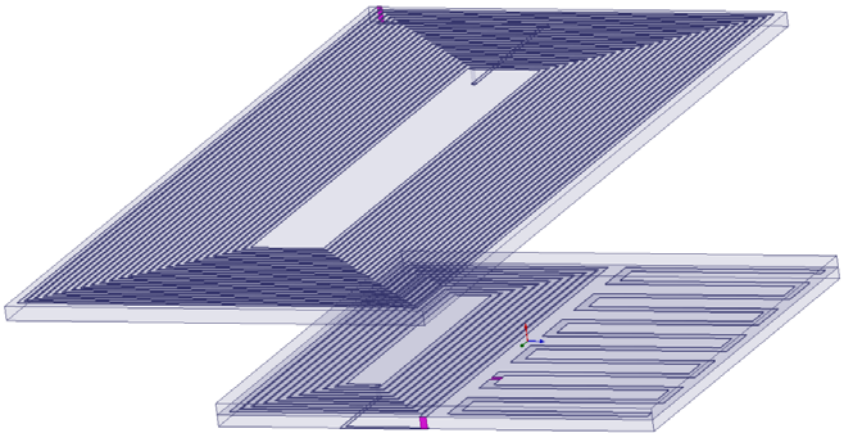

(c)

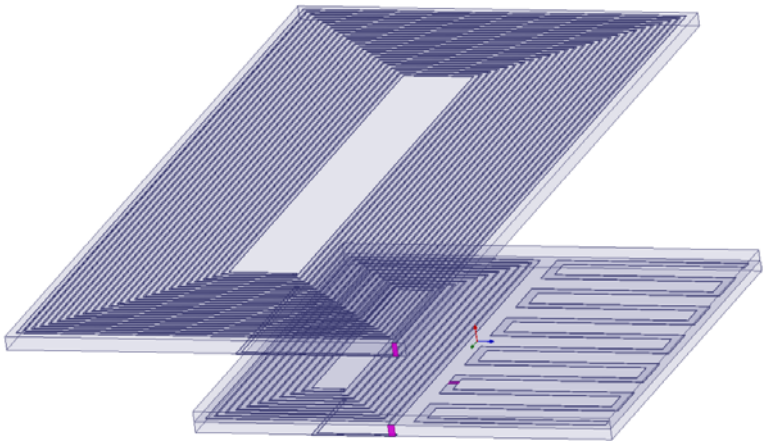

(d)

Figure 5-9 Different ports' locations for P_{ex}, P_{in} and D_{in} (a) Both the ports of P_{ex} and P_{in} are away from port of D_{in} (b) The port of P_{ex} is away from D_{in} while P_{in} is near the port of D_{in} (c) The port of P_{ex} is further located away from D_{in} while P_{in} is near the port of D_{in} (d) Both the ports of P_{ex} and D_{in} are located near the port of D_{in}.

Finally, we evaluate the effect of the port's location on the coupling strength. And we change the ports' locations as shown in Figure 5-9. In previous simulation, the port is placed as in Figure 5-9 (a). If we change to the ports' configuration to three other cases as in the Figure 5-9, the desired power amplitude and interference power amplitude are compared in Figure 5-10.

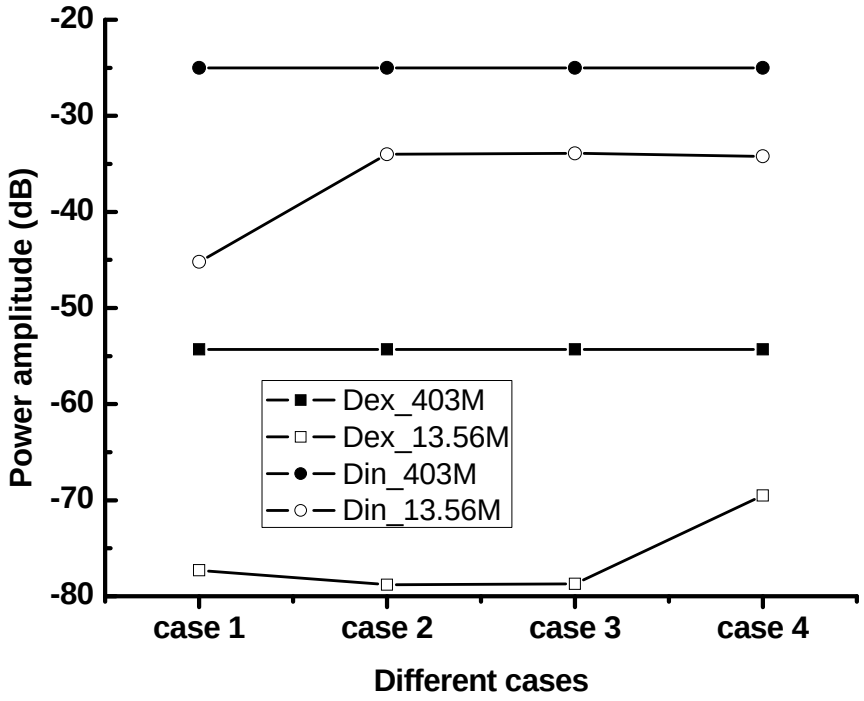

Figure 5-10 Desired power amplitude and unwanted power amplitude for D_{ex} and D_{in} versus different cases for ports' locations.

From the figure we can see that the biggest interference comes from the ports' configuration of case 4. The unwanted signal at D_{ex} side at 13.56 MHz is increased to -69.5 dBm, which is still 15.3 dB lower than the received signal strength of -54.3 dBm. The unwanted signal at D_{in} side at 13.56 MHz is increased to -34 dBm, which is still 9 dB lower than the output power of -25 dBm. Therefore, the interference is negligible for all cases. However, if feeding location for the implanted coil is supposed to be extremely close to the feeding port of the implanted antenna, then possible interference from the power link to the data link may exist.

Consequently, for minimum interference, three methods can be adopted. Firstly, for minimum interference to the receiver located outside the body, the external antenna should be placed at certain distance away from the implanted system. For the operating frequency used in this chapter, a minimum distance of 20 mm is recommended. Secondly, for IC2 shown in Figure 5-1, the port for the power input and data output should be located away from each other. Finally, we can further increase the frequency separation. For instance, we can further reduce the power transferring frequency to 6.78 MHz ISM band and increase the data transferring frequency to 915 MHz ISM band or 2.45 GHz ISM band.

Chapter 6

Conclusion

6.1 Thesis Assessment

This thesis evaluates the whole telemetry link for the implanted device, including the link for wireless power transfer and the link for data transmission. The prominent aspects which differ from previous work can be summarized as follows:

Chapter 2 proposes the systematic method for improving the power transferring efficiency for rectangular coils and presents a new and simple method for calculating the power efficiency.

For practical applications, the space left for power coupling coils design may presents certain shape other than square or circular shape, therefore in this case rectangular shape serves as a more general and favorable solution. Also, for a given space, rectangular coils fully utilize the area for maximum mutual inductance and therefore the mutual coupling between them.

Additionally, previous equation for mutual coupling calculation is only available for circular shape. For the square coils' case [17], the equation is just the same as circular one with a coefficient added, which is not accurate and cannot be adapted to the rectangular case. Therefore, we propose a new method for calculating the mutual inductance between rectangular or square coils.

Due to the fact that the resistance of coil is very sensitive with respect to the thickness of copper, we should take into account of the skin effect. Therefore in HFSS simulation, we should tick the "solve inside" option for the copper. This will lead to a tediously long simulation time for the multi-turn

coupling coils, especially at low frequency range at several megahertz. Consequently, we should first model the coupling coils based on lumped component model and execute the optimization by Matlab codes, and then do the final tuning of the geometrical parameters of rectangular coils with HFSS. Finally, the lumped component modeling results and HFSS simulation results are compared with measurement for comparison.

Chapter 3 proposes a differentially fed dual-band implantable antenna for the wireless neural recording application for the first time. The central frequencies are around 433.92 MHz and 542.4 MHz, which are both near the 402 ~ 405 MHz MICS band. The transmitter connected before the antenna is a burst-mode injection-locked FSK transmitter. The capacitor bank in the LC oscillator of the transmitter sets the free-running frequency close to f_0 of 542.4 MHz or f_1 of 433.92 MHz for data of '0' or '1'. The benefit of the differential configuration for an implantable antenna is to facilitate its connection with transmitter with differential output, eliminating the loss introduced by baluns and matching circuits.

In this chapter, the antenna is implanted into single skin tissue model and three-layer tissue model composed of skin, fat and muscle for comparison. The SAR distribution is evaluated, and the simulation result of differential reflection coefficient is compared with measurement result in skin-mimicking tissue with a composition of 56.18% sugar, 2.33% salt and 41.49% deionized water. Additionally, the link performance between the implanted antenna and external dual-band half-wavelength dipole is also presented, with the link budget analysis performed at last. Finally, in-vitro test of the communication link in minced pork with the circuits connected is presented.

Chapter 4 proposes a differentially fed dual-band implantable antenna with biocompatible insulation operating at both 403 MHz MICS and 2.45GHz ISM band for the first time. Its planar form and flexible form are both explored. The bandwidths of both cases are much larger than the antenna presented in Chapter 3.

Dual-band capability can ensure the antenna's application in system with two modes: sleep mode and wake-up mode. MICS band can be used for data communication and ISM band can be intended for wake-up signal, and the system will only consume power when being trigged by the wake-up signal. In this way, the lifetime of the implanted system can be extended.

Both the planar and flexible antennas are covered with a biocompatible material parylene-C, which can protect the antenna from the conducting influence of the human tissue. Its flexible form can be intended for capsule antenna design in the future.

The simulation is not only done in HFSS tissue models, but also performed in a CST male human model named Gustav with a size of 532.48 × 264.16 × 1764 mm^3. The planar form in Gustav shoulder and chest implantation and the flexible form in stomach implantation are evaluated. Additionally, the differential reflection coefficient of the flexible form is evaluated in capsule application with PEC cylinder representing the battery and circuits. Also the SAR distribution and radiation properties are given. Finally, the simulation results are compared with measurement results in minced pork.

Chapter 5 evaluates the interference between coupling antennas and coils in one-layer skin tissue model for the first time. Previous studies only deal with power link and data link both composed of coupling coils operating at several or dozens of megahertz.

For the protection from the conducting effect of human tissue, superstrate is added for both the implanted antenna and internal coil. From the presented simulation results, we found that the effect of antennas on the coupling coils is negligible. For the coils' effect on coupling antennas, three methods can be adopted for minimization of the interference. Firstly, the external antenna should be placed far away from the implant. Secondly, the feeding ports of the implanted coil and of the implanted antenna should be located as far away from each other as possible. Finally, further frequency separation between power link and data link can be implemented.

6.2 Future Work

We have addressed several issues in our work. However, there is still room for improvement or extension. And some future work can be performed in the following aspects.

(1) For the wireless power transfer, the effect of lateral and angle misalignment on power transfer efficiency can be systematically investigated. Also, the optimization of power efficiency with multiple varying parameters would be extremely meaningful.

(2) For wireless power transfer, higher operating frequency would ensure higher self inductance and mutual inductance. However, the resistance would also be increased, reducing the quality factor. Therefore, if a maximum size for the implanted coil has been given, the evaluation of optimum operating frequency for coupling coils would be extremely meaningful.

(3) For data transfer realized by coupling antennas, high operating frequency makes the miniaturization of implanted antenna possible. However the tissue absorption of the electromagnetic propagation would be also larger. Considering the size constraint for the implantable antenna, the evaluation of optimum operating frequency for coupling antennas would also be of significant value.

(4) For the reduction of interference of power link on the data link, we used separate frequencies for each of them. The effect of frequency separation on the mutual influence of power link and data link can be more thoroughly investigated.

(5) Finally, for all experiments, both in-vitro and in-vivo tests should be performed to ensure the work's reliability.

BIBLIOGRAPHY

[1] D. Panescu, "Emerging technologies [wireless communication systems for implantable medical devices]," *IEEE Eng. Med. Biol. Mag.*, vol. 27, no. 2, pp. 96–101, Mar.-Apr. 2008.

[2] C. M. Furse, R. Harrison and F. Solzbacher, "Recent Advances in BioMedical Telemetry", *International Conference on Electromagnetics in Advanced Applications*, Sep. 2007, pp. 1026-1027.

[3] E. Feigenbaum, "Cochlear Implant Devices for the Profoundly Hearing Impaired", *IEEE Eng. Med. Biol. Mag.*, vol. 6, no. 2, pp. 10–21, Jun. 1987.

[4] T. Buchegger, et al., "An ultra-low power transcutaneous impulse radio link for cochlea implants," in *Joint Ultra Wideband Systems and Technologies (UWBST) and International Workshop on UWBS*, May 2004, pp. 356-360.

[5] K. Gosalia, G. Lazzi, and M. Humayun, "Investigation of a microwave data telemetry link for a retinal prosthesis," *IEEE Trans. Microw. Theory Tech.*, vol. 52, no. 7, pp. 1925-1933, Aug. 2004.

[6] S. Soora, K. Gosalia, M. S. Humayun, and G. Lazzi, "A Comparison of Two and Three Dimensional Dipole Antennas for an Implantable Retinal Prosthesis", *IEEE Trans. Antennas Propag.*, vol. 56, no. 3, pp. 622-629, Mar. 2008.

[7] R. R. Harrison et al., "A low-power integrated circuits for a wireless 100-electrode neural recording system," *IEEE J. Solid-State Circuits*, vol. 42, no. 1, pp. 123-133, Jan. 2007.

[8] Z. M. Chen, K. W. Cheng, Y. J. Zheng, and M. Je, "A 3.4 mW 54.24 Mbps burst-mode injection-locked CMOS FSK transmitter," in *Proc. IEEE Asian Solid State Circuits Conf.*, Nov. 14–16, 2011, pp. 289–292.

[9] T. Karacolak, A. Z. Hood, and E. Topsakal, “Design of a dual-band implantable antenna and development of skin mimicking gels for continuous glucose monitoring,” *IEEE Trans. Microw. Theory Tech.*, vol. 56, no. 4, pp. 1001-1008, Apr. 2008.

[10] P. Valdastri, A. Menciassi, A. Arena, C. Caccamo, and P. Dario, “An Implantable Telemetry Platform System for In Vivo Monitoring of Physiological Parameters,” *IEEE Trans. Inform. Technol. Biomed*, vol. 8, no. 3, pp. 271-278, Sep. 2004.

[11] Xu, Y. P., Yen, S-C., Ng, K. A., Liu, X., Tan, T. C. "A Bionic Neural Link for Peripheral Nerve Repair," *34th International Annual Conference of the IEEE Engineering in Medicine & Biology Society (EMBC)*, San Diego, USA, 28 Aug - 1 Sept, 2012.

[12] H. Cao et al., “Enabling Technologies for Wireless Body Area Networks: A Survey and Outlook,” *IEEE Commun. Mag.*, vol. 47, no. 12, Dec. 2009, pp. 84-93.

[13] M. Klemm and G. troester, “Textile UWB Antennas for Wireless Body Area Networks”, *IEEE Trans. Antennas Propag.*, vol. 54, no. 11, pp. 3192-3197, Nov. 2006.

[14] C. M. Zierhofer and E. S. Hochmair, “High-efficiency coupling-insensitive transcutaneous power and data transmission via an inductive link,” *IEEE Trans. Biomed. Eng.*, vol. 37, no. 7, pp. 716–722, Jul. 1990.

[15] P. R. Troyk and M. A. K. Schwan, “Closed-loop class E transcutaneous power and data link for microimplants,” *IEEE Trans. Biomed. Eng.*, vol. 39, no. 6, pp. 589–599, Jun. 1992.

[16] M. Ghovanloo and S. Atluri, “A wideband power-efficient inductive wireless link for implantable microelectronic devices using multiple carriers,” *IEEE Trans. Circuits Syst. I, Reg. Papers*, vol. 54, no. 10, pp. 2211–2221, Oct. 2007.

[17] U.M. Jow and M. Ghovanloo, “Design and Optimization of Printed Spiral Coils for Efficient Transcutaneous Inductive Power Transmission,” *IEEE Trans. Biomed. Circuits Syst.*, vol. 1, no. 3, pp. 193-202, Sep. 2007.

[18] U.M. Jow and M. Ghovanloo, “Modeling and optimization of printed spiral coils in air, saline, and muscle tissue environments,” *IEEE Trans. Biomed. Circuits Syst.*, vol. 3, no. 5, pp. 339-347, Oct. 2009.

[19] Z. Duan, and Y.X. Guo, “Rectangular Coils Modeling for Inductive Links in Implantable Biomedical Devices,” *IEEE Symposium on Antenna and Propagation*, Spokane, Washington, USA, July 3-8, 2011.

[20] Z. Duan, Y.X. Guo, and D.L. Kwong, “Rectangular coils optimization for wireless power transmission”, *Radio Sci.*, vol. 47, RS3012, Jun. 2012.

[21] M. W. Baker and R. Sarpeshkar, “Feedback analysis and design of RF power links for low-power bionic systems,” *IEEE Trans. Biomed. Circuits Syst.*, vol. 1, no. 1, pp. 26–38, Mar. 2007.

[22] G. Simard, M. Sawan, and D. Massicotte, “Novel coils topology intended for biomedical implants with multiple carrier inductive link,” in *Proc. IEEE Int. Symp. Circuits Syst.*, May. 24-27, 2009, pp. 537–540.

[23] W. Liu, M. Sivaprakasam, G. Wang, M. Zhou, J. Granacki, J. Lacoss, and J. Wills, “Implantable biomimetic microelectronic systems design,” *IEEE Eng. Med. Biol. Mag.*, vol. 24, no. 5, pp. 66–74, Sep. - Oct. 2005.

[24] K. Gosalia, G. Lazzi, and M. Humayun, “Investigation of a microwave data telemetry link for a retinal prosthesis,” *IEEE Trans. Microw. Theory Tech.*, vol. 52, no. 7, pp. 1925–1933, Aug. 2004.

[25] Z. Duan, Y.X. Guo, R.F. Xue, M. Je, and D.L. Kwong, “Differentially-fed dual-band implantable antenna for biomedical applications”, *IEEE Trans. Antennas Propag.*, vol. 60, no.12, pp. 5587-5595, Dec 2012.

[26] J. Kim, and Y. Rahmat-Samii, “Implanted antennas inside a human body: simulations, designs, and characterizations”, *IEEE Trans. Microw. Theory Tech.*, vol. 52, no. 8, pp. 1934-1943, Aug. 2004.

[27] P. Soontornpipit, C. M. Furse, and Y. C. Chung, “Design of Implantable Microstrip Antenna for Communication With Medical Implants”, *IEEE Trans. Microw. Theory Tech.*, vol. 52, no. 8, pp. 1944-1951, Aug. 2004.

[28] C.-M. Lee, T.-C. Yo, C.-H. Luo, C.-H. Tu and Y.-Z. Juang, “Compact broadband stacked implantable antenna for biotelemetry with medical devices”, *Electron. Lett.*, vol. 43, no. 12, pp. 660-662, Jun. 2007.

[29] C.-M. Lee, T.-C. Yo, F.-J. Huang, and C.-H. Luo, “Dual-resonant π-shape with double L-strips PIFA for implantable biotelemetry”, *Electron. Lett.*, vol. 44, no. 14, pp. 837 – 838, Jul. 2008.

[30] W. C. Liu, F. M. Yeh, and M. Ghavami, “Miniaturized Implantable Broadband Antenna for Biotelemetry Communication,” *Microwave Opt. Technol. Lett.*, vol.50, no. 9, pp. 2407-2409, Sep. 2008.

[31] W. C. Liu, S. H. Chen, and C. M. Wu, “Bandwidth Enhancement and Size Reduction of an Implantable PIFA Antenna for Biotelemetry Devices,” *Microwave Opt. Technol. Lett.*, vol. 51, no. 3, pp.755-757, Mar. 2009.

[32] Z. N. Chen, G. C. Liu, and T. S. P. See, “Transmission of RF signals between MICS loop antennas in free space and implanted in the human head,” *IEEE Trans. Antennas Propag.*, vol. 57, no. 6, pp. 1850–1854, Jun. 2009.

[33] J. Abadia, F. Merli, J.-F. Zürcher, J. R. Mosig, A. K. Skrivervik, "3D-Spiral Small Antennas Design and Realization for Biomedical Telemetry in the MICS band", *Radioengineering*, vol. 12, no. 4, pp. 359-367, Dec 2009.

[34] T.-F. Chien, C.-M. Cheng, H.-C. Yang, J.-W. Jiang and C.-H. Luo, "Development of Non-Superstrate Implantable Low Profile CPW-Fed

Ceramic Antennas", *IEEE Antennas and Wireless Propag. Lett.*, vol. 9, pp. 559-562, 2010.

[35] A. Kiourti, M. Christopoulou, and K. S. Nikita, "Performance of a novel miniature antenna implanted in the human head for wireless biotelemetry," in *Proc. IEEE Int. Symp. Antennas Propag.*, Spokane, WA, 2011, pp. 392–395.

[36] P. M. Izdebski, H. Rajagopalan and Y. Rahmat-Samii, "Conformal ingestible capsule antenna: A novel chandelier meandered design", *IEEE Trans. Antennas Propag.* vol. 57, no. 4, pp. 900-909, Apr. 2009.

[37] W. Xia, M. Takahashi, and K. Ito, "Performances of an implanted cavity slot antenna embedded in the human arm", *IEEE Trans. Antennas Propag.*, vol. 57, no. 4, pp. 894-899, Apr. 2009.

[38] N. Haga, K. Saito, M. Takahashi, and K. Ito, "Characteristics of cavity slot antenna for body-area networks", *IEEE Trans. Antennas Propag.*, vol. 57, no. 4, pp. 837-843, Apr. 2009.

[39] M. L. Scarpello, D. Kurup, H. Rogier, D. Vande Ginste, F. Axisa, J. Vanfleteren, W. Joseph, L. Martens, and G. Vermeeren, "Design of an implantable slot dipole conformal flexible antenna for biomedical applications," *IEEE Trans. Antennas Propag.*, vol. 59, no. 10, pp. 3556–3564, 2011.

[40] T. Dissanayake, K. P. Esselle and M. R. Yuce, "Dielectric loaded impedance matching for wideband implanted antennas", *IEEE Trans. Microw. Theory Tech.*, vol. 57, no. 10, pp. 2480-2487, Oct. 2009.

[41] "Rec. ITU-R RS.1346," Int. Telecommun. Union. Geneva, Switzerland, 1998.

[42] "Rep. ITU-R SM.2180," Int. Telecommun. Union. Geneva, Switzerland, 2010.

[43] J. Gemio, J. Parron, and et al., "Human Body Effects on Implantable Antennas for ISM Bands Applications: Models Comparison and Propagation Losses Study," *Progress In Electromagnetics Research* vol. 110, pp. 437-452, 2010.

[44] S. Gabriel, R. W. Lau, and C. Gabriel, "The dielectric properties of biological tissues," *Phys.Med. Biol.* pp. 2231–2293 [Online]. Available: http://niremf.ifac.cnr.it/tissprop/, Oct. 2004, (1996).

[45] CST Microwave Studio Suite, www.cst.com

[46] *IEEE Standard for Safety Levels with Respect to Human Exposure to Radio Frequency Electromagnetic Fields, 3 kHz to 300 GHz*, IEEE Standard C95.1-1999, 1999.

[47] *IEEE Standard for Safety Levels with Respect to Human Exposure to Radio Frequency Electromagnetic Fields, 3 kHz to 300 GHz*, IEEE Standard C95.1-2005, 2006.

[48] F. Viani, P. Rocca, G. Oliveri, D. Trinchero, and A. Massa, "Localization, tracking, and imaging of targets in wireless sensor networks: An invited review," *Radio Sci.*, 46, RS5002, 2011.

[49] H.-T. Chou, L.-R. Kuo, H.-H. Chou, K.-L. Hung, and P. Nepa, "Realistic implementation of ellipsoidal reflector antennas to produce near-field focused patterns," *Radio Sci.*, 46, RS5007, 2011.

[50] H.-T.Chou, P.-H. Hsueh, T.-M. Hung, L.-R. Kuo, and H.-H. Chou, A "dual-band near-field focused reflectarray antenna for RFID applications at 0.9 and 2.4 GHz," *Radio Sci.*, 46, RS6010, 2011.

[51] X. Qing, Z. N. Chen, and M. Y. W. Chia, "Characterization of ultra-wideband antennas using transfer functions," *Radio Sci.*, 41, RS1002, 2006.

[52] M. Klemm, I. J. Craddock, A. Preece, J. Leendertz, and R. Benjamin, "Evaluation of a hemi-spherical wideband antenna array for breast cancer imaging," *Radio Sci.*, 43, RS6S06, 2008.

[53] Y. Jang and M. M. Jovanovic, "A contactless electrical energy transmission system for portable-telephone battery chargers," *IEEE Trans. Ind. Electron.*, vol. 50, no. 3, pp. 520–527, Jun. 2003

[54] N. Najafi, C.A. Rich, and S. Massoud-Ansari, "system for monitoring conduit obstruction," *US Patent 7211048*, May 2007.

[55] X. K. Chen, X. Y. Zhang, and L. W. Zhang et al., "A Wireless Capsule Endoscope System With Low-Power Controlling and Processing ASIC," *IEEE Trans. Biomed. Circuits Syst.*, vol. 3, no. 1, pp. 11-22, Feb. 2009.

[56] S. Ahn and J. Kim, "Magnetic Field Design for High Efficient and Low EMF Wireless Power Transfer in On-Line Electric Vehicle," *EUCAP*, Rome, 2011, pp. 3979-3982.

[57] G. A. Kendir, W. Liu, R. Bashirullah, G. Wang, M. Sivaprakasam, R. Bashirullah, M. S. Humayun, and J. D. Weiland, "An optimal design methodology for inductive power link with Class-E amplifier," *IEEE Trans. Circuits Syst., Reg. Papers*, vol. 52, no.5, pp. 857–866, May 2005.

[58] Z. Yang, W. Liu, and E. Basham, "Inductor modeling in wireless links for implantable electronics," *IEEE Trans. Magn.*, vol. 43, no. 10, pp. 3851-3860, Oct. 2007.

[59] A. N. Laskovski, M. R. Yuce, and T. Dissanayake, "Stacked spirals for use in biomedical implants", *Asia Pacific Microwave Conference*, Singapore, Dec. 7-10, 2009, pp. 389-392.

[60] M. R. Shah, R. P. Phillips, and R. A. Normann, "A study of printed spiral coils for neuroprosthetic transcranial telemetry applications," *IEEE Trans. Biomed. Eng.*, vol. 45, no. 7, pp. 867-876, Jul. 1998.

[61] W. Li, D. C. Rodger, J. Weiland, M. Humayun, and Y. C. Tai. "Integrated flexible ocular coil for power and data tranfer in retinal prostheses," in *Proc. 27th Annu. Int. Conf. IEEE Eng. Medicine Biol. Soc.*, Shanghai, China, 2005, pp. 1028-1031.

[62] K. M. Silay, C. Dehollain, and M. Declercq, "Improvement of Power Efficiency of Inductive Links for Implantable Devices," *Proc. PRIME'08 Conf.*, 2008, pp. 229-232.

[63] Y. Hu and M. Sawan, "A Fully Integrated Low-Power BPSK Demodulator for Implantable Medical Devices," *IEEE Trans. Circuits Syst. I*, Vol. 52, No. 12, pp.2552-2562, Dec. 2005.

[64] W. H. Ko, S. P. Liang, and C. D. Fung, "Design of radio-frequency powered coils for implant instruments," *Med. Biol. Eng. Comp.*, vol. 15, pp. 634-640, 1977.

[65] C. M. Zierhofer and E. S. Hochmair, "Geometric Approach for Coupling Enhancement of Magnetically Coupled Coils," *IEEE Trans. Biomed. Eng.*, vol. 43, no. 7, pp. 708-714, Jul. 1996.

[66] T. H. Lee, *The Design of CMOS Radio-Frequency Integrated Circuits*, 2nd ed. Cambridge, U.K.: Cambridge University Press, 2004.

[67] K. M. Silay, D. Dondi, L. Larcher, M. Declercq, L. Benini, Y. Leblebici and C. Dehollain, "Load Optimization of an Inductive Power Link for Remote Powering of Biomedical Implants," *IEEE Int. Symposium. Circuits Syst.*, 2009, pp. 533-536.

[68] E. G. Kilinc, C. Dehollain, F. Maloberti, "Design and optimization of inductive power transmission for implantable sensor system," in *Proc. SM2ACD'10*, 2010, pp.1-5.

[69] H. M. Greenhouse, "Design of Planar Rectangular Microelectronic Inductors," *IEEE Trans. Parts, Hybrids Packag.*, vol. PHP-10, no. 2, pp. 101-109, Jun. 1974.

[70] K. Kang, J. Shi, W. Y. Yin, L. W. Li, S. Zouhdi, S. C. Rustagi and K. Mouthaan, "Analysis of Frequency- and Temperature-Dependent Substrate Eddy Currents in On-chip Spiral Inductors Using the Complex Image Method," *IEEE Trans. Magnetics*, vol. 43, no. 7, Jul 2007.

[71] F. W. Grove, *Inductance Calculations: Working Formulas and Tables*. New York: Van Nostrand, 1946.

[72] W. B. Kuhn and N. M. Ibrahim, "Analysis of current crowding effects in multiturn spiral inductors," *IEEE Trans. Microwave Theory Tech.*, vol. 49, pp. 31–38, Jan. 2001.

[73] Y. Eo and W. R. Eisenstadt, "High-speed VLSI interconnect modeling based on S-parameter measurements," *IEEE Trans. Comp., Hybrids, Manufact. Technol.*, vol. 16, pp. 555–562, Aug. 1993.

[74] C. J. Sánchez-Fernández, O. Quevedo-Teruel, J. Requena-Carrión, L. Inclán-Sánchez, and E. Rajo-Iglesias, "Dual-band microstrip patch antenna based on short-circuited ring and spiral resonators for implantable medical devices," *Microw., Antennas Propag. IET*, vol. 4, no. 4, pp. 1048–1055, Aug. 2010.

[75] F. J. Huang, C. M. Lee, C. L. Chang, L. K. Chen, T. C. Yo, and C. H. Luo, "Rectenna application ofminiaturized implantable antenna design for triple-band biotelemetry communication," *IEEE Trans. Antennas Propag.*, vol. 59, no. 7, pp. 2646–2653, Jul. 2011.

[76] Z. M. Chen, K. W. Cheng, Y. J. Zheng, and M. Je, "A 3.4 mW 54.24 Mbps burst-mode injection-locked CMOS FSK transmitter," in *Proc. IEEE Asian Solid State Circuits Conf.*, Nov. 14–16, 2011, pp. 289–292.

[77] D. E. Bockelman and W. R. Eisenstadt, "Combined differential and common-mode scattering parameters: Theory and simulation," *IEEE Trans. Microw. Theory Tech.*, vol. 43, no. 7, pp. 1530–1539, Jul. 1995.

[78] D. E. Bockelman and W. R. Eisenstadt, "Pure-mode network analyzer for on-wafer measurements of mixed-mode S-parameters of differential

circuits," *IEEE Trans. Microw. Theory Tech.*, vol. 45, no. 7, pp. 1071–1077, Jul. 1997.

[79] R. Meys and F. Janssens, "Measuring the impedance of balanced antennas by an S-parameter method," *IEEE Antennas Propag. Mag.*, vol. 40, no. 6, pp. 62–65, Dec. 1998.

[80] W. Fan, A. Lu, L. L. Wai, and B. K. Lok, "Mixed-mode S-parameter characterization of differential structures," in *Proc. 5th Conf. Electron. Packag. Technol.*, Dec. 10–12, 2003, pp. 533–537.

[81] K. D. Palmer and M.W. V. Rooyen, "Simple broadband measurements of balanced loads using a network analyzer," *IEEE Trans. Instrum. Meas.*, vol. 55, no. 2, pp. 266–272, Feb. 2006.

[82] Y. P. Zhang and J. J. Wang, "Theory and analysis of differentially-driven microstrip antennas," *IEEE Trans. Antennas Propag.*, vol. 54, no. 4, pp. 1092–1099, Apr. 2006.

[83] R. Bourtoutian, C. Delaveaud, and S. Toutain, "Differential, shorted dipole antenna for European UWB applications," in *Proc. 2nd Eur. Conf. Antennas Propag.* (EuCAP'07), Nov. 2007, pp. 1–5.

[84] X. Qing, C. K. Goh, and Z. N. Chen, "Impedance characterization of RFID tag antennas and application in tag co-design," *IEEE Trans. Microw. Theory Tech.*, vol. 57, no. 5, pp. 1268–1274, May 2009.

[85] H. L. Zhu, Y. C. A. Ko, and T. T. Ye, "Impedance measurement for balanced UHF RFID tag antennas," in *Proc. IEEE Radio Wireless Symp.*, Jan. 2010, pp. 128–131.

[86] L. Han, W. Zhang, X. Chen, G. Han, and R. Ma, "Design of compact differential dual-frequency antenna with stacked patches," *IEEE Trans. Antennas Propag.*, vol. 58, no. 4, pp. 1387–1392, Apr. 2010.

[87] C.-M. Su, H.-T. Chen, and K. L. Wong, "Printed compact dual band antenna for 2.4 and 5 GHz ISM band applications," *Electron. Lett.*, vol. 38, no. 22, pp. 1568–1569, Oct. 2002.

[88] W. Greatbatch and C. F. Homes, "History of implantable devices," *IEEE Engineering in Medicine and Biology Magazine*, vol. 10, no. 3, pp. 38-41, Sep 1991.

[89] C. R. Liu, Y. X. Guo, and S. Q. Xiao, "Compact Dual-Band Antenna for Implantable Devices", *IEEE Antennas Wireless Propag. Lett*., vol. 11, pp. 1508-1511, Dec, 2012.

[90] S. Yun, K. Kim, and S. Nam, "Outer wall loop antenna for ultra wideband capsule endoscope system," *IEEE Antennas Wireless Propag. Lett.*, vol. 9, pp. 1135–1138, Dec. 2010.

[91] F. Merli, L. Bolomey, J.-F. Zürcher, G. Corradini, E. Meurville, and A. K. Skrivervik, "Design, realization and measurements of a miniature antenna for implantable wireless communication systems", *IEEE Trans. Antennas Propag.*, vol. 59, no. 10, pp. 3544-3555, Oct. 2011.

[92] P. D. Bradley, "An ultra low power, high performance medical implant communication system (MICS) transceiver for implantable devices," in *Proc. IEEE Biomedical Circuits and Systems Conf. BioCAS 2006*, Nov. 2006, pp. 158–161.

[93] L. J. Xu, Y. X. Guo, and W. Wu, "Dual-Band Implantable Antenna with Open-End Slots on Ground", *IEEE Antennas Wireless Propag. Lett*., vol. 11, pp. 1564-1567, Dec. 2012.

[94] F. Merli, B. Fuchs, J. R. Rosig and A. K. Skrivervik, "The effect of insulating layers on the performance of implanted antennas", *IEEE Trans. Antennas Propag.*, vol. 59, no. 1, pp. 21-31, Jan. 2011.

[95] A. Kiourti and K. Nikita, "A review of implantable patch antennas for biomedical telemetry: Challenges and solutions," *IEEE Antennas and Propag. Mag.*, vol. 54, no. 3, pp. 210 –228, Jun. 2012.

[96] K. Cheng, et. al., “100-channel wireless neural recording system with 54-Mb/s data link and 40%-efficiency power link,” in *Proc. IEEE Asian Solid State Circuits Conference (A-SSCC) Dig. Tech. Papers*, Dec. 2012, pp. 185–188.

[97] R. Jegadeesan, Y.X. Guo, “Topology selection and efficiency improvement of inductive power links,” *IEEE Trans. Antennas Propag.*, vol. 60, no. 10, pp. 4846-4854, Oct 2012.